Fun iMat

RTMM

ICMOL
Institut de Ciència Molecular

Garin Escorcia-Ariza 2019 Ph.D. Thesis

Engineering new tools for automated fabrication of molecular thin films and study of their electrical properties

Supervisors:
Sergio Tatay Aguilar
Carlos Martí Gastaldo

Garin Escorcia-Ariza
University of Valencia
Paterna, May 2019

Ph.D. thesis in Nanoscience and Nanotechnology

GENERALITAT VALENCIANA
Conselleria d'Educació, Investigació, Cultura i Esport
Grisolia/2015/007

erc

Engineering new tools for automated fabrication of molecular thin films and study of their electrical properties

Universidad de Valencia

Instituto de Ciencia Molecular (ICMol)

***

Memoria presentada por Garin Escorcia Ariza para aspirar al grado de Doctor en Nanociencia y Nanotecnología

***

Dirigida por el Dr. Sergio Tatay Aguilar y el Dr. Carlos Martí Gastaldo

***

May 2019

“La única manera de hacer un gran trabajo es amar lo que hace. Si no ha encontrado todavía algo que ame, siga buscando. No se conforme. Al igual que los asuntos del corazón, sabrá cuando lo encuentre”

(Steve Jobs. 1955-2011. Fundador de Apple)

Acknowledgments

Esta tesis fue todo un reto para mí, principalmente porque me obligó a cambiar de ciudad, país y cultura, incluso hasta de área de formación disciplinar, de ingeniería a ciencias básicas.

En primer lugar, me gustaría agradecer a mis tutores Sergio Tatay y Carlos Martí por su supervisión y dirección durante la realización de esta tesis. Y, especialmente a Sergio Tatay por ser mi guía durante todo el doctorado, además de retarme siempre a desarrollar nuevos equipos y a adquirir nuevos conocimientos. Y particularmente a Carlos Martí por creer en mi para usar mis talentos en el desarrollo de nuevos equipos experimentales. También quisiera agradecer al Prof. Eugenio Coronado, director del ICMol y líder del RTMM, por crear el Master en Nanociencia y Nanotecnología Molecular qué me dio la oportunidad de conocer a las excelentes personas con las que he convivido durante mi estancia el ICMol, empezar mi carrera investigadora y conocer un poco más la investigación fundamental, además por ofrecerme la beca Santiago Grisolía que me permitió alargar mi estancia hasta este momento. También a Alicia Forment y Elena Pinilla por introducirme en la química y microscopia de superficies. A Marta Galbiati por iniciarme en las medidas de transporte. A Ramon Torres por siempre estar dispuesto a explicarme aspectos y conceptos varios sobre la química que no comprendía, también a Victor Rubio por enseñarme las técnicas de Langmuir Blodgett y Layer-by-Layer. De igual forma, a Marc Morant y a Safaa Moubtassim, mis compañeros de despacho y consejeros a la hora de escribir este documento.

En segundo lugar, me gustaría agradecer a todos aquellos que participaron en las publicaciones en las que colaboré entre ellos, Victor Rubio-Giménez, Marta Galbiati, Javier Castells-Gil, Neyvis Almora-Barrios, José Navarro-Sánchez, Michele Mattera, Thomas Arnold, Jonathan Rawle, Sergio Tatay, Eugenio Coronado, y Carlos Martí-Gastaldo, Michele Sessolo. También a todos los técnicos que hacían más fácil la estancia en el laboratorio, Ángel López, Cristian Zoia, Alejandra Soriano, Paco Gonzales, Marian Hernández, que ya no pertenece al grupo, a Paco Escrig, Manuel Pérez y Julián Herrero.

En cuanto a mi estancia en el instituto, nada sería igual sin mis inigualables compañeros o excompañeros de despacho Marc, Safaa, Helena, Marta, Josef, Alejandra, Marian y Javi C. También agradezco a Vero, Marc, Ramon y Yan por inspirarme con su incansable trabajo en el laboratorio. De la misma manera, también agradezco a todos mis compañeros de máster que me dieron la bienvenida a España, y en especial al instituto, que me acogió como uno más de este gran grupo académico.

En cuanto a mi vida estancia en Valencia, agradezco a Alejandra, Marc, Jose Miguel, Vero y Yan por hacerme parte de sus familias, sin ellos no habría podido soportar tantos cambios en mi vida. A Paco, Jose Jaime, Vicente, Marc y Jose Miguel por ser los mejores compañeros de viaje.

Finalmente me gustaría agradecer a mi familia y en especial a mis abuelos paternos (Rosita y Walter) por su apoyo, motivación y consejos, que solo la sabiduría de los años puede ofrecer, a mis hermanos y a mis padres por su acompañamiento constante, de principio a fin, en esta odisea del conocimiento.

Abbreviations

-	Output
A_g	Geometrical Contact Area
E_{CBM}	Minimum energy of Conduction Band
E_F	Fermi Level
E_{VBM}	Maximum energy of Valence Band
E_a	Activation Energy
E_g	Energy Gap
I_{DS}	Drain-source current
R_c	Contact Resistance
R_s	Sample Resistance
R_w	Wire Resistance
T_a	Absolute Temperature
V_{AC}	Alternating Current Voltage
V_{DC}	Voltage Direct Current
V_{DS}	Drain-source voltage
V_G	Gate Voltage
V_t	Transition Voltage
m^*	Effective mass
σ_{N_2}	Electrical Conductivity in Nitrogen
[EMI] [TFSA]	1-ethyl-3-methylimidazolium bis(trifluoromethylsulfonyl)amide
+	Input
Δf	Frequency Shift
µm	micrometer
2D	Two-dimensional
3D	Three dimensional

ABLM	5-azabenzimidazole
ABS	Acrylonitrile butadiene styrene
APTES	3-aminopropyltriethoxysilane
BC	Bottom Contacts
BDC	1,4-benzenedicarboxylate
BG	Bottom Gate
bpy	2,2'-bipyridine
BTC	1,3,5-benzenetricarboxylate
C-AFM	Conductive Atomic Force Microscopy
CAT	Catecholate / HHTP = 2,3,6,7,10,11-hexahydroxytriphenylene
CB	Conduction Band
CISS	Chiral Induced Spin Selectivity
CMOS	Complementary metal-oxide-semiconductor
CoTCPP	5,10,15,20-tetrakis (4-carboxyphenyl)-porphyrinatocabalt (II)
CP	Coordinated Polymer
CPD	Contact potential difference
CV	Cyclo-voltammetry
DABCO	1,4-diazabicyclo[2.2.2]octane
DFT-D3	dispersion corrected density functional theory
DNA	deoxyribonucleic acid
EGaIn	Gallium Indium Eutectic
eV	Electron volts
exp	Exponent
FET	Field Effect Transistor
FN	Fowler-Nordheim

GPIB	General Purpose Interface Bus
GΩ	Giga ohm
HBTC	5-carboxy-benzene-1,3-dicarboxylate dianion
HC	Hoffman Clathrate
HEPES	4-(2-hydroxyethyl)-1-piperazineethanesulfonic acid
HITP	2,3,6,7,10,11-hexaiminotriphenylene
HITP	2,3,6,7,10,11-hexaimino-triphenylene
HKUST-1	Hong Kong University of Science and Technology n°1
HS	High-Spin
ICMol	Institute of Molecular Science
IRRAS	infrared reflection absorption spectroscopy
ISO	International Organization for Standardization
KΩ	Kilo ohm
L	Ligand
LB	Langmuir Blodgett
LbL	Layer-by-Layer
LBT	Lanthanide Binding Tag
LBTC	Lanthanide Binding Tag
LCD	Liquid Crystal Display
LS	Low- Spin
M	Metal
MIL-101	Materials of Institute Lavoisier n°101
MIL-89	Materials of Institute Lavoisier n°89
MOF	Metal Organic Framework
MOF-2	Metal Organic Framework n°2

MOF-5	Metal Organic Framework n˚5
MTBS	Methyltributylammnium methyl sulfate
MΩ	Mega ohm
NP	Nanoparticles
OAc	Acetoxy Group
OLEDs	organic light-emitting diodes
P(VDFHFP)	Poly(vinylidene fluoride co-hexafluoropropylene)
PC	Personal Computer
PCB	Printed Circuit Board
PDB	Protein Data Bank
QCM	Quartz Crystal Microbalance
r	Spatial Distance
RTMM	Research Team on Molecular Materials
S	Gap between electrodes
$S*cm^{-1}$	Siemens/centimeter
SAM	Self-assembled Monolayers
sccm	Standard Cubic Centimeter per Minute
SCO	Spin-Crossover
SP	Spin Polarization
SPR	Surface Plasmon Resonance
SURMOF-2	Surface-bound metal-organic framework n˚2
TC	Top Contacts
TCNQ	7,7,8,8-tetracyanoquinododimethane
TG	Top Gate
TVS	Transition Voltage Spectroscopy
USB	Universal Serial Bus

VB	Valence Band
VOCs	Volatile organic compounds
ZIF-22	Zeolite Imidazole Frameworks n˚22
ZIF-8	Zeolite Imidazole Frameworks n˚8
ZIF-90	Zeolite Imidazole Frameworks n˚90
ϵ_o	Molecular orbital energy offset
Ω	Ohm
$\boldsymbol{A}$	Area, ammeter or amperes
$\boldsymbol{D}$	Sample diameter, sample width or drain
$\boldsymbol{E}$	Energy difference
$\boldsymbol{F}$	correction factor of Four-point probe
$\boldsymbol{G}$	Electrical conductance or Gate
$\boldsymbol{H}$	Thickness of the film
$\boldsymbol{I}$	Electrical current
$\boldsymbol{J}$	Current Density
$\boldsymbol{L}$	Length of the electrodes
$\boldsymbol{N}$	Number of gaps
$\boldsymbol{P}$	Hopping Probability
$\boldsymbol{R}$	resistance
$\boldsymbol{V}$	Voltage
$\boldsymbol{d}$	Distance
$\boldsymbol{d}$	Thickness
$\boldsymbol{e}$	Electrons or elemental charge
$\boldsymbol{h}$	Holes
$\boldsymbol{k}$	Boltzmann Constant
$\boldsymbol{l}$	Length
$\boldsymbol{n}$	Density

s	Distance between adjacent probes
w	Sample width
α	Constant that depends on the nature of hopping sites
β	Current Attenuation Factor
μ	Mobility
σ	Electrical Conductivity
τ	The mean time between two charge-scattering events

Motivation and organization of this thesis

I discovered Nanotechnology while I was studying Mechatronic Engineering. I immediately got fascinated! Then, I started thinking about how some of the mechatronic concepts I learnt could be applied to this field and at the end of my degree, I decided to join the Master of Molecular Nanoscience and Nanotechnology at the Institute of Molecular Nanoscience (ICMol). This institute was founded in 2000 and is located in the Scientific Park of the University of Valencia. Its main focus is to develop high-quality research in Materials Science and Nanoscience using a molecular approach by: i) designing and synthesizing molecules and molecular assemblies exhibiting useful physical or chemical properties, ii) investigating these properties through both experimental and theoretical approaches, and iii) exploring the potential applications of these molecules and materials in different areas of current interest (Metal-organic Frameworks (MOFs), Molecular Magnetism, Molecular Electronics, Molecular Spintronics, Nanotechnology, Biotechnology, Catalysis, etc.).

During my Master I worked among the Research Team on Molecular Materials (RTMM) led by Prof. Eugenio Coronado and Functional Inorganic Materials (Funimat) group led by Dr. Carlos Martí Gastaldo. There, I discovered the great potential of the Institute in developing new molecular materials and characterizing their properties (structural, optical, magnetic). But I thought that there was still place for improvement in the way that materials were integrated into functional devices. In fact, making new materials that are compatibles with current CMOS based technology (CMOS,

Complementary metal-oxide-semiconductor) will require its integration into surfaces and the use of electrical signals to address its properties.

Mechatronics is used to design new systems on different areas based on the automatization of buildings, homes, industries, vehicles, and to design robots or new machines that combine Mechanics, Electrics, Electronics, and Computational Control. And thus, it is perfectly suited to address some of the challenges of materials research.

Following those ideas, a Santiago Grisolía PhD Scholarship (GRISOLIA/2015/007) was granted to me with the group of Prof. Coronado. **Its aim was** to develop some of the platforms missing in the Institute to carry on with the study of the electrical properties of molecular materials and integration into electrical devices. The main purposes were: i) Nanostructuration of novel molecular materials like polypeptide, two-dimensional metal-organic frameworks (2D MOFs), spin-crossover coordination polymers (SCO-CPs) into thin films and ii) to reliably measure their electrical properties and to integrate them into functional devices (as for example gas sensors or field effect transistors) compatible with currents technologies.

Although I learnt a lot about the chemistry of these materials. It is important that the reader keeps in mind, that my main work has not been focused on the synthesis of materials but on the development of new tools that make its electrical characterization and their integration into devices possible. As a result, **this thesis will be focused specifically** on the description of the tools that I have developed and how to use them. I will put special care on signaling out what are their limitations and how can they be upgraded in the near future.

This document will be divided into **three chapters**:

The first chapter will start introducing what metal-organic frameworks (MOFs) are and why they are promising candidates for its integration into electronic devices. Then, I will present the general principles to understand the electronic properties followed by the techniques used to measure electrical properties of bulk samples and thin films. And finally, I will review the techniques used to deposit MOFs as thin films.

In the second chapter, these concepts will be focused on the development of necessary tools to the study electrical conductivity of a family of isostructural two-dimension metal-organic frameworks (2D-MOFs). More precisely M-CAT-1 formed through combination of the CAT ligand [CAT = catecholate = HHTP = 2,3,6,7,10,11-hexahydroxytriphenylene] with different metals (M) such as Cu, Co, Ni, Zn and Cd. We will focus on Cu-CAT-1 which turned to be the most conductive of its family. Then, I will review how Cu-CAT-1 thin films were deposited and how its electrical properties were studied. Additionally, we will show the tools and experiments carried out to find out the origin of the chemiresistive response of these 2D MOF films.

The third chapter will focus on the use of Quartz Crystal Microbalance (QCM) working in continuous flow regime to study the deposition of Lanthanide Binding Tag (LBT) coordinated to Tb^{3+} and Hoffman Clathrate (HC) Coordinated Polymers (CPs) onto a conductive film. Then, we will study the electrical properties of both materials on a vertical setup using liquid metals as top contact. On the case of HCs, we will show how electrical transport depends on the

thickness of the films and the pillars nature. Finally, I will present how this measuring method can be adapted to measure Chiral-induced spin selectivity (CISS) effect by modifying the initial setup to be able apply magnetic fields while the electrical flow is measured.

Publications

The following works were published during the course of this PhD:

[1] Rubio-Giménez, V., Galbiati, M., Castells-Gil, J., Almora-Barrios, N., Navarro-Sánchez, J., Escorcia-Ariza, G., Mattera, M., Arnold, T., Rawle, J., Tatay, S., Coronado, E., & Martí-Gastaldo, C. Bottom-Up Fabrication of Semiconductive Metal-Organic Framework Ultrathin Films. *Advanced Materials* 30, 1704291 (2018).

[2] Rubio-Giménez, V., Almora-Barrios, N., Escorcia-Ariza, G., Galbiati, M., Sessolo, M., Tatay, S., & Martí-Gastaldo, C. Origin of the Chemiresistive Response of Ultrathin Films of Conductive Metal- Organic Frameworks. *Angewandte Chemie International Edition* 57, 15086-15090 (2018). ***First Autor***

[3] Rubio-Giménez, V., Escorcia-Ariza, G., Bartual-Murgui, C., Sternemann, C., Galbiati, M., Castells-Gil, J., Antonio Real, J., Tatay, S., & Martí-Gastaldo, C. Effect of nitrogenated linker in Hoffman Clathrates (HCs) over structure pillaring and vertical transport. ***submited***

[4] Cardona-Serra, S., Torres-Cavanillas, R., Escorcia-Ariza, G., Chandra Mondal, P., Giménez-Santamarina, S., Sessolo, M., Galbiati, M., Tatay, S., Rosaleny, L. E., Forment-Aliaga, A., Gaita-Ariño, A. Room temperature spin filtering in a metallopeptide. ***work in progress***

Contents

Chapter One - Introduction

1. Introduction

Miniaturization of integrated digital circuits is one of the key pillars of the current information technology. However, downsizing of current Complementary Metal-Oxide-Semiconductor (CMOS) technology will come to an end in the foreseeable future.

This is reflected in Moore's law,[1] which predicts that every two years the number of transistor per cm square in a microprocessor would be doubling. However, the circuit miniaturization is approaching sizes where quantum uncertainties will make transistors unreliable. Current state-of-the-art silicon technology enables up to 100 million transistors per mm square being the typical size of few nanometers like the generation of 14 nm.[2] At this point, CMOS technology is becoming increasingly expensive.

As a result, new approaches and novel materials are explored with increased interest. New trends such as low-power/low-cost standalone devices (e.g. ‘‘internet-of-things’’ applications) and flexible electronics are further inciting this interest.

The discovery of intrinsically conducting polymers and organic conductors on 1970s[3,4] opened the possibility to use organic materials, and more generally organic-inorganic hybrids, as replacement of traditional pure inorganic semiconductors, like silicon. Since then, the so-called molecular materials have increased their presence on electronic devices thanks to that they are cheaper to produce, and they also present great variability and chemical diversity.

Molecular materials represent a class of substances where seemingly small changes in molecular structure can change totally the properties

of the material.[5,6] Many molecular materials have demonstrated a wide range of physical phenomena since the 1980s. The scope of those materials is vast and diverse, and their magnetic, optical and electrical properties have been studied.[6] One of these molecular materials that have demonstrated potential for applications are Metal-organic frameworks (MOFs).

Metal-Organic Frameworks (MOFs) are crystalline solids built from the linking of organic and inorganic components with coordinative bonds. The controllable positioning of inorganic clusters or metal nodes and organic linkers into the three-dimensional space enables the assembly of topologically regular structures with very high surface areas ranging up to 8000 m^2 g^{-1}.[7] These empty pockets can be also molecularly engineered in size, shape and chemical function to render a rich family of crystalline solids with structural and functional diversities beyond compare.[8]

Those have already found applications as gas storage[9,10] and separation[11] as well as heterogeneous catalysis.[12] Moreover, its use in sensing, magnetism, ferroelectricity, nonlinear optics or drug delivery applications are gaining importance.[13] Traditionally MOFs exhibit very low electrical conductivity, a direct consequence of how these materials are constructed: metal ions are connected by redox inactive organic ligands that bind via oxygen atoms.[14] Therefore, the vast majority of MOFs do not provide any low-energy pathway for charge transport, nor any free charge carries, and behave as electrical insulators with conductivity lower than 10^{-10} S cm^{-1}. Nevertheless, in the last ten years, some remarkable examples of conductive MOFs have been reported. With electrical conductivity adding a new dimension to

their tunable nature, MOFs have recently found new applications in electronic devices.[15,16] For example, $Cu_3(HITP)_2$ (HITP = 2,3,6,7,10,11-hexaiminotriphenylene) (Figure 1-1A) was used in chemiresistive sensors as reported by Campbell et. al.[17,18] In addition, $Ni_3(HITP)_2$ (Figure 1-1A) reported by Dincă et. al. together to a collection of nanocrystalline MOFs reported by Yaghi et. al. were integrated on a device to work as supercapacitors.[19,20] Additionally, MIL-53(Fe) [$M^{III}OH(BDC)$; BDC = 1,4-benzenedicarboxylate; M^{III} = V^{III}, Cr^{III} or Fe^{III})] (Figure 1-1B) reported by Tarascon et. al and other similar structures where studied as possible candidates for battery components.[21–25] Similarly, Zn-SURMOF-2 [$Zn_2(BDC)$] (Figure 1-1C) was integrated into a solar cell device showing large charge-carrier mobility and large charge-carrier generation efficiency as reported by Wöll et. al.[26] Furthermore, HKUST-1 [$Cu_3(BTC)_2$; BTC = 1,3,5-benzenetricarboxylate] (Figure 1-1D) infiltrated with tetracyanoquinodimethane (TCNQ) as guest reported by Talin showed low thermal conductivity and High Seebeck Coefficient, properties highly desirable in the development of thermoelectric applications.[27] Furthermore, field-effect transistors (FETs) where 2D MOFs offer High electron and hole mobility have been reported by Pandas et. al. and Zhu et al.[28, 29]

Advances in these new areas depend critically on benchmarking the electrical properties of MOFs, including electrical conductivity, charge mobility, charge density, electronic band gap, and charge activation energy, for instance. In the following section, I will focus on the description and understanding of the parameters governing charge transport in this family of materials.

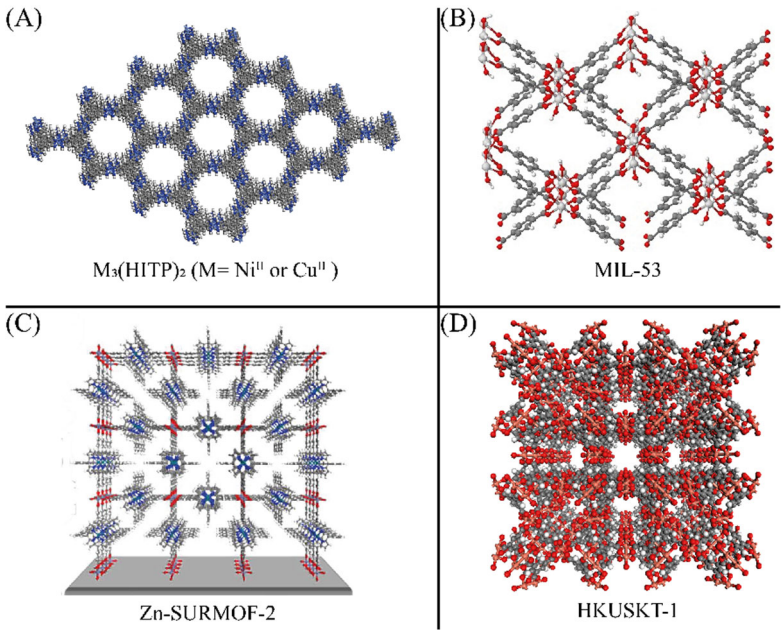

Figure 1-1 Crystal structures of (A)$M_3(HITP)_2$ (M= Ni^{II} or Cu^{II}) extracted from ref. 30, (B) MIL-53 extracted from ref. 31, (C) Zn-SURMOF-2 on a substrate extracted and modified from ref. 26, and (D) HKUST-1 extracted from Cambridge Crystallographic Data Center (CCDC) Deposition number (DN): 977873.

2. General principles of electronic properties

Electrical conductivity (σ) is the key factor by which the possibility to transport change on MOFs is judged. Conductivity is dictated by the density (n) and mobility (μ) of electrons (e) and holes (h). Both high charge density and high charge mobility are thus needed to achieve high conductivity [Eq. 1-1]:

$$\sigma = e(\mu_e * n_e + \mu_h * n_h) \qquad 1\text{-}1$$

High charge density requires that the material contains a high concentration of loosely bound charge carries (>10^{15} cm^{-3}). These can be either free carries, as in metallic conductors, or they can be thermally activated, as in semiconductors. Both metal ions and organic ligands of

MOFs could be sources of charge carries. Metal ions should have high-energy electrons or holes, for example, the unpaired electron of square-planar d^9 Cu^{II} centers or the minority-spin electron of high-spin octahedral d^6 Fe^{II} centers. Organic ligands should be either stable radicals, to provide unpaired electrons and their orbitals should overlap with the metal centers, or other redox-active centers to enable facile charge transfer between metal ions or nodes.

In principle, the highly ordered crystal structure of MOFs warrants the application of band theory to understand their electronic structures. According to band theory, solids can be classified as insulators, semiconductors, or metals based on the magnitude of the energy gap (E_g), separating the valence band (VB) from the conduction band (CB). Bands below the Fermi level are called valence bands and bands above the Fermi level are called conduction bands. Materials with $E_g > 4eV$ are considered insulators, while those with $0 < E_g < 3\,eV$ are semiconductors, and those with $E_g = 0$ are metals.[32] In metallic conductors, the CB and VB overlap and all electrons are free charge carries and, owing to the charge density in a metallic conductor is typically higher than 10^{20} cm^{-3}, this gives rise to high electrical conductivity (>100 Scm^{-1}).[33]

In semiconductors and insulators, the Fermi level lies in a gap between the VB and the CB. At absolute zero, the VB is completely filled, while the CB is completely empty. The energy difference between Fermi level and the valence band maximum (E_{VBM}) or the conduction band minimum (E_{CBM}) is called activation energy (E_a) [Eq.1-2]:

$$E_a = E_F - E_{VBM}$$
$$or \qquad 1\text{-}2$$
$$E_a = E_F - E_{CBM}$$

At finite temperature, VB electrons are thermally promoted into the CB, leaving holes in the VB. Both electrons and holes become free charges. Charge density is therefore determined by the activation energy [Eq.1-3]:

$$n = n_0 \exp\left(-\frac{E_a}{kT}\right) \qquad 1\text{-}3$$

where n_0 is a prefactor, k is the Boltzmann constant, and T is abstolute temperature. Clearly, the smaller the activation energy is, the larger the charge density and electrical conductivity are at a given temperature. In undoped (intrinsic) semiconductors, the Fermi level is generally considered to lay at the middle of the band gap. In doped (extrinsic) semiconductors, the dopant energy levels shift the Fermi level closer to the band edge of either the valence band or the conduction band reducing the E_a, and giving rise to p-type or n-type semiconductors with increased charge densities.[34] Charge mobility reflects the efficiency of the charge transport.

In the band transport regime (Figure 1-2A), [35] charge carriers (i.e. electrons and/or holes) are delocalized, with effective masses (m^*) determined by the band curvature. Charge mobility is dictated by the effective mass of the charge carries and the frequency of charge scattering events [Eq. 1-4]:[33]

$$\mu = \frac{e\tau}{m^*} \qquad 1\text{-}4$$

where e is the elemental charge, and τ is the mean time between two charge-scattering events. A high density of charge-scattering sites,

such as disorder, defects, impurities, or grain boundaries will lead to a small τ and thus low mobility. Achieving high mobility also requires that charge carriers have small effective mass. Although the effective mass is affected by a complex set of factors including band dispersion, crystal lattice symmetry, and unit-cell parameters, an essential requirement that leads to a small m^* is a well-dispersed band, which is fundamentally a result of good orbital overlap. On the other hand, the poor orbital overlap will result in poor dispersed bands and high m^* to the point that charge carriers will become localized at specific sites with discrete energy levels, and charge transport will be possible only when charge carries hop between neighboring sites.

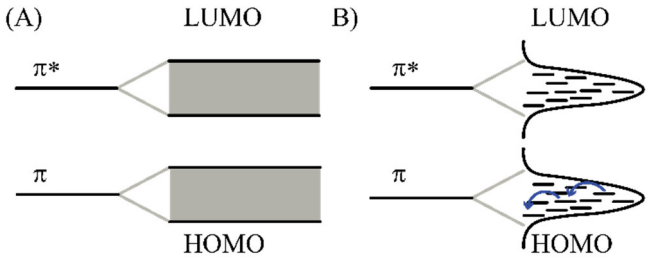

Figure 1-2 (A) representation of the structure for band transport. If the overlap between molecules is strong enough, the overlap of bonding and anti-bonding π orbitals leads to the formation of energy bands formed by a quasi-continuum of states. (B) Representation of the structure for hopping transport. In a MOF with poor orbital overlap. Extracted and adapted from ref. 37.

This will give rise to ***hopping transport regime*** (Figure 1-2B) where the charge mobility scales with the hopping probability (P), which is in turn governed by the spatial distance (R) and the energy difference (E) between neighboring hopping sites [Eq. 1-5]:[36]

$$P = exp\left(-\alpha R - \frac{E}{kT}\right) \qquad 1\text{-}5$$

where α is a constant that depends on the nature of hopping sites, and the other terms were defined above.

Both hopping transport and band transport require low-energy charge-transport pathways; however, as mentioned above, such pathways are absent in the vast majority of MOFs. From a design perspective, both modes of transport require good spatial and energetic overlap between orbitals of appropriate symmetry; improving the charge transport pathway by increasing orbital overlap will increase charge mobility. To obtain this aim, there have been two general synthetic approaches towards providing a charge-transport pathway in these materials: a "through-bond (via linker or guest)" approach, and a "through space" approach (Figure 1-3).[38] In principle, both approaches can give rise to either hopping or band transport. The through-bond approach aims to promote charge transport via favorable spatial and energetic overlap of the metal and ligand orbitals involved in covalent bonding. The through-space approach enables charge transport via non-covalent interactions (such as $\pi - \pi$ stacking) between electroactive fragments (i.e. molecular components with readily accessible redox couples, be it organic or inorganic) that are held in place by the metal-ligand bonds of the MOF. The permanent porosity of MOFs offers another variable for improving conductivity: the incorporation of guest molecules. The guest molecules can act as charge carries themselves, as in the case of ionically conductive MOFs. Alternatively, redox-active guest molecules may act as charge dopants, thereby inducing free charge carries within the MOF skeleton or walls through guest-framework charge-transfer interactions. Although

effective, the use of guest molecules to improve conductivity in a given material inevitable reduces the porosity, limiting materials applicability in scenarios where high surface areas are desirable.

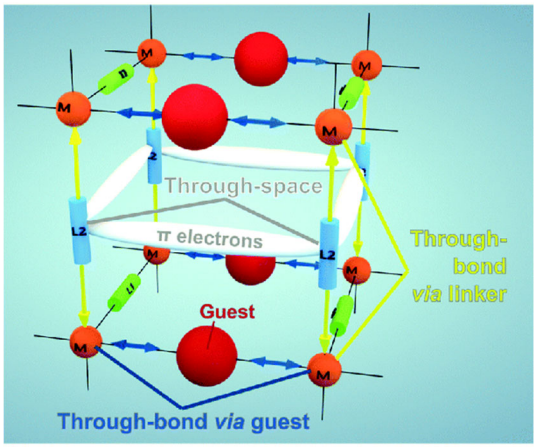

Figure 1-3 Schematic illustrations of analogous routes for charge and energy transport in MOFs. (a) Three possible mechanisms have been observed in MOFs for charge transport: through-bond conduction via metal nodes and linkers; through-bond conduction via guests that function as bridging units; and through-space conduction via charge delocalization through adjacent aromatic linkers. Extracted from ref. 39.

Up to this point, I have introduced different concepts that could help to understand the electrical properties of MOFs and in the last term their electrical conductivity. In the next section, I will introduce some of the techniques that can be used to measure them.

3. Conductivity measurement techniques

Electrical measurements are notoriously challenging because they depend not just on the intrinsic properties of the material being measured, but also on the materials used for the characterization (e.g. electrical leads, contact pastes, substrates, etc.) and the quality of the material itself. For this reason, it is necessary to study the different

techniques that have been used to measure the electrical conductivity and the mobility of MOFs.

Electrical conductivity (σ), measures the ability of a material to conduct electrical current. Measuring σ typically requires incorporating the material of interest into an electronic device, typically a resistor, and measuring electrical conductance (G), length (l) and area (A) of the conduction channel [Eq. 1-6]:

$$\sigma = G * \frac{l}{A} = \frac{I}{V} * \frac{l}{A} \qquad 1\text{-}6$$

Electrical conductance follows Ohm's law and is measured by taking the ratio between electrical current (I) and voltage (V), or by fitting the linear part of a $I - V$ curve. Depending on the nature of the material, charge transport may be limited and lead to a nonlinear I-V curve. Therefore, the appropriate voltage or current range is typically determined by experiment. The measured electrical conductance is determined by the intrinsic electrical conductivity of the material, but it also depends on the crystallinity and physical form of the measured sample, direction of electrical conduction, device quality, environment, and the sensibility of the ammeter and voltmeter. Equally important are the length and cross-sectional area of the conduction channel, which can be difficult to measure accurately and often introduce systematic errors, especially if the shape of the conduction channel is irregular.

Clearly, accurate measurements of intrinsic electrical conductivity are challenging and fraught with potential sources of errors. For this reason, many methods have been developed to measure electrical conductivity[30,40–46]. In this section, I will introduce two different situations: The first one, will cover conductivity measurements on all

samples that are not deposited on the surface, that is, bulk samples like polycrystalline powders and single crystal samples. In the other, I will cover cases where the samples that have already been deposited on surfaces as films.

3.1. Bulk samples

Single crystals are usually obtained by slow diffusion synthetic techniques that allow components of the system to organize themselves into crystals that maintain spatial periodicity in ranges above those found in microcrystalline powders. Other than crystallographic consideration, from a practical point of view, in our case, we set the limit to ~35 μm^3, because, at this is the smallest crystal that we can confidently contact.

Due to the fact that a single crystal is periodically ordered, the number of defects is very small, and it can be oriented to measure the electrical transport on their different crystallographic directions. For each crystallographic direction, their electrical properties can change.

Most of the time, single crystal MOFs are unavailable or exceedingly difficult to contact since they are usually too small. As a result, conductivity measurements on powder samples are the most common.

Powder is usually the main product obtained in the synthesis of a MOF. Depending on the reaction conditions this powder can be amorphous or microcrystalline. In amorphous materials, components inside the solid are not periodically ordered while in microcrystalline materials the components are periodically ordered at the micrometric range. Usually, to study the electrical behavior of these materials, the powder is pressed into pellets or rods and electrical contacts are added. Grain

boundaries, surface defects, and disorder difficult electronic transport, lower conductivity and makes impossible to clearly identify the path traveled by the electrons through the pellet. However, it is a reasonable first approximation to get information on conductivity, or even the only possibility if single crystals are not available.

3.2. Measurement techniques on single crystals and powder samples

These pressed powder and single crystals are usually measured with a two-contact probe, four-contact probe, four-point probe, and van der Pauw methods (Figure 1-4). The relevant equations that allow the measurement of electrical conductivity in two-contact and four-contact probe methods are based on Eq.1-6. In two-contact probe method, the sample is usually cut into a bar/rod-like shape, where two opposite surfaces are connected to thin metal wires (gold or copper wires with a diameter of 10-100 μm) are commonly used by conductive adhesive paste (silver, gold or carbon paste) (Figure 1-4a). Voltage or current is supplied or measured through two wires. This method measures the total resistance of the sample, contacts, and wires. Because of the equivalent circuit represents a number of resistors in series (Figure 1-4e), the resistance of the sample must be significantly larger than the total resistance of the contacts and the wire leads, which thus need not to be known precisely. The typical resistance of wires and contacts is less than 100 Ω. Therefore, to measure electrical conductivity with less than 10% error, the resistance of the sample needs to be higher than 1 kΩ.

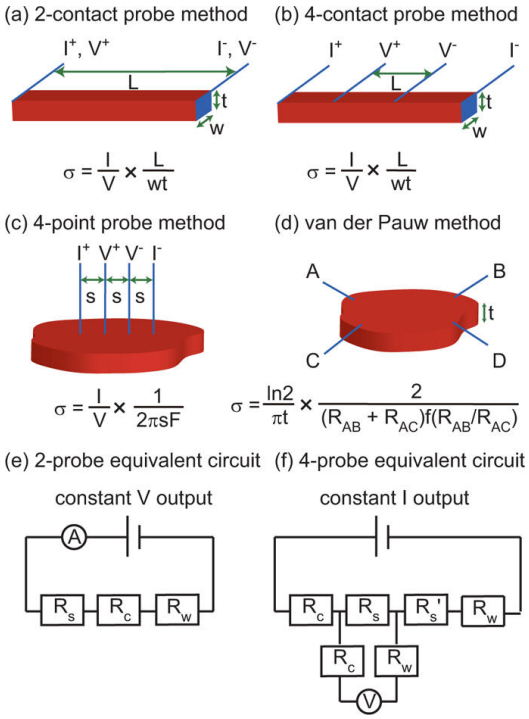

Figure 1-4 Methods for measuring the electrical conductivity on pressed powder MOFs (a-d), Red and blue areas represent samples and electrodes, respectively. I, current; V, Voltage; l, sample length; w, sample width; t, sample thickness; s, the distance between adjancent probes; σ, electrical conductivity; F and $f(R_{AB}/R_{AC})$, correction factors; +, imput; −, output. (e) Equivalent circuit for two-contact probe divice. (f) Equivalent cirucuit for four-contact probe, the four -pint probe, and van der PAuw devices. R_s, the resistance of the sample of interest; R_c, contact resistance; R_w, wire resistance; R_s, sample resistance that is not measured; A, ammeter; V, voltmeter. Extracted from ref. 47.

If the resistance of the sample is comparable or smaller than total resistance of the contacts and wires, the four-contact probes are connected to the sample (Figure 1-4b). The outer two probes supply current, while the inner two probes measure voltage. The equivalent circuit for this configuration consists of contact and wire resistors in series with a voltmeter, both parallel to the sample resistors (Figure

1-4f). This circuit eliminates contact and wire resistances and measures only the resistance of the sample as long as it is significantly smaller than the internal resistance of the voltmeter, typically on the order of tera-ohms to peta-ohms. This assumption is justified even for poorly conducting samples with a resistance exceeding 1 GΩ. This method thus allows for an accurate determination of electrical conductivity that does not depend on the resistance of the wires or contacts. The same method can be applied to highly resistive samples, although σ measurements with four-contact or two-contact probe techniques for highly resistive materials should naturally give nearly identical results.

Whereas the two- and four- contact probe techniques are ideal for single crystals, the four-point probe and van der Pauw methods are the most appropriate for measuring the electrical conductivity of irregularly shaped samples. As four-contact probe methods, both four-point contact and van der Pauw methods, eliminate contributions from the resistance of contacts and wires (Figure 1-4f). In the former, four small (i.e. point-like) probes are placed linearly onto the surface of the sample, making point contacts (Figure 1-4c). Probes typically consist of aligned equidistant metal pins. The equal spacing between pins simplifies the probe operation and the calculations. Current is supplied through the outer two probes, while voltage is measured through the inner two probes. Importantly, this technique assumes that the sample size is infinite both laterally and vertically, the contact between the four point-probes and the sample are infinitesimally small, and the sample exhibits isotropic conductivity. Practically, these assumptions are difficult to meet, thus it is necessary to apply a correction factor (F) to evaluate the electrical conductivity [Eq.1-7]:

$$\sigma = \frac{1}{2\pi sF} * \frac{I}{V} \qquad 1\text{-}7$$

where s is the probe spacing. F corrects for lateral sample dimensions, sample thickness, and placement of the probe relative to the sample edges, among others.

3.2.1. Correction Factors in Four Probe measurements

Four-point probe correction factors can be calculated by the method of images,[48–50] complex variable theory,[51] the method of Carbobino sources,[52] Poisson's equation,[53] Green's functions[54] and conformal mapping.[55–57] I will give the most appropriate factors here for samples with a regular diameter and collinear or in-line probes with equal probe spacing, s.

The total Correction Factor, F, is written as a product of three separate correction factors [Eq.1-8]:

$$F = F_1 * F_2 * F_3 \qquad 1\text{-}8$$

F_1 corrects for thickness, F_2 for lateral dimensions, and F_3 for placement of the probes relative to the sample edges. Each of these factors can be further subdivided in smaller contributions.

Sample thickness must be corrected for most measurements since samples are not infinitely thick. A detailed derivation of thickness correction factors was given by Weller.[58] If the sample consists of a semiconducting sample on a semiconductor surface, the sample should be electrically isolated from the substrate. The simplest way is to place the conductive sample on a high isolated substrate. Sample thickness is usually on the order of the probe spacing or less, the correction factor for a non-conducting bottom sample surface boundary is [Eq. 1-9]:[59]

$$F_{11}\left(\frac{t}{s}\right) = \frac{t/s}{2ln\{[sinh(t/s)]/[sinh(t/2s)]\}} \qquad 1\text{-}9$$

where t is the thickness of the sample and s is the spacing between the probes. For a conducting bottom surface, the correction factor becomes [Eq.1-10]:

$$F_{12}\left(\frac{t}{s}\right) = \frac{t/s}{2ln\{[cosh(t/s)]/[cosh(t/2s)]\}} \qquad 1\text{-}10$$

F_{11} and F_{12} are plotted in Figure 1-5. However, it is worth noting that most four-point probe measurements are made with insulating bottom boundaries.

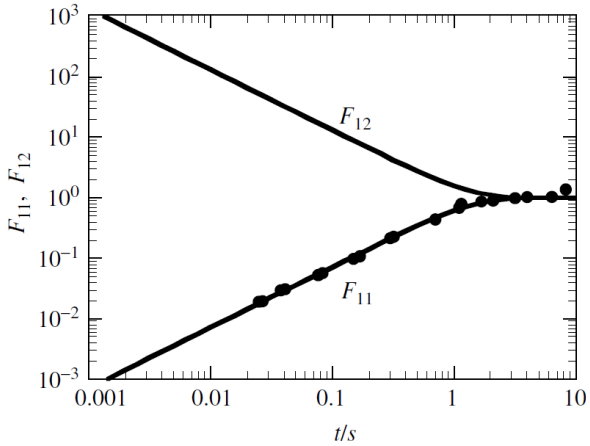

Figure 1-5 Sample thickness correction factor versus normalized sample thickness; t is the sample thickness, s the probe spacing. Extracted form [41].

Additionally, there is a factor to apply according to the shape of the sample. On circular samples of diameter D, the correction factor F_2 in Eq. 1-8 is given by [Eq.1-11]:[60]

$$F_2\left(\frac{D}{s}\right) = \frac{\ln(2)}{\ln(2) + ln\{[(D/s)^2 + 3]/[(D/s)^2 - 3]\}} \qquad 1\text{-}11$$

F_2 is plotted in Figure 1-6 for circular samples. The sample must have a diameter $D \geq 40s$ for F_2 to be unity. For a probe spacing of 1.2 mm, this implies that the sample must be at least 48 mm in diameter. Also, show in Figure 1-6 is the correction factor for rectangular samples.[45, 46]

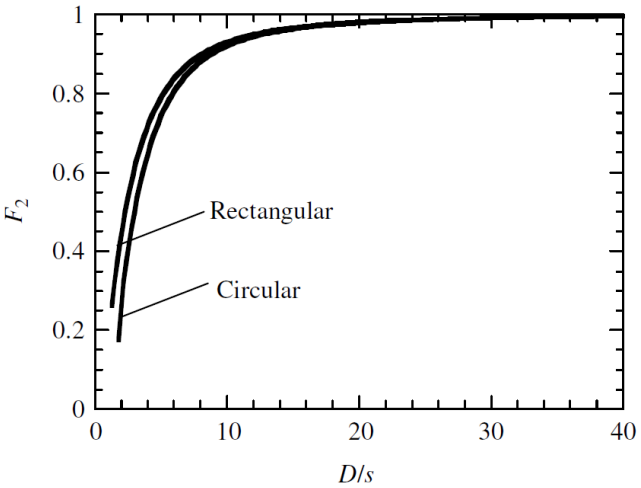

Figure 1-6 Sample diameter correction factors versus the normalized sample diameter. For circular samples: D = sample diameter; for rectangular samples: D = sample width, s = probe spacing. Extracted from [41].

Last but not least, there is factors related to the distance between the nearest probe to the edge sample. It also accounts if the probe arrangement is perpendicular or parallel to the sample edge. For perpendicular probes at a distance d, on the non-conducting boundary (i.e. sheets of glass), the correction factor is given by [Eq.1-12]:[48]

$$F_{31}\left(\frac{d}{s}\right) = \qquad \text{1-12}$$

$$\frac{1}{\left[1+\frac{1}{1+(2d/s)}-\frac{1}{2+(2d/s)}-\frac{1}{4+(2d/s)}+\frac{1}{5+(2d/s)}\right]}$$

And for parallel probes at a distance d, on the non-conducting boundary, the factor correction is given by [Eq.1-13]:[48]

$$F_{32}\left(\frac{d}{s}\right) = \frac{1}{\left[1+\frac{2}{\sqrt{1+(2d/s)^2}}-\frac{1}{\sqrt{1+(d/s)^2}}\right]} \qquad \text{1-13}$$

On the other hand, for probes perpendicular to and a distance d from conducting boundary, the factor correction is given by [Eq.1-14]:[48]

$$F_{33}\left(\frac{d}{s}\right) = \qquad \text{1-14}$$

$$\frac{1}{\left[1-\frac{1}{1+(2d/s)}+\frac{1}{2+(2d/s)}+\frac{1}{4+(2d/s)}-\frac{1}{5+(2d/s)}\right]}$$

For probes parallel to and a distance d from conducting boundary, the factor correction is given by [Eq.1-15]:[48]

$$F_{34}\left(\frac{d}{s}\right) = \frac{1}{\left[1-\frac{2}{\sqrt{1+(2d/s)^2}}+\frac{1}{\sqrt{1+(d/s)^2}}\right]} \qquad \text{1-15}$$

These correction factors are shown in Figure 1-7. For $d \geq 3s \; to \; 4s$, the correction factors F_{31} to F_{34} reduce to unity. For most four-point probe measurements this condition is easily satisfied. Correction

factors F_{31} to F_{34} only become important for small samples in which the probe is, of necessity, close to the sample boundary.

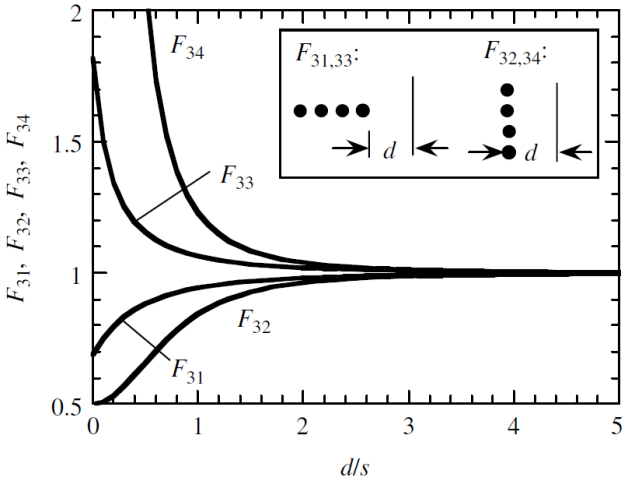

Figure 1-7 Boundary proximity correction factors versus normalized distance d (s = probe spacing) from the boundary. F_{31} and F_{32} are non-conducting boundaries, F_{33} and F_{34} are for conducting boundaries. Extracted from ref. 41.

For very thin samples that satisfy the conditions for F_2 and F_3 to be approximately unity, we can obtain from Eq.1-7, 1-8 and 1-11, the electrical conductivity as [Eq.1-16]:

$$\sigma = \frac{\ln(2)}{\pi * t} * \frac{I}{V} = \frac{2 * 10^{-1}}{t} * \frac{I}{V} \qquad 1\text{-}16$$

Four-point probe measurements are also subject to further corrections factors depending on how the measuring instruments are connected to the probes, for instance in Eq. 1-16, the factor of $2 \cdot 10^{-1}$ is for collinear probes with the current flowing into probe 1, out of probe 4, and voltage sensed across probes 2 and 3. For the current applied and the voltage sensed across other probes, different correction factors should be applied.[61]

As an example, it can be pedagogical to calculate the correction that applies to typical circular sample with non-conductive boundary and non-conductive substrate like the ones studied during this thesis (Table 1-1).

Table 1-1 Experimental dimensions for a typical 2 probe measurements presented in this thesis.

Parameters	Value (cm)
s	0.12
t	0.035
D	1.33
$d\ perpendicular$	0.49

Using subfactors F_{11}, F_2 and F_{31} according to Eq. 1-10, Eq. 1-11 and Eq. 1-12 respectively. We can obtain the values reported in Table 1-2.

Table 1-2 Values obtained from each one of the sub correction factors for a circular sample with non-conductive boundary and the non-conductive substrate with dimensions reported in Table 1-1.

Subfactors	Value
F_{11}	0.207
F_2	0.935
F_{31}	0.995

Using these sub-correction factors, and following the Eq. 1-8, the overall correction Factor (F) can be calculated:

$$F = F_{11} * F_2 * F_{31} = 0.207 * 0.935 * 0.995 = 0.193$$

Due to the fact that $F_2, F_{31} \approx 1$, F can be considered as F_{11}. It shows that for this kind of sample the critical factor is the related with the thickness of the sample, t, as long as the four-point probes are positioned in the center of the sample and the factor diameter is above 1.33 cm. Otherwise, the correction should be recalculated.

Up to this point, I have introduced some techniques and equations that are necessary to measure the electrical conductivity of bulk samples. In the next section, I will introduce some specific techniques to measure the electrical conductivity of MOF thin films.

3.3. Measurement of electrical conductivity in thin films

Due to MOFs having high resistance, it is easy to find resistances near to 1kΩ or higher. As I mentioned before, it is enough to measure this kind of samples using just two contacts. In here we are going to consider two particular possibilities for doing that in the case of thin films. Each one of them is with different orientation of the film and the contacts: lateral, in which electrodes are fixed laterally and the film is considered to be relatively conductive (e.g. below 1 MΩ with a gap of at least 2.5µm) (Figure 1-8A), and vertical, in which electrodes are fixed vertically and the film is considered low conductive (e.g. few nanometer thick films with resistance around or above 1 GΩ). Moreover, this kind of configuration is also used to study stacked multilayered samples (e.g. OLEDs) (Figure 1-8B) where the current needs to be forced to pass through all the layers. On the vertical configuration, the gap is determined by the thickness of the film while in the lateral configuration is determine by the gap between electrodes.

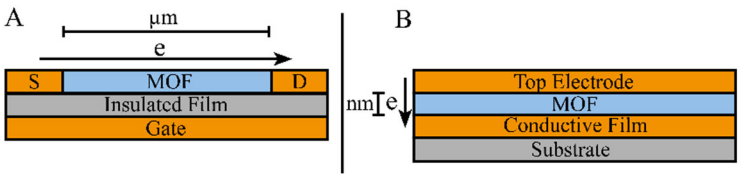

Figure 1-8 Schematic picture in which shows how electrons travel through (A) lateral and (B) vertical configurations.

3.3.2. Charge transport on thin films measured laterally using Field-Effect Transistor type devices

The lateral configuration can include two or three terminals. On the case of three terminals it is also called Field Effect Transistor (FET) device/configuration[39]. A FET consists of a semiconductor, a dielectric and three conducting electrodes (gate, source, and drain). The device can be viewed as a planar capacitor, formed by the gate electrode and semiconductor on both sides of a dielectric (Figure 1-9). V_g is used to modulate the current flowing laterally. A FET setup can be used to characterize electrically conductive samples up to $\sigma \geq 5 \cdot 10^{-7}\ S \cdot cm^{-1}$ and usually includes gaps of up to 20 µm between contacts. When this setup is used, the MOF thin film is placed between the two lateral contacts. Depending on how the electrodes are placed different options are available: bottom contacts and bottom gate (BC-BG), bottom contacts and top gate (BC-TG), and top contacts and bottom gate (TC-BG). Nevertheless, for soft materials, the most used is BC-BG, because it is less aggressive with the film.

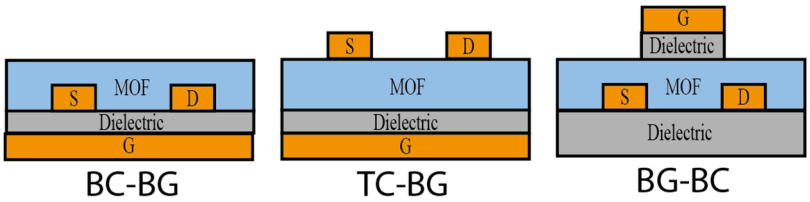

Figure 1-9 Three common geometries that are widespread for FET-type measurements. From left to right: bottom contacts and bottom gate (BC-BG), bottom contacts and top gate (BC-TG), and top contacts and bottom gate (TC-BG). Redraw from ref. 62.

The electrical conductivity on a lateral device is calculated adapting Eq. 1-6 to Eq.1-17:

$$\sigma = \frac{S * I}{V * H * L * N} \qquad 1\text{-}17$$

where S, L, and N, are the gap between electrodes, the length of the electrodes and number of interdigitated channels (Figure 1-10), respectively and H, the thickness of the film. As usual, the voltage V, and electrical current, I, are extracted from the I-V curves when the sample is measured.

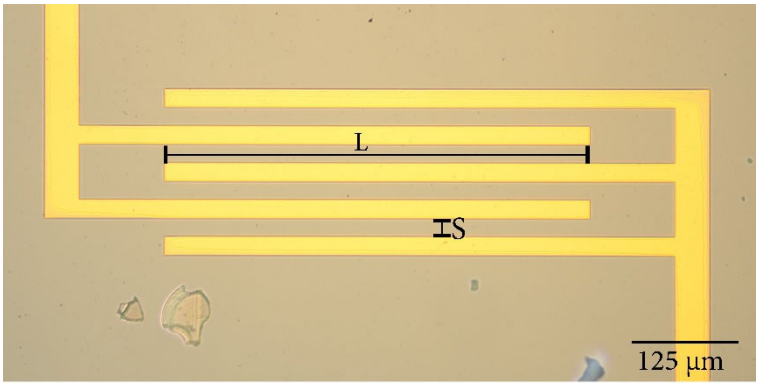

Figure 1-10 Picture of the contacts of a FET device including four channels like the ones used in this PhD thesis. The parameters useful to calculate the electrical conductivity: L, electrode length; S, the gap between electrodes.

3.3.3. Charge transport on thin films measured vertically using liquid contacts

The vertical configuration is well adapted to measure the electrical conductivity of low conductive materials whose thickness can be precisely controlled (i.e. SAMs). In that case, even when conductivity is very low, it become measurable when a small gap (small thickness) between contacts is used. It is also used in situations when multilayers are present (i.e. solar cells) and the electrons are forced to cross through the layers. In principle the architecture of this set-up consists of a conductive substrate on top of which the film will be deposited. As a

top contact we can use different options (Figure 1-11). For instance, conductive AFM allows measuring small areas (i.e. sample-size up to 250 μm^2)[63], if conductive metal contacts are deposited large areas can be measured (i.e. sample-size about 25 mm^2)[44] but the probability of short circuit is very high, especially for very thin films. Alternatively, liquid metal contacts (i.e. Mercury Drop and Eutectic Gallium-Indium Alloys) allow measuring relatively large areas with low probability of short circuit[38],[61]. Liquid metals are cheap and liquid metal contacts are well adapted to the soft porous nature of MOF films. For that reason, we decided to develop this contacting technique in the lab.

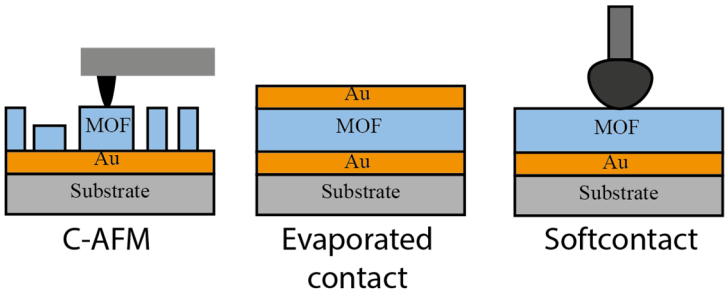

Figure 1-11 Architecture for vertical setup and some different kind of possible top contacts. From left to right: Conductive Tip of AFM, Evaporated contact and the liquid metal contact.

The electrical conductivity on a vertical device is calculated using Eq.1-6:

$$\sigma = G * \frac{l}{A} = \frac{I}{V} * \frac{l}{A} \qquad 1\text{-}6$$

where A is the area value of the top contact and l the thickness of the film. The typical area of the top contact is calculated from the diameter of the drop in contact with the film using a camera (Figure 1-12).

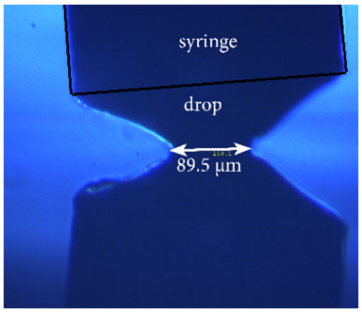

Figure 1-12 Picture of a EGaIn liquid metal contact with his diameter.

To consider the variable size of the contacts, the current density (J) is calculated instead of the electrical conductivity. The current density is given by Eq.1-18:

$$J(V) = \frac{I(V)}{A_g} \qquad 1\text{-}18$$

where $I(V)$ is the voltage-dependent electrical current and A_g is the geometrical contact area. The value of $J(V)$ does not depend on A_g which, in principle, make the comparison of data measured across different junctions possible.

Up to this point, I have introduced two techniques commonly used to measure the electrical conductivity of MOF thin films. However, to integrate these materials into devices compatible with current CMOS technology and to apply these techniques, it is necessary to process these materials as thin films above a solid support. In the next section, I will show how this is done.

3.4. Fabrication methods for MOF thin films

To consider molecular materials as a component of an electronic device compatible with CMOS technology, it is necessary to understand how

these materials function within the device and how they interface with it. On this order of ideas, it is necessary to deposit and study these materials as thin films.

For MOFs, the quality of the film can be changed drastically depending on method used deposited it on the substrate. In the following sections, I will review some of the techniques used for the deposition of MOFs as films and ultrathin films.

These techniques are divided depending on the thickness accuracy needed and how the final material is formed. These are separated on three groups: (i) **Deposition from colloids/colloidal dispersions** where the MOF is previously synthesized as colloidal particles and then deposited on the surface, (ii) **Direct Synthesis** of micrometer-thick films that are generally grown by seeding methods with poor control over the orientation of the crystals and (iii) **Layer-by-Layer (LbL)** (nanometer-thick), films grown by sequential deposition methods.[13,65–68] As we will see later, some of those methods can be improved by functionalizing substrates to promote and direct the nucleation, orientation, and structure of the resulting film.

3.4.4. Deposition from colloidal materials.

This kind of procedure is composed of two steps. The first step where the MOF colloidal particles are formed in solution, and, the second one, in which MOF particles are deposited on the surface. Dip-coating, drop-casting and spin coating are the techniques commonly used to deposit MOFs particles that range up to 500nm.

Fabrication of MOF films by this method has been used among others by Sanchez, Serre, and co-workers.[69–71] They prepared MOF particles with well-defined size and transferred them onto a silicon substrates by dip-coating. They demonstrated this concept experimentally with three different MOF structures: MIL-89 [$Fe_6O_2Cl_2(BDC)_6$] (Figure 1-13A),[69] MIL-101 [$Cr_3OF(BDC)_2(H_2O)_2$] (Figure 1-13B),[70] and ZIF-8 [$Zn(Cu_4H_5N_2)_2$] (Figure 1-13C).[71] Depending on the concentration of the particles in solution, 2-3 layers of particles were deposited at the same time. Repetition of the dip-coating process led to thicker films and allowed close control of the thickness. However, the mechanical resistance of such films that are not rigidly linked to their substrates is moderated. The advantage of this method is that particle size,

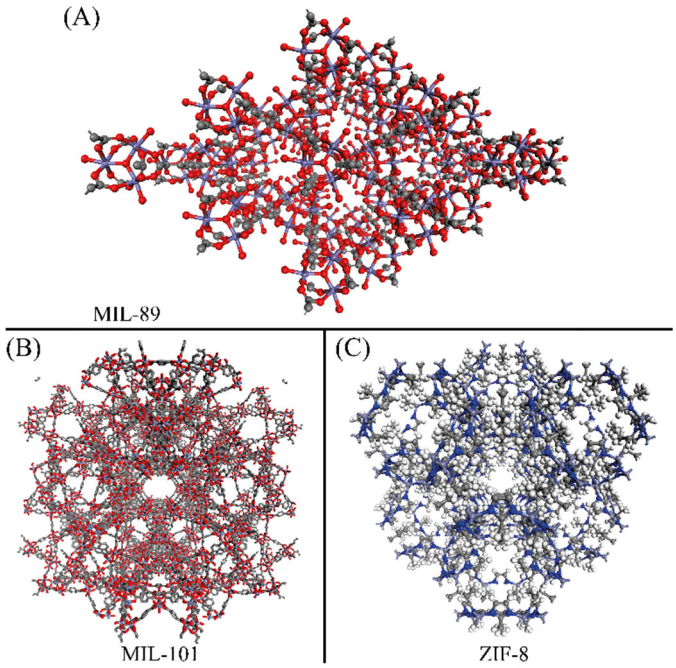

Figure 1-13 Crystal structures of (A) MIL-89 (DN: 1152929), (B) MIL-101 (DN: 605510), (C) ZIF-8 (DN: 864310), extracted from CCDC.

crystallinity, and the presence of intergrain mesoporosity. On the other hand, it demands the preparation of stable colloidal dispersions.

3.4.5. In-situ Growth/deposition in the MOF reaction conditions.

In this case, substrate, solvent, and reactants are kept together in the same reactor during the MOF synthesis. When the reaction has finished, the film is formed on the substrate most often along with a powder precipitated at the bottom of the reactor container.[72,73] Zacher et al.[72] showed that the nature of the surface, and especially its acid/base properties, influence whether a film can grow or not. The authors suggested that binding between the surface and the film is mediated by the organic linker, and therefore, a MOF that contains acid linkers like HKUST-1 cannot grow on acidic surfaces such silica. However, a MOF that contains both acidic and basic linkers such as [Zn_2(BDC-Br)$_2$(DABCO); (DABCO = 1,4-diazabicyclo[2.2.2]octane)]

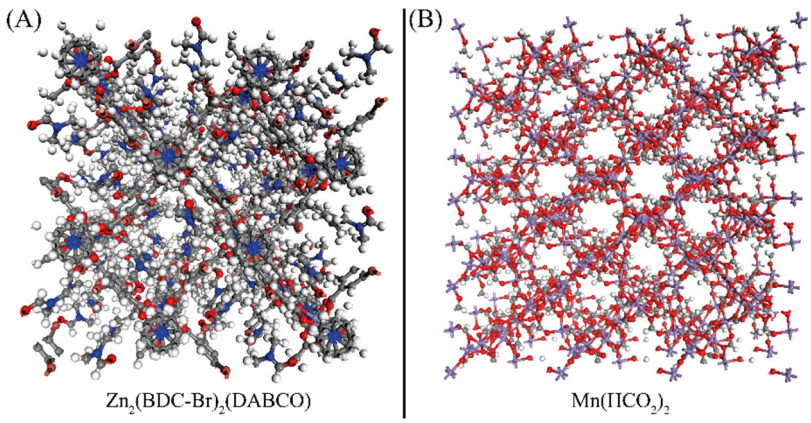

Figure 1-14 Crystal Structure of (A) $Zn_2(BDC)_2(DABCO)$ extracted from ref. 74 and (B) $Mn(HCO_2)_2$ extracted from ref. 75.

(Figure 1-14A) can grow on both silica and alumina. Arnold et al.[73]

reached similar conclusions by studying $Mn(HCO_2)_2$ (Figure 1-14B) growth on alumina and graphite.

As a result, the use of organic molecules has been proposed to improve heterogeneous nucleation and growth. Huang et al.[76] treated a porous Titania support with 3-aminopropyltriethoxysilane (APTES). This molecule can bind to the surface by the silane group and to ZIF-22 [$Zn(ABLM)_2$; ABLM = 5-azabenzimidazole] (Figure 1-15A) crystals through the terminal amino group. As a result, thick (40µm) and well-intergrown films of higher quality than the ones obtained without the linker were obtained. The same phenomenon has been observed for ZIF-90 [$Zn(C_4H_3N_2O)_2$][77] (Figure 1-15B).

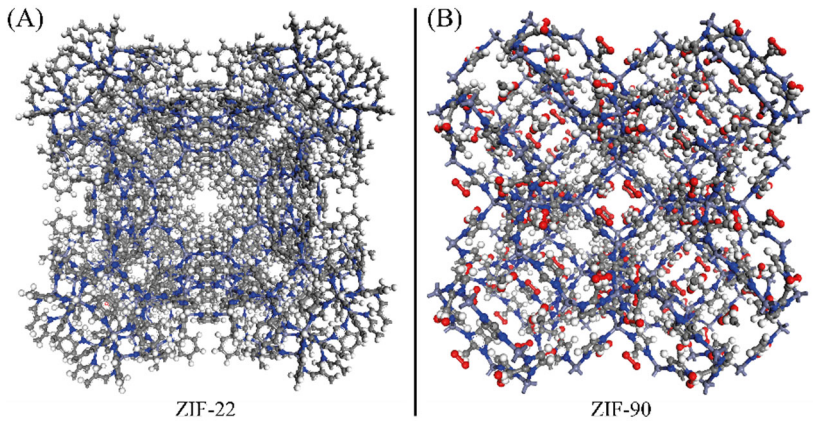

Figure 1-15 Crystal structure of (A) ZIF-22 (DN: 647001) extracted from CCDC and ZIF-90 extracted from ref. 78.

Usually, MOF synthesis takes place in solvothermal conditions. However, ***microwave-heating*** approaches have been developed for bulk materials synthesis and have been extended to films.[79] The advantage of this method over conventional heating is the increased nucleation rate. Indeed, a few hours is enough to archive full crystallization. This method was introduced by Yoo et al.[80] using a

substrate (porous alumina) coated with a conducting layer, such as graphite or gold, and immersed in a MOF-5 [$Zn_4O(BDC)$] (Figure 1-16A) precursors solution. Upon microwave irradiation (5-30s), the temperature of the conductive layer increased rapidly and introduced fast heterogeneous nucleation for MOF-5 crystals. Later, Bux et al.[81] used the microwave-assisted deposition to prepare a 40μm thick ZIF-8 film on porous Titania that exhibits molecular sieving properties.

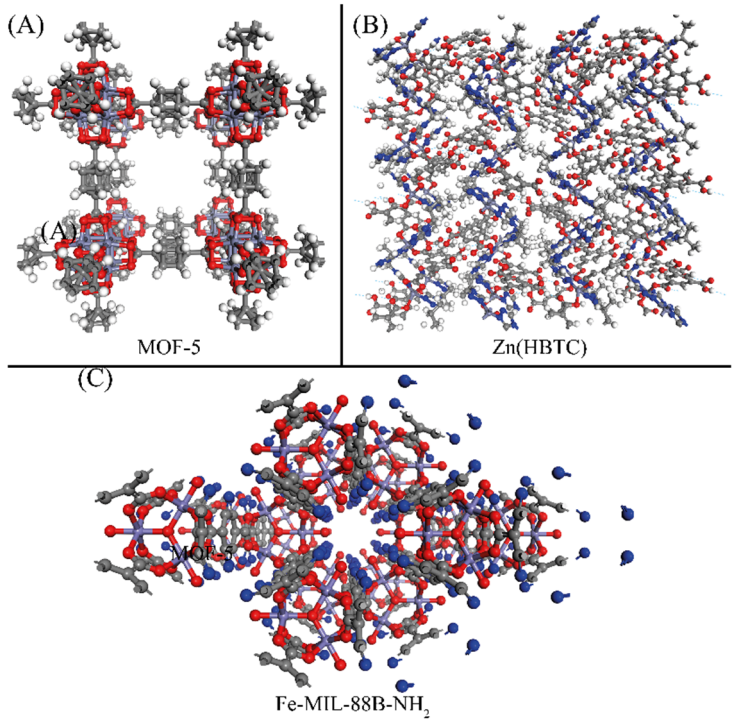

Figure 1-16 Crystal structure of (A) MOF-5 (DN: 1487331), (B) Zn(HBTC) (DN: 1455328), (C) Fe-MIL-88B-NH_2. (DN: 647646). All structures extracted from CCDC.

A variation of the above ideas is the use of ***Gel-layer synthesis*** to better control nucleation over the surface**.** This method was originally applied to MOFs by Yaghi et al. to grow Zn(HBTC) (HBTC = 5-carboxy-benzene-1,3-dicarboxylate dianion) (Figure 1-16B).[82] Later,

Schoedel et al.[83] employed this method to grow HKUST-1 and Fe-MIL-88B-NH_2 [H_2(NH_2-BDC)] (Figure 1-16C) films on a -COOH or -OH terminal alkanethiolate SAM functionalized Au-substrates. They immersed the substrates in poly (ethylene oxide) gel loaded with metal-ion precursor (Cu^{2+} or Fe^{3+}) and then carefully added the linker solution (H_3BTC or H_2(NH_2-BDC) on the top of the gel layer. The morphology and thickness of the resulting MOF film could be controlled by the length of the poly(ethylene oxide) and the concentration of the metal ions in the gel. The thickness of Fe-MIL-88B-NH_2 film was estimated to be 40 nm.

An electrochemical method to control the reaction rate was originally developed by researchers at BASF.[84] The principle was based on supplying the metal-ion, by anodic dissolution to a solution that contained the organic ligand and a conducting salt. Careful modification of the conditions used to electrochemically produce bulk MOF material enables the preparation of thin films. This process was demonstrated with HKUST-1, applying an anodic voltage to the copper electrode in the presence of a solution containing BTC and methyltributylammnium methyl sulfate (MTBS) as conduction salt. Films with thicknesses in the range 2 to 50 μm of well packed HKUST-1 crystals were obtained. The thickness of the film could be changed modifying the synthesis conditions.[85]

3.4.6. Layer-by-Layer (LbL)

Protocols and deposition methods of MOFs described before, are very dependent on the crystallite size because of competition between crystal nucleation and growth. This consumes adjacent building blocks giving rise to non-closed films with grainy textures and thickness

above to 40 nm. In the following section, we will review some strategies that have been devised to separate crystal nucleation from growth like the **Assisted Layer-by-Layer method** and the combination of **Langmuir Blodgett (LB) and LbL method**.

3.4.6.1.Assisted Layer-by-layer.

In this strategy, a substrate is exposed to metal and ligand solutions individually. This gives each of components the opportunity to saturate all deposition sites without the formation of new nuclei at the surface or in solution.[86] Between each step, the sample is rinsed with solvent to remove the uncoordinated precursors. The thickness film can be well-controlled by adjusting the number of cycles. This technique has the potential of depositing highly oriented films and transferring one-unit cell per transfer cycle allowing for a nanometric control of the thickness of the film. Such methods result in more homogeneous surface coverage and crystallinity with better potential for the study of physical/chemical properties and the applications on devices.[13,65–68,87] As in the previous cases, the substrate is usually modified with a SAM to improve growth and homogeneity of the films.[88] Several techniques have been born to control the sequential addition of metal and ligand, namely dipping, pump, spray, and spin-coating.

Dipping method. In the dipping method, the functionalized substrate is immersed in three containers with the metal salt, organic ligand, and rising solutions as shown in Figure 1-17. This method was reported for first time by Mallouk et al. on the sequential deposition of Ni(bpy){Pt(CN)$_4$} (bpy = 2,2'-bipyridine).[89] This process can also be carried out manually[90] or automatized using a robot.[91] HKUST-1 was synthesized by sequentially immersing the substrate in Cu(OAc)$_2$ (OAc

= Acetoxy Group) and H_3BTC ethanolic solutions for 30 and 60 min respectively, between each immersion the sample was rinsed with ethanol and dried with N_2 stream.[90] For the case of the automatized method, times were 10 and 15 min respectively, and a rinse time of 2 min and showered with pure ethanol for 3 s.[91]

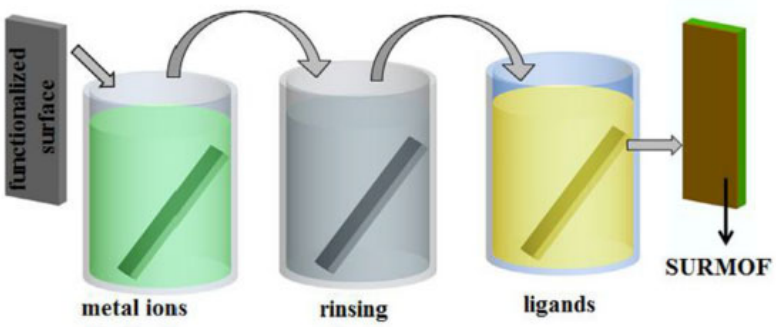

Figure 1-17 The diagram of dipping LbL method for SURMOFs preparation. Extracted from ref. 90.

A continuous flow method. was used by Wöll et al. to synthesize Cu and Zn-MOF-2 [M(BDC); M = Cu or Zn] ultrathin films (Figure 1-18A).[92] In this report, four pumps were connected to a sealed chamber. As shown in Figure 1-18B, 2 pumps for controlling the reaction time with the precursor ($M_2(CH_3COO)_2{\cdot}H_2O$ (M= Cu or Zn)) and H_2BDC to 30 and 60 minutes respectively. Another one, to control the rinsing time, and the fourth one was responsible for pumping out the solution from the reactor.

In addition, Quartz Crystal Microbalance (QCM) and Surface Plasmon Resonance (SPR) have been widely reported as complementary methods to monitor the amount of material deposited during the process.[90,93] For example, Shekhah has recorded the sequential injection of $Cu(Ac)_2$ (Ac = Acetyl group) and H_3BTC and then rinsed

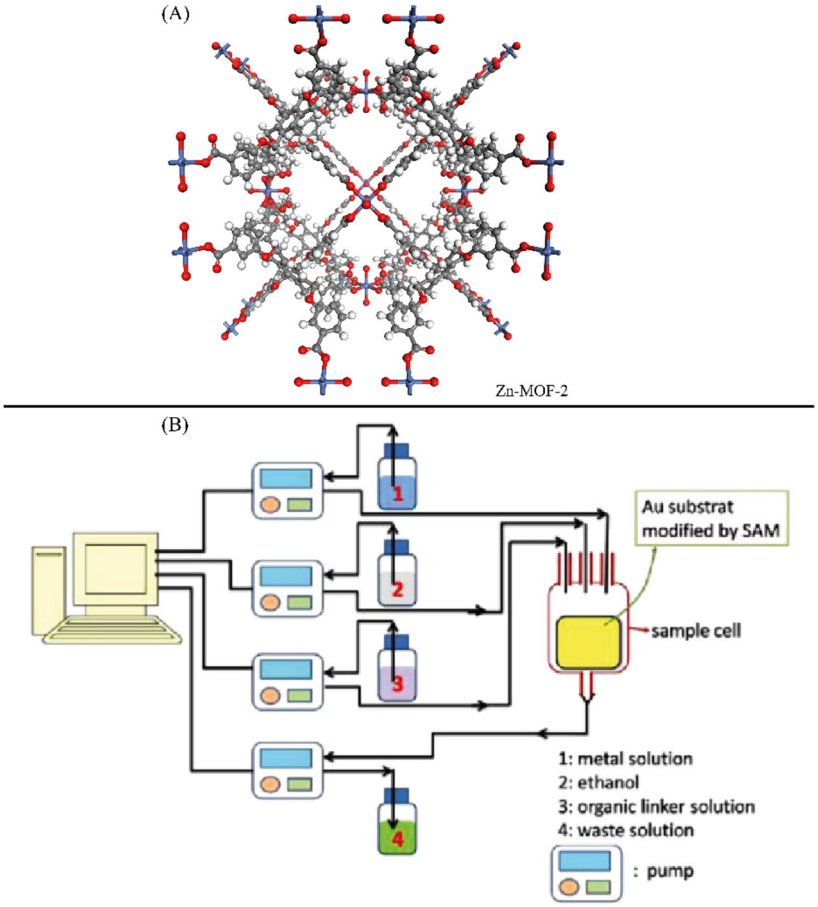

Figure 1-18 (A) Crystal structure of Zn-MOF-2 (DN: 957606) extracted from CCDC. (B) The diagram of the pump system for the automated Layer-by-Layer growth of SURMOFs. Extracted from ref. 92.

with ethanol on a functionalized QCM electrode.[93] Moreover, these techniques can be used to obtain information about film porosity[26,85,94] when the growth has finished.

The spray method is related to the dipping method. In this case, a spray system is adapted (Figure 1-19)[95] to dispense the reagents. This approach has been used to grow MOFs ultrathin film with fast speed and keeping a high degree of crystallinity and orientation. In this

method, there are three nozzles for spraying the solutions including metal salts, organic ligands, and rising solvent, respectively.

As a proof of concept, HKUST-1 was again selected to demonstrate the efficiency of this method by Wöll et al.[95] Carboxylic acid SAM-modified substrates were alternately exposed to aerosol mixtures containing $Cu(OAc)_2$ (10 s) or (H_3BTC) (20 s) produced by spray nozzles. Like the other methods, the removal of residual reactants (metal source, organic linkers) was achieved by exposing the substrate to an aerosol produced from the pure solvent.

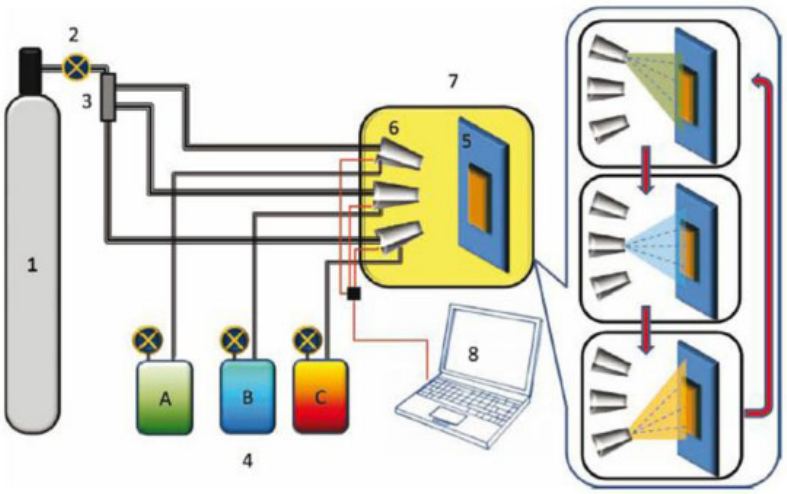

Figure 1-19 The diagram of the automatic spray method for LbL growth of SURMOF: (1) Gas supply, (2) gas flow controller (3) three-way valve gas distributor (4) (A–C) solutions storage containers (5) sample holder (6) dosing valves, (7) spray chamber, (8) PC. Extracted from ref. 95.

The Spin-coating method is an effective way to prepare thin and homogeneous films out of solutions on flat substrates.[96,97] In 2009, Vozar et al. reported an automated spin-assisted layer-by-layer assembly. In this system, a substrate is rotated rapidly, and precursors

and cleaning solution are deposit onto the substrate, typically using a nozzle impinging upon the center of the substrate. The rapid spinning of the sample produces a thin layer over the full substrate area. This setup was originally used to fabricate polymer-clay nanocomposites[97] and recently adapted by Shekhah et al.[98] to grow $Cu_2(BDC)_2$ thin films (Figure 1-20A). A SAM functionalized substrate was placed on a vacuum chuck and subsequently spin-coated in a continuous mode (Figure 1-20B) during the addition of 50µl of $Cu_2(CH_3COO)_4$ solution for 5 s followed by 50 µl of H_2bdc solution for 8 s. The substrate was washed with 50µl of pure ethanol between each step. ZIF-8 and HKUST-1 ultrathin films have been grown using the same setup. [98]

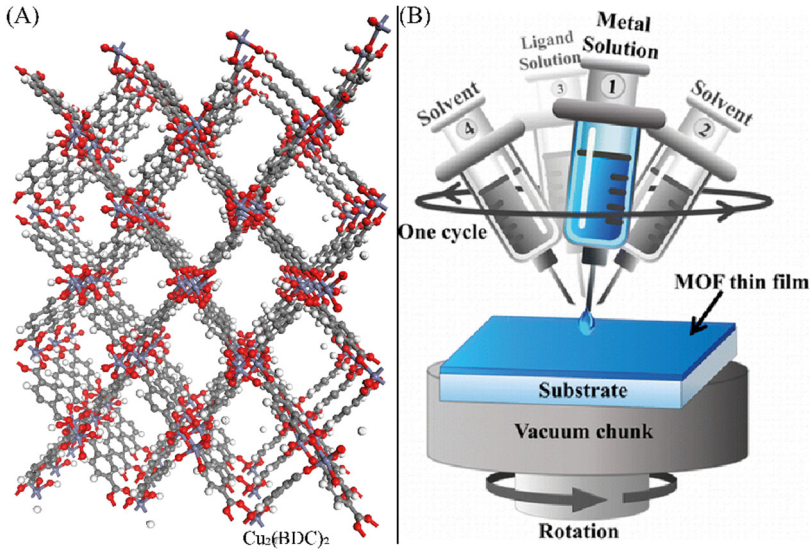

Figure 1-20 (A) Crystal structure of $Cu_2(BDC)_2$ modified from $Zn_2(BDC)_2$ (DN: 1165060) extracted from CCDC . (B) Schematic representation of the setup employed for the fabrication of MOF thin films using the LbL approach adapted to the spin-coating method. Extracted from ref. 98.

3.4.6.2.Langmuir Blodgett (LB) as LbL method

Last but not least, a method combining some of the ideas discussed above was introduced by Kitagawa et. al.[99] for depositing 2D-MOF on planar substrates. This method is carried out in two steps, in the first one the MOF is synthesized at the air-water interface and next transferred to the film. In this way only, a limited amount of preformed material is transferred in each step. First, they assembled at the

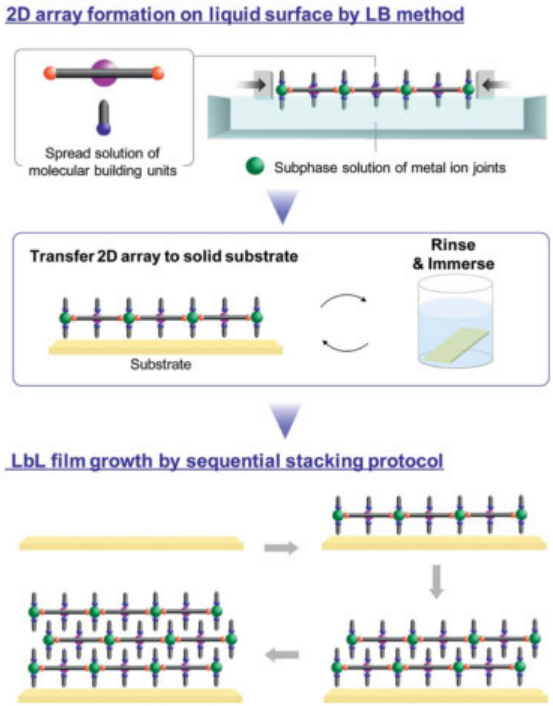

Figure 1-21 Schematic illustration of the representative steps involved in the combined LB–LbL film fabrication technique. Extracted from ref. 99.

air-water interface 5,10,15,20-tetrakis(4-carboxyphenyl)porphyrinato cobalt (II) (CoTCPP), copper (II) ions as a metal node and pyridine molecules (py) as a coordination-saturating ligand to form CoTCPP-py-Cu layers. The fabrication protocol was started by

spreading a solution of CoTCPP and py onto an aqueous solution of $CuCl{\cdot}2H_2O$ at room temperature. Next, the floating components were compressed to obtain an ultrathin uniform MOF layer. Finally, the 2D-MOF layers were transferred to a substrate. The thickness of the final film can be carefully controlled as a function of the number of transfers. To transfer this film, the substrate is immersed parallel to the film at room temperature (Figure 1-21). Once transferred, the substrate with CoTCPP-py-Cu sheet was rinsed with flowing distilled water, immersed in distilled water for 3 min, and dried by blowing nitrogen. This process was repeated to obtain the thickness desired.

As we will see later, this is the method we chose for the growth of Cu-CAT-1 and some LbL methods for the growth of Hoffman Clathrate SCO-CP with good coverage and a very fine control of their thicknesses between 1 to 60 nm.

4. Bibliography

1. Waldrop, M. M. The chips are down for Moore's law. *Nature* **530**, 144–147 (2016).

2. Intel. Intel® 14 nm Technology. *Intel* (2015). Available at: https://www.intel.com/content/www/us/en/ silicon-innovations/intel-14nm-technology.html. (Accessed: 3rd October 2018)

3. Chiang, C. K. *et al.* Electrical conductivity in doped polyacetylene. *Phys. Rev. Lett.* **39**, 1098–1101 (1977).

4. Wudl, F., Wobschall, D. & Hufnagel, E. J. Electrical Conductivity by the Bis-1,3-dithiole-Bis-1,3-dithiolium System. *J. Am. Chem. Soc.* **94**, 670–672 (1972).

5. Miller, J. S. Molecular Materials. *Science* **262**, 1460–1460 (1993).

6. Bruce, D. W. (Editor), O'Hare, D. (Editor) & Walton, R. I. (Editor). *Molecular Materials*. *John Wiley & Sons, Ltd* (Wiley, 2010).

7. Hönicke, I. M. *et al.* Balancing Mechanical Stability and Ultrahigh Porosity in Crystalline Framework Materials. *Angew. Chemie Int. Ed.* **57**, 13780–13783 (2018).

8. Furukawa, H., Cordova, K. E., O'Keeffe, M. & Yaghi, O. M. The chemistry and applications of metal-organic frameworks. *Science* **341**, 1230444 (2013).

9. Li, J. R. *et al.* Carbon dioxide capture-related gas adsorption and separation in metal-organic frameworks. *Coord. Chem. Rev.* **255**, 1791–1823 (2011).

10. Collins, D. J. & Zhou, H.-C. Hydrogen storage in metal-organic frameworks. *J. Mater. Chem.* **17**, 3154–3160 (2007).

11. Li, J. R., Kuppler, R. J. & Zhou, H. C. Selective gas adsorption and separation in metal-organic frameworks. *Chem. Soc. Rev.* **38**, 1477–1504 (2009).

12. Lee, J. *et al.* Metal-organic framework materials as catalysts. *Chem. Soc. Rev.* **38**, 1450–1459 (2009).

13. Shekhah, O., Liu, J., Fischer, R. A. & Wöll, C. MOF thin films: Existing and future applications. *Chem. Soc. Rev.* **40**, 1081-1106 (2011).

14. Nasalevich, M. A., Van Der Veen, M., Kapteijn, F. & Gascon, J. Metal-organic frameworks as heterogeneous photocatalysts: Advantages and challenges. *CrystEngComm* **16**, 4919–4926 (2014).

15. Stavila, V., Talin, A. A. & Allendorf, M. D. MOF-based electronic and opto-electronic devices. *Chem. Soc. Rev.* **43**, 5994-6010 (2014).

16. Allendorf, M. D., Schwartzberg, A., Stavila, V. & Talin, A. A. A roadmap to implementing metal-organic frameworks in electronic devices: Challenges and critical directions. *Chem. - A Eur. J.* **17**, 11372–11388 (2011).

17. Campbell, M. G., Sheberla, D., Liu, S. F., Swager, T. M. & Dincă, M. Cu_3(hexaiminotriphenylene)$_2$: An Electrically Conductive 2D Metal-Organic Framework for Chemiresistive Sensing. *Angew. Chemie Int. Ed.* **54**, 4349–4352 (2015).

18. Campbell, M. G., Liu, S. F., Swager, T. M. & Dincă, M. Chemiresistive Sensor Arrays from Conductive 2D Metal-Organic Frameworks. *J. Am. Chem. Soc.* **137**, 13780-13783 (2015).

19. Sheberla, D. *et al.* Conductive MOF electrodes for stable supercapacitors with high areal capacitance. *Nat. Mater.* **16**, 220-224 (2017).

20. Choi, K. M. *et al.* Supercapacitors of nanocrystalline metal-organic frameworks. *ACS Nano* **8**, 7451–7457 (2014).

21. Férey, G. *et al.* Mixed-valence Li/Fe-based metal-organic frameworks with both reversible redox and sorption properties. *Angew. Chemie - Int. Ed.* **46**, 3259–3263 (2007).

22. Wiers, B. M., Foo, M. L., Balsara, N. P. & Long, J. R. A solid lithium electrolyte via addition of lithium isopropoxide to a metal-organic framework with open metal sites. *J. Am. Chem. Soc.* **133**, 14522–14525 (2011).

23. Zhang, Z., Yoshikawa, H. & Awaga, K. Monitoring the solid-state electrochemistry of Cu(2,7-AQDC) (AQDC = anthraquinone dicarboxylate) in a lithium battery: Coexistence of metal and ligand redox activities in a metal-organic framework. *J. Am. Chem. Soc.* **136**, 16112-16115 (2014).

24. Aubrey, M. L. & Long, J. R. A Dual-Ion Battery Cathode via Oxidative Insertion of Anions in a Metal-Organic Framework. *J. Am. Chem. Soc.* **137**, 13594–13602 (2015).

25. Zhang, Z., Yoshikawa, H. & Awaga, K. Discovery of a 'bipolar Charging' Mechanism in the Solid-State Electrochemical Process of a Flexible Metal-Organic Framework. *Chem. Mater.* **28**, 1298–1303 (2016).

26. Liu, J. *et al.* Photoinduced Charge-Carrier Generation in Epitaxial MOF Thin Films: High Efficiency as a Result of an Indirect Electronic Band Gap? *Angew. Chemie - Int. Ed.* **54**, 7441-7445 (2015).

27. Erickson, K. J. *et al.* Thin film thermoelectric metal-organic framework with high seebeck coefficient and low thermal conductivity. *Adv. Mater.* **27**, 3453–3459 (2015).

28. Panda, T. & Banerjee, R. High charge carrier mobility in two dimensional indium (III) isophthalic acid based frameworks. *Proc. Natl. Acad. Sci. India Sect. A - Phys. Sci.* **84**, 331–336 (2014).

29. Huang, X. *et al.* A two-dimensional π–d conjugated coordination polymer with extremely high electrical conductivity and ambipolar transport behaviour. *Nat. Commun.* **6**, 7408 (2015).

30. Ko, M., Mendecki, L. & Mirica, K. A. Conductive two-dimensional metal-organic frameworks as multifunctional materials. *Chem. Commun.* **54**, 7873–7891 (2018).

31. Chen, L. *et al.* Elucidating the Breathing of the Metal–Organic Framework MIL-53(Sc) with ab Initio Molecular Dynamics Simulations and in Situ X-ray Powder Diffraction Experiments. *J. Am. Chem. Soc.* **135**, 15763–15773 (2013).

32. Hummel, R. E. *Electronic Properties of Materials*. *Development* **134**, (Springer New York, 2011).

33. Grosso, G. & Parravicini, G. P. Optical and Transport Properties of Metals. in *Solid State Physics* 483–528 (Academic Press, 2014).

34. Grosso, G. & Parravicini, G. P. Transport in Intrinsic and Homogeneously Doped Semiconductors. in *Solid State Physics* 577-608 (Academic Press, 2014).

35. Stallinga, P. Electronic transport in organic materials: Comparison of band theory with percolation/(variable range) hopping theory. *Adv. Mater.* **23**, 3356–3362 (2011).

36. Mott, N. F. Conduction in non-crystalline materials. *Philos. Mag.* **19**, 835–852 (1969).

37. Galbiati, M. *Molecular Spintronics*. *Physica E: Low-dimensional Systems and Nanostructures* (Springer International Publishing, 2016).

38. Hoffmann, R. Interaction of Orbitals through Space and through Bonds. *Acc. Chem. Res.* **4**, 1–9 (1971).

39. Stassen, I. *et al.* An updated roadmap for the integration of metal-organic frameworks with electronic devices and chemical sensors. *Chem. Soc. Rev.* **46**, 3185–3241 (2017).

40. Franssila, S. *Introduction to Microfabrication*. *John Wiley & Sons, Ltd* (Wiley, 2010).

41. Schroder, D. K. & Rubin, L. G. Semiconductor Material and Device Characterization. *Physics Today* **44**, (1991).

42. Roth, S. & Carroll, D. *One-dimensional metals: Conjugated polymers, organic crystals, carbon nanotubes and graphene*. *One-Dimensional Metals: Conjugated Polymers, Organic Crystals, Carbon Nanotubes and Graphene* (Copyright © 2015 Wiley-VCH Verlag GmbH & Co. KGaA, 2015).

43. Chiechi, R. C., Weiss, E. A., Dickey, M. D. & Whitesides, G. M. Eutectic gallium-indium (EGaIn): A moldable liquid metal for electrical characterization of self-assembled monolayers. *Angew. Chemie - Int. Ed.* **47**, 142–144 (2008).

44. Niskala, J. R. *et al.* Tunneling characteristics of Au-alkanedithiol-Au junctions formed via nanotransfer printing (nTP). *J. Am. Chem. Soc.* **134**, 12072–12082 (2012).

45. Kokil, A., Yang, K. & Kumar, J. Techniques for characterization of charge carrier mobility in organic semiconductors. *J. Polym. Sci. Part B Polym. Phys.* **50**, 1130-1144 (2012).

46. Kreno, L. E. *et al.* Metal-organic framework materials as chemical sensors. *Chem. Rev.* **112**, 1105–1125 (2012).

47. Sun, L., Park, S. S., Sheberla, D. & Dincă, M. Measuring and Reporting Electrical Conductivity in Metal-Organic Frameworks: Cd_2(TTFTB) as a Case Study. *J. Am. Chem. Soc.* **138**, 14772-14782 (2016).

48. Valdes, L. B. Resistivity Measurements on Germanium forTransistors. *Procedings of the I.R.E.* **29**, 420–427 (1954).

49. Uhlir, A. The Potentials of Infinite Systems of Sources and Numerical Solutions of Problems in Semiconductor Engineering. *Bell Syst. Tech. J.* **34**, 105–128 (1955).

50. Smits, F. M. Measurement of Sheet Resistivities with the Four-Point Probe. *Bell Syst. Tech. J.* **37**, 711–718 (1958).

51. Buehler, M. G. A hall four-point probe on thin plates. Theory and experiment. *Solid State Electron.* **10**, 801–812 (1967).

52. Buehler, M. G. & Thurber, W. R. Measurement of the resistivity of a thin square sample with a square four-probe array. *Solid State Electron.* **20**, 403–406 (1977).

53. Yamashita, M. Geometric Conrrection Factor for Resistivity of Semiconductors by the Square Four-Point Probe Method. *Japan J. Appl. Phys.* **25**, 563–567 (1986).

54. Murashima, S. & Ishibashi, F. Correction Devisors for the Four-Point Probe Resistivity Measurement on Cylindrical Semiconductors II. *Japan J. Appl. Phys.* **9**, 1340–1346 (1970).

55. Perloff, D. S. Four-Point Probe Correction Factors for Use in Measuring Large Diameter Doped Semiconductor Wafers. *J. Electrochem. Soc.* **123**, 1745-1750 (1976).

56. Perloff, D. S. Four-point sheet resistance correction factors for thin rectangular samples. *Solid State Electron.* **20**, 681-687 (1977).

57. Yamashita, M. & Agu, M. Geometrical correction factor for semiconductor resistivity measurements by Four-Point Probe Method. *Jpn. J. Appl. Phys.* **23**, 1499–1504 (1984).

58. Weller, R. A. An algorithm for computing linear four-point probe thickness correction factors. *Rev. Sci. Instrum.* **72**, 3580-3586 (2001).

59. Albers, J. An Alternative Approach to the Calculation of Four-Probe Resistances on Nonuniform Structures. *J. Electrochem. Soc.* **132**, 2453 (1985).

60. Albert, M. P. & Combs, J. F. Correction Factors for Radial Resistivity Gradient Evaluation of Semiconductor Slices. *IEEE Trans. Electron Devices* **11**, 148–151 (1964).

61. Rymaszewski, R. Relationship between the correction factor of the four-point probe value and the selection of potential and current electrodes. *J. Phys. E.* **2**, 170–174 (1969).

62. Braga, D. & Horowitz, G. High-Performance organic field-effect transistors. *Adv. Mater.* **21**, 1473–1486 (2009).

63. Bâldea, I., Xie, Z. & Frisbie, C. D. Uncovering a law of corresponding states for electron tunneling in molecular junctions. *Nanoscale* **7**, 10465–10471 (2015).

64. Banica, F. G. A Simple Hanging Mercury Drop Electrode. *J. Chem. Educ.* **77**, 98 (2000).

65. Otsubo, K., Haraguchi, T. & Kitagawa, H. Nanoscale crystalline architectures of Hofmann-type metal–organic frameworks. *Coord. Chem. Rev.* **346**, 123–138 (2017).

66. Gu, Z. G. & Zhang, J. Epitaxial growth and applications of oriented metal-organic framework thin films. *Coord. Chem. Rev.* **378**, 513–532 (2017).

67. Bétard, A. & Fischer, R. A. Metal-organic framework thin films: From fundamentals to applications. *Chem. Rev.* **112**, 1055-1083 (2012).

68. Zhuang, J. L., Terfort, A. & Wöll, C. Formation of oriented and patterned films of metal-organic frameworks by liquid phase epitaxy: A review. *Coord. Chem. Rev.* **307**, 391–424 (2016).

69. Horcajada, P. *et al.* Colloidal route for preparing optical thin films of nanoporous metal-organic frameworks. *Adv. Mater.* **21**, 1931-1935 (2009).

70. Demessence, A. *et al.* Elaboration and properties of hierarchically structured optical thin films of MIL-101(Cr). *Chem. Commun.* **101**, 7149–7151 (2009).

71. Demessence, A. *et al.* Adsorption properties in high optical quality nanoZIF-8 thin films with tunable thickness. *J. Mater. Chem.* **20**, 7676–7681 (2010).

72. Zacher, D., Baunemann, A., Hermes, S. & Fischer, R. A. Deposition of microcrystalline $[Cu_3(btc)_2]$ and $[Zn_2(bdc)_2(dabco)]$ at alumina and silica surfaces modified with patterned self assembled organic monolayers: Evidence of surface selective and oriented growth. *J. Mater. Chem.* **17**, 2785–2792 (2007).

73. Arnold, M. *et al.* Oriented crystallisation on supports and anisotropic mass transport of the metal-organic framework manganese formate. *Eur. J. Inorg. Chem.* **2007**, 60–64 (2007).

74. Burrows, A. D. *et al.* Compositional control of pore geometry in multivariate metal–organic frameworks: an experimental and computational study. *Dalt. Trans.* **45**, 4316–4326 (2015).

75. Dybtsev, D. N., Chun, H., Yoon, S. H., Kim, D. & Kim, K. Microporous Manganese Formate: A Simple Metal-Organic Porous Material with High Framework Stability and Highly Selective Gas Sorption Properties. *J. Am. Chem. Soc.* **126**, 32-33 (2004).

76. Huang, A., Bux, H., Steinbach, F. & Caro, J. Molecular-sieve membrane with hydrogen permselectivity: ZIF-22 in LTA topology prepared with 3-aminopropyltriethoxysilane as covalent linker. *Angew. Chemie - Int. Ed.* **49**, 4958–4961 (2010).

77. Huang, A., Dou, W. & Caro, J. Steam-stable zeolitic imidazolate framework ZIF-90 membrane with hydrogen selectivity through covalent functionalization. *J. Am. Chem. Soc.* **132**, 15562-15564 (2010).

78. Morris, W., Doonan, C. J., Furukawa, H., Banerjee, R. & Yaghi, O. M. Crystals as Molecules: Postsynthesis Covalent Functionalization of Zeolitic Imidazolate Frameworks. *J. Am. Chem. Soc.* **130**, 12626–12627 (2008).

79. Klinowski, J., Almeida Paz, F. A., Silva, P. & Rocha, J. Microwave-assisted synthesis of metal-organic frameworks. *Dalt. Trans.* **40**, 321–330 (2011).

80. Yoo, Y. & Jeong, H.-K. Rapid fabrication of metal organic framework thin films using microwave-induced thermal deposition. *Chem. Commun.* **0**, 2441 (2008).

81. Bux, H., Liang, F., Li, Y., Cravillon, J. & Wiebcke, M. Zeolitic Imidazolate Framework Molecular Sieving Membrane Titania Support. *J. Am. Chem. Soc.* **131**, 16000-16001 (2009).

82. Yaghi, O. M., Li, G. & Li, H. Crystal Growth of Extended Solids by Nonaqueous Gel Diffusion. *Chem. Mater.* **9**, 1074-1076 (1997).

83. Schoedel, A., Scherb, C. & Bein, T. Oriented nanoscale films of metal-organic frameworks by room-temperature gel-layer synthesis. *Angew. Chemie - Int. Ed.* **49**, 7225–7228 (2010).

84. MÜLLER, U. DE *et al.* Method For Electrochemical Production of A Crystalline Porous Material Organic Skeleton Material. (2007).

85. Ameloot, R. *et al.* Patterned growth of metal-organic framework coatings by electrochemical synthesis. *Chem. Mater.* **21**, 2580–2582 (2009).

86. Puurunen, R. L. Surface chemistry of atomic layer deposition: A case study for the trimethylaluminum/water process. *J. Appl. Phys.* **97**, 121301 (2005).

87. Zacher, D., Schmid, R., Wöll, C. & Fischer, R. A. Surface chemistry of metal-organic frameworks at the liquid-solid interface. *Angew. Chemie - Int. Ed.* **50**, 176–199 (2011).

88. Rubio-Giménez, V. *et al.* Bottom-Up Fabrication of Semiconductive Metal-Organic Framework Ultrathin Films. *Adv. Mater.* **30**, 1704291 (2018).

89. Bell, C. M., Arendt, M. F., Gomez, L., Schmehl, R. H. & Mallouk, T. E. Growth of Lamellar Hofmann Clathrate Films by Sequential Ligand Exchange Reactions: Assembling a Coordination Solid One Layer at a Time. *J. Am. Chem. Soc.* **116**, 8374-8375 (1994).

90. Shekhah, O. *et al.* Step-by-step route for the synthesis of metal-organic frameworks. *J. Am. Chem. Soc.* **129**, 15118-15119 (2007).

91. Gu, Z.-G. *et al.* Transparent films of metal-organic frameworks for optical applications. *Microporous Mesoporous Mater.* **211**, 82–87 (2015).

92. Arslan, H. K. *et al.* Intercalation in layered metal-organic frameworks: Reversible inclusion of an extended π-system. *J. Am. Chem. Soc.* **133**, 8158–8161 (2011).

93. Shekhah, O. Layer-by-layer method for the synthesis and growth of surface mounted metal-organic frameworks (SURMOFS). *Materials* **3**, 1302–1315 (2010).

94. Zhou, Z. *et al.* Antiferromagnetic copper(II) metal−organic framework based quartz crystal microbalance sensor for humidity. *Cryst. Growth Des.* **17**, 6719–6724 (2017).

95. Arslan, H. K. *et al.* High-throughput fabrication of uniform and homogenous MOF coatings. *Adv. Funct. Mater.* **21**, 4228-4231 (2011).

96. Won, H. *et al.* Carbon-Nanotube Optoacoustic Lens for. *Sci. Rep.* **2**, 989 (2013).

97. Vozar, S. *et al.* Automated spin-assisted layer-by-layer assembly of nanocomposites. *Rev. Sci. Instrum.* **80**, 023903 (2009).

98. Chernikova, V., Shekhah, O. & Eddaoudi, M. Advanced Fabrication Method for the Preparation of MOF Thin Films: Liquid-Phase Epitaxy Approach Meets Spin Coating Method. *ACS Appl. Mater. Interfaces* **8**, 20459–20464 (2016).

99. Makiura, R. & Kitagawa, H. Porous porphyrin nanoarchitectures on surfaces. *Eur. J. Inorg. Chem.* **2010**, 3715-3724 (2010).

Chapter Two From devices to chemoresistive gas sensors: charge transport in ultrathin film devices and environmental control of conductivity

1. Introduction

Among the family of conductive MOFs available,[1] two-dimensional (2D) MOFs are especially interesting.[2] Their high conductivity results from in-plane charge delocalization and extended π-conjugation along the sheets. Moreover, the possibility to be integrated in electronic devices by using soft bottom-up methods has recently been demonstrated.[3,4] In these systems, single metal atoms and benzene or triphenylene linkers with S, N, or O as donor groups bond into 2D honeycomb layers that stack together to form hexagonal channels (Figure 2-1).[5–10] The coordination of the metal center in the network is for most cases square planar, but also octahedral for HHTP (2,3,6,7,10,11-hexahydroxytriphenylene) and M=Co or Ni,[7] which have two axial water molecules. M-CAT [$M_3(HTTP)_2$] family was reported the first time by Yaghi et. al. on 2012.[7] Although, they reported the structure for Co and Ni-CAT, the structure of the Cu^{II} phase was still missing at the beginning of this thesis. Surprisingly, they reported an electrical conductivity of ≈ 0.2 $S \cdot cm^{-1}$ on a single crystal of Cu-CAT-1 [$Cu_3(HHTP)_2$]. Later, on 2015,[11] Campbell et. al. reported an electrical conductivity of 0.002 $S \cdot cm^{-1}$ on pressed powder for the same material, they also reported a value of 0.2 $S \cdot cm^{-1}$ for $Cu_3(HITP)_2$ (HITP=2,3,6,7,10,11hexaiminotriphenilene) and 2 $S \cdot cm^{-1}$ for $Ni_3(HITP)_2$, both materials share a similar structure. Additionally, they highlithed the marked electrical response of those three materials to different environments like ammonia and volatile organic compounds (VOC) (Figure 2-2).[11–15] Finally, in 2018,[16] Miner et. al. reported an electrical conductivity of ≈ $6 \cdot 10^{-3}$ $S \cdot cm^{-1}$ and ≈ $2 \cdot 10^{-3}$ $S \cdot cm^{-1}$ for $Ni_3(HHTP)_2$ and $Co_3(HHTP)_2$ respectively on pressed powder samples.

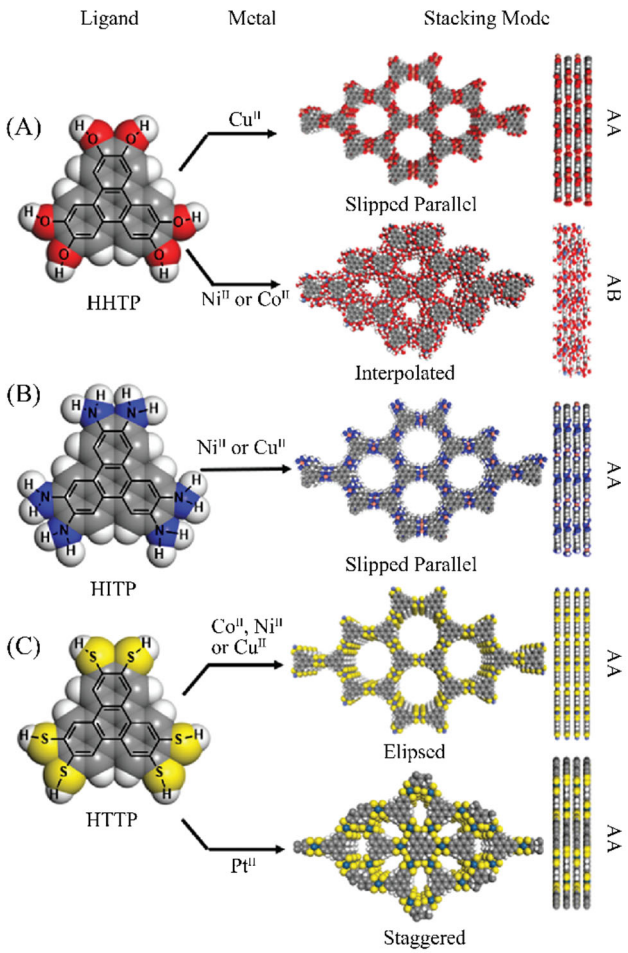

Figure 2-1 Three triphenylene based organic ligands with the heteroatom interchanged between (A) O,[7] (B) NH[9,12] and (C) S.[17–20] The heteroatom present on the triphenylene and the metal salt together dictate the formation of MOF and the stacking mode, which can vary from slipped parallel, eclipsed, staggered, and with or without the presence of an interpolated layer leading to either AA or AB pattern. Modified from ref. 2.

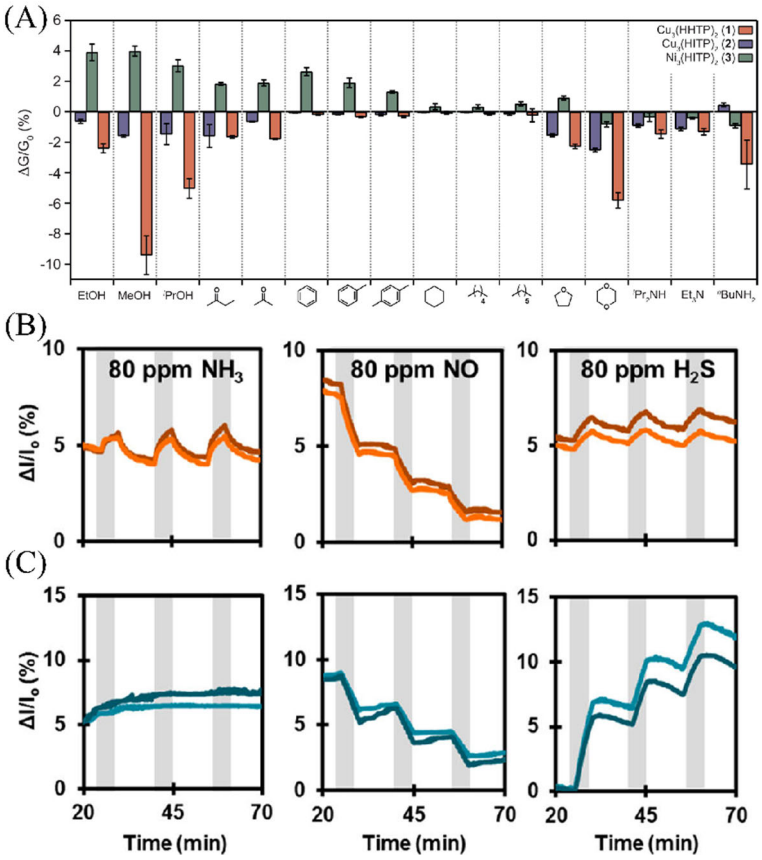

Figure 2-2 (A) Sensing responses of $Cu_3(HHTP)_2$, $Cu_3(HITP)_2$ and $Ni_3(HHTP)_2$ array to representative examples from different categories of VOCs, where $\Delta G/G_0$ is the relative response (change in conductance) upon a 30 s exposure to 200 ppm of the VOC vapor; each response is averaged from 12 measurements (4 exposures to 3 separate devices for each MOF); error bars show one standard deviation. Extracted from ref. 11. (B) Representative sensing traces (3 x 80 ppm) for $Cu_3(HHTP)_2$ and (C) representative traces (3 x 80 ppm) for $Ni_3(HTTP)_2$. Extracted from ref. 14.

These early works confirmed a direct dependence of the electrical response with host-guest interactions that can be also modified for different metal nodes. However, further information that would help to unveil the exact mechanism controlling this phenomenon was still missing.

To obtain more information about this phenomenon, we decided to re-investigate the conductivity of the M-CAT family (M = Co, Ni, Cu, Zn and Cd) (Figure 2-1A) paying special attention to the development of appropriate tools to measure their electrical behavior press-pellets, and on thin films under different atmospheres for environmental control of their chemoresistive response.

In the next sections, we will briefly describe the reaction conditions used to synthesize M-CAT-1 (M = Co, Ni, Cu, Zn and Cd) samples. Next, we will describe the designing of a home-build set-up designed for rapid measurement of the electrical conductivity of pressed pellets. Finally, we will use soft bottom-up methodologies for fabricating thin films of this family of MOFs and study their conductivity by using our own environmental controlled chamber under different environments to unveil the mechanism governing these conductivity changes.

2. M-CAT conductivity on pressed powder samples

To study pressed powder M-CAT samples, we developed a set-up to measure electrical conductivity using the four-point probe method (Figure 2-3).

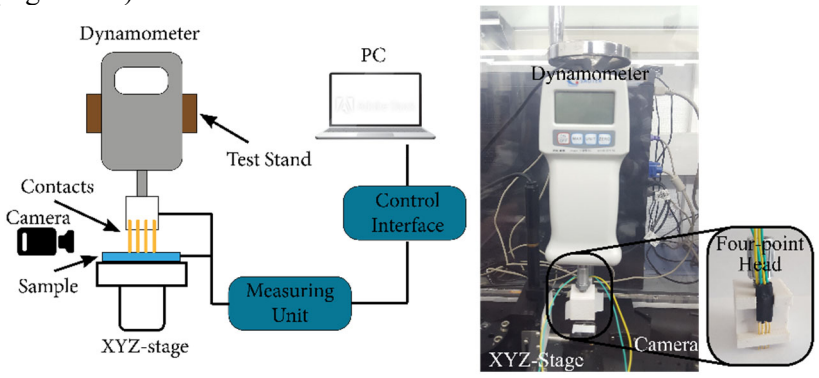

Figure 2-3 On the left, the diagram of our four-point probe set-up. On the right, Picture of the real set-up.

Compared to other commercial set-ups like Lucas Labs Pro4-440N, we thought on a tool that could adapt to the surface of the material and could be used on soft materials like MOF pressed powders. To achieve this aim, we implemented a dynamometer, to control the pressure exerted on the sample, attached to a homemade head (Figure 2-4) made of Acrylonitrile butadiene styrene (ABS) with four retractile gold probes to control the contact extended to the sample and to be able to

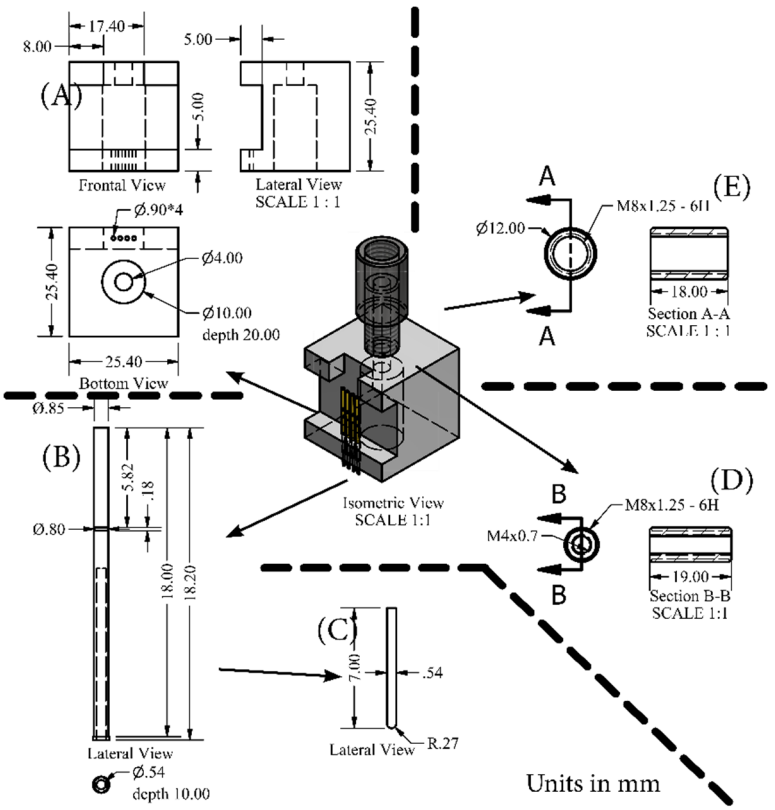

Figure 2-4 Sketch of the parts of our homemade tip holder. (A) Head to hold sleeves of the points, (B) sleeve of the gold points, (C) gold point, (D) screw to attach the head and (E) junction between Head and Dynamometer.

contact irregular surfaces. The sample is positioned using a Thorlabs

XYZ-stage, a test stand and a digital camera are used to control and monitor the approach to the sample. A voltmeter and ammeter are used to record the electrical signal.

To test the tool, first, we synthesized the M-CAT we wanted to study using solvothermal conditions. Briefly, we mixed HHTP in distilled water and an adequate metal salt and heat the mixture up at 85℃ for 12 hours. Then the resultant powder was filtered, dried and activated. To obtain the M-CAT pellet, the powder was compressed using a hydraulic press applying up to 6 KPa for 5 minutes.

Next, we collected several I-V curves on each one of the M-CAT (M = Cu, Ni, Zn, Cd, and Co) pellets. Figure 2-5 shows the average I-V for each sample. The conductivity is calculated from Eq. 1-17 as:

$$\sigma = \frac{\ln(2)}{\pi * s} * \frac{I}{V} = \frac{2 * 10^{-1}}{s} * \frac{I}{V}$$

where the diameter (D), sample thickness (t) sample and distance between probes (s) were measured by optical approach and a caliper. The diameter and thickness of the samples were 10 to 13 mm and 150 to 300 μm, respectively. The distance between probes was fixed at 1.2 mm for all samples. Intensity values was obtained at a bias of 5 volts. As can be seen, there are more than 5 orders of magnitude difference in intensity as a function of the metal. Co is the least conductive and Cu is the most conductive (Figure 2-5).

Conductivity values are shown in Table 2-1 and in general are not comparable with the ones found in the bibliography.[2,14,16] Although the values follow the same trend with Cu being the most conductive of them. Those difference could be related to the way which the sample

were synthesized, activated, ground, compressed or even the method that was used to do the electrical measurements.

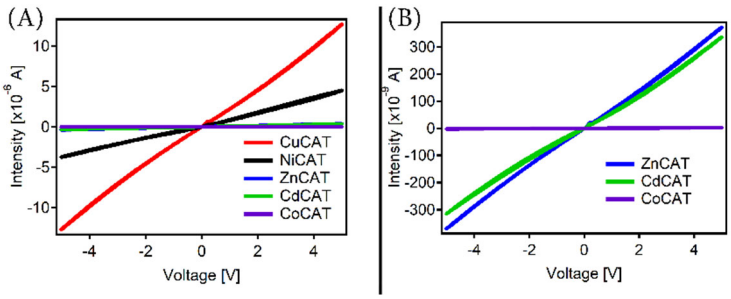

Figure 2-5 $I-V$ curves of the M-CAT family (A) the total comparation of five metals and (B) a zoom showing the comparation between Zn, Cd, and Co.

Table 2-1 Conductivity (σ) values for each sample of the M-CAT family.

Sample	Conductivity (σ) [S/cm^{-1}]	σ/σ_{Co}	Conductivity Reported (σ) [S/cm^{-1}]	REF.
$Cu_3(HHTP)_2$	$1.9*10^{-5}$	$1.0*10^{4}$	$7.6*10^{-3}$	14
$Ni_3(HHTP)_2$	$6.8*10^{-6}$	$3.7*10^{3}$	$6.0*10^{-3}$	16
$Zn_3(HHTP)_2$	$5.7*10^{-7}$	$3.1*10^{2}$	n/a	n/a
$Cd_3(HHTP)_2$	$4.7*10^{-7}$	$2.6*10^{2}$	n/a	n/a
$Co_3(HHTP)_2$	$1.8*10^{-9}$	1.0	$2.0*10^{-3}$	16

Next, to rule out that the observed differences were coming simply from experimental errors I tested different conditions. What I did was: i) **to measure the sample on two different directions** to monitor the influence of the sample mounting on the conductivity, and ii) **to measure the sample, to grind it again, to compress the powder once more, and then to measure it again**, to monitor the influence of

sample preparation on the conductivity and rule out structural transformations.

As a result of those experiments, we obtained:

i) Same sample measured on two orientations

For this experiment, I measured the pellet on two different orientations, the original position and after turning it 90° with respect to the original position. This experiment was carried out on seven samples. The variation observed of the M-CAT family is probably reflecting the differences in the packing of the crystallites inside the pellet or changes in thickness. Figure 2-6 shows the measured average I-V for the pellets that showed the biggest and smallest change in conductivity at 0° and 90°. A maximun 47% variatation in σ was observed in the case of Ni-CAT curves at 0º and 90º.

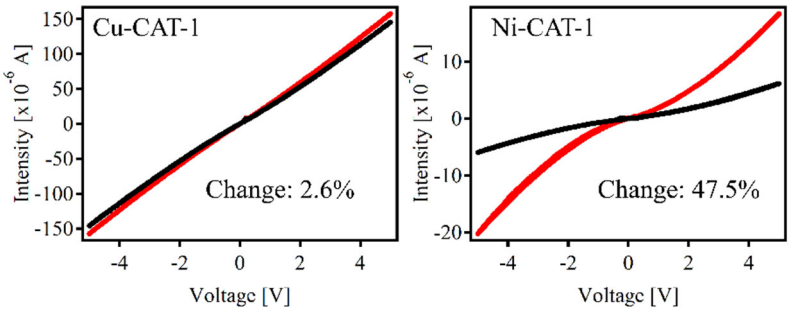

Figure 2-6 measured average I-V for the pellets that showed the biggest and smallest change in conductivity at 0° and 90°. Red line represents I-V curve of the sample on the initial orientation and Black line represent I-V curve measured on the sample but after turning it 90° respect to the initial position.

ii) Conductivity on re-ground samples

To carry on the second experiment, I ground, pressed and measured the sample for the first time, then I repeated the process once again. Figure

2-7 shows the worst result after measuring 16 I-Vs where the changes observed were up to 81.33%. These conductivity changes can be attributed once again to differences on grain orientation or even to the H_2O release after grinding the sample for a second time. As we will describe later, there is a drastic effect of the atmosphere over the resistivity of this family of porous solids.

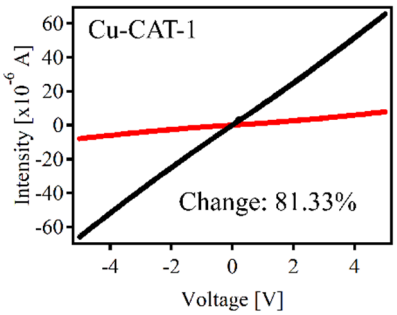

Figure 2-7 I-V curves of a sample measured for the first time, then, ground, compressed and measured again. Red line represents the first time the sample was measured, and black line represent the second time the sample was measured.

These experiments have shown that changes on conductivity below 80% should be expected in our method. However, 5 orders of magnitude (Table 2-1) cannot be the results of the observed experimental errors, but something related to the changes on the true nature of the sample.

Although, the measured conductivity values do not match with those reported by others in the literature, they follow the same trend Cu >> Ni and Co. It is important to highlight that to fathom out the reason of this changes is not a simple task. For example, the use of different metals and HHTP does not only imply the obvious change in electronic structure but also changes on the crystallographic structure. This can be observed comparing the structure of Co-CAT and Cu-CAT-1.

Co-CAT is formed by extended $Co_3(HHTP)_2(H_2O)_6$ layers and $Co_3(HHTP)_2(H_2O)_{12}$ discrete complexes between the layers.[4] Whereas, Cu-CAT-1 structure is formed only by slipped-parallel (AA) staking of hexagonal layers.[4]

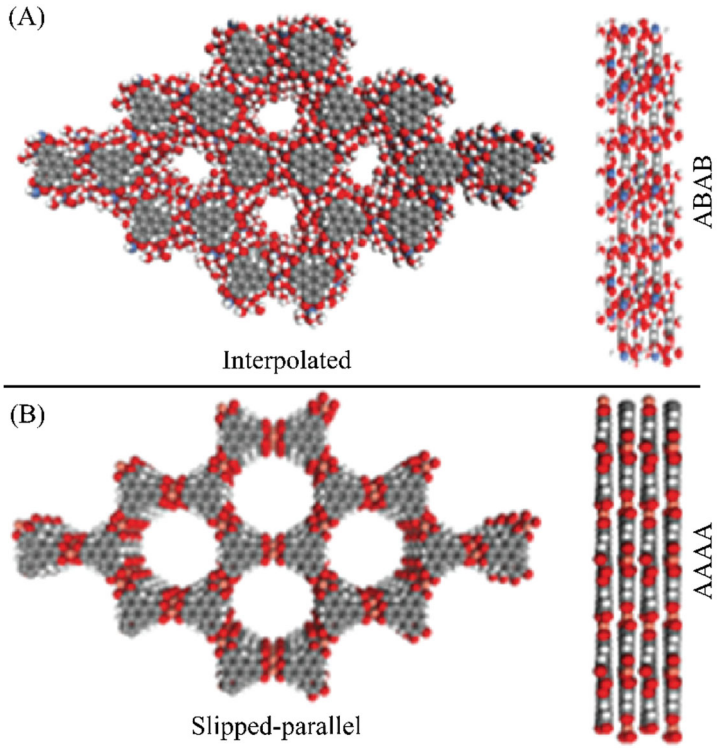

Figure 2-8 Crystal structure for (A) Co-CAT and (B) Cu-CAT-1, both extracted and adpted from ref. 2.

All those changes should reflect on the electrical conductivity of the resultant material. Moreover, if we conserve the metal and change the hydroxyls of the ligand to amino groups for example, the conductivity of the series is reversed to Co to Ni>>Cu[11]. Summing, up the observed conductivity trends cannot be rationalized on the basis of simple chemical principles.

At this point, we have confirmed Cu-CAT-1 as the most conductive member of the M-CAT-1 family, in agreement with the results of Dincă & Miner[16]. Next, we will review briefly our approach to deposit and integrate this material into an interdigitated device.

3. Bottom-up fabrication of semiconductive MOF ultrathin films

With the aim of integrating Cu-CAT-1 into FET-type device, we studied the possibility to deposit it as a film using the LbL and LB-LbL techniques[4] (see chapter one: section 2.4.3.). Althoug we succeded obataining films with both methods, the best results were obtained pre-functionalizing the substrate with an appropriated SAM and using the LB-LbL technique. To deposite Cu-CAT-1 as a homogeneous thin film on different planar substrates. In this case, HHTP solution was dispersed on a subfase (usually water), as it is insoluble in the subphase, the substance formed floating layers on top, which is then compressed at the desired pressure to form continuous film and then transferred to a functionalized substrate by bringing it into contact with the floating film. For more information: address the reader to the PhD thesis of V. Rubio-Giménez.[21]

Next, to study the electrical behavior of the film. It was deposited on four pairs of interdigitated Au Electrodes pre-patterned (with S of 2.5µm and L of 500µm) on top of Si/SiO_2 substrate (SiO_2 230 nm thick and highly doped n-type Si acting as dielectric and gate respectively, to eventually apply a bottom-gate voltage) (Figure 2-9).

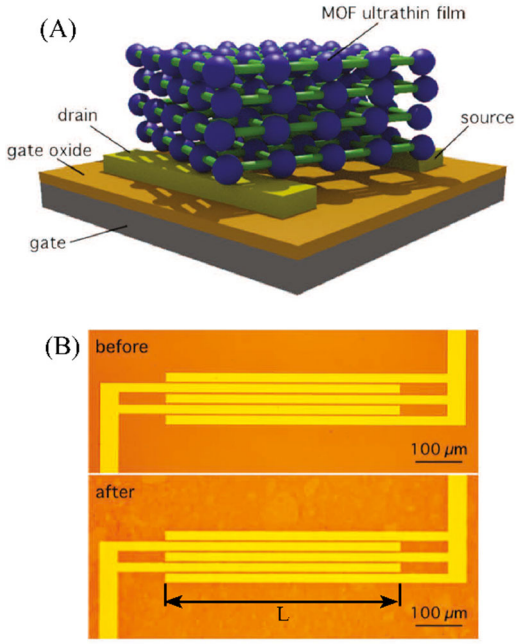

Figure 2-9 (A) Schematic of a Cu-CAT-1 bottom-gate bottom-contact MOF-based device. (B) Optical microscope picture of a real device with on a pair of interdigitated pre-patterned Au electrodes with a L of 500μm and S of 2.5μm before/after LB transfer of a 10 nm thick film. Extracted from ref. 4.

First, we studied the resistance as a function of the number of transfers with samples prepared with the LbL and LbL-LB methods (Figure 2-10). Compared to LbL-LB films, samples fabricated by LbL reaction show a higher average resistance values and a higher dispersion in measurement statistics, as well as a less clear exponential tendency of resistance decay with film thickness. This is probably the consequence of poorer film/electrode interfaces and it clearly denotes a lower homogeneity and reproducibility of the films.

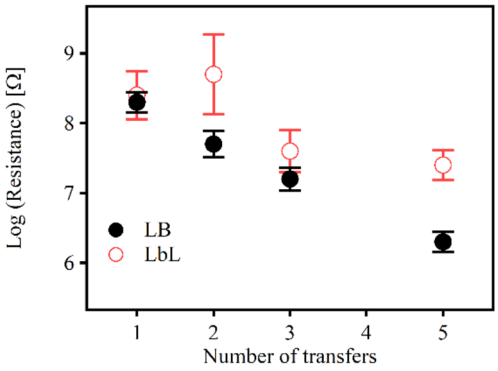

Figure 2-10 Comparison of the logarithm of device resistance vs a number of transfers for devices fabricated via the LB technique (black solid circles) and via the LbL method (red empty circles). Solid and empty circles correspond to the average of logarithmic resistance for at least four different devices fabricated respectively using LB and LbL techniques. Devices have a channel length of 2.5 µm and they were measured in an air atmosphere. Error bars are calculated as the standard deviation of these values. Extracted from ref. 4.

Next, we studied the dependence of the LB-LbL film conductivity with the temperature. Figure 2-11 shows the dependence of the electrical conductivity to the temperature on a 10 transfers Cu-CAT-1 film. Tranport results suggest that two transport mechanisms are operative. For $T > 240\ K$, transport is dominated by thermal activation and, for $T < 240\ K$, is dominated by a variable range hopping mechanism.

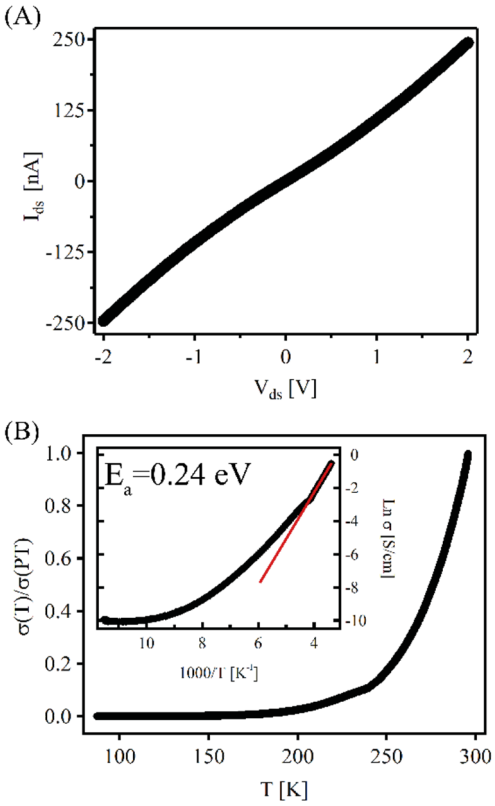

Figure 2-11 (A) Room temperature I–V curve for the device (2.5 µm channel length). The measurement was performed in a vacuum. (B) Electrical conductivity (σ) of the device as a function of temperature measured at a bias voltage of V_{ds} = 1 V and normalized by the electrical conductivity measured at room temperature (σ(RT)). The inset shows the plot of Ln(σ(T)/σ(RT)) versus 1/T. From the linear fit at elevated temperature (red line), we estimate activation energy of 0.24 eV. Modified Extracted from ref. 4.

As a complement for this work, we carried out some experiments of source-drain current modulation with bottom gate voltage (Figure 2-12A and B). We believe that the small device modulation we observe should be mainly attributed to a bad contact between the MOF thin film and SiO_2 layer created by the SAM. This was supported by the fact that

when we performed some preliminary tests using the "cut and stick" process to fabricate a ion gel base top gate as reported by Lee et al.[22] (Figure 2-12C) the modulation improved. The top gate was fabricated

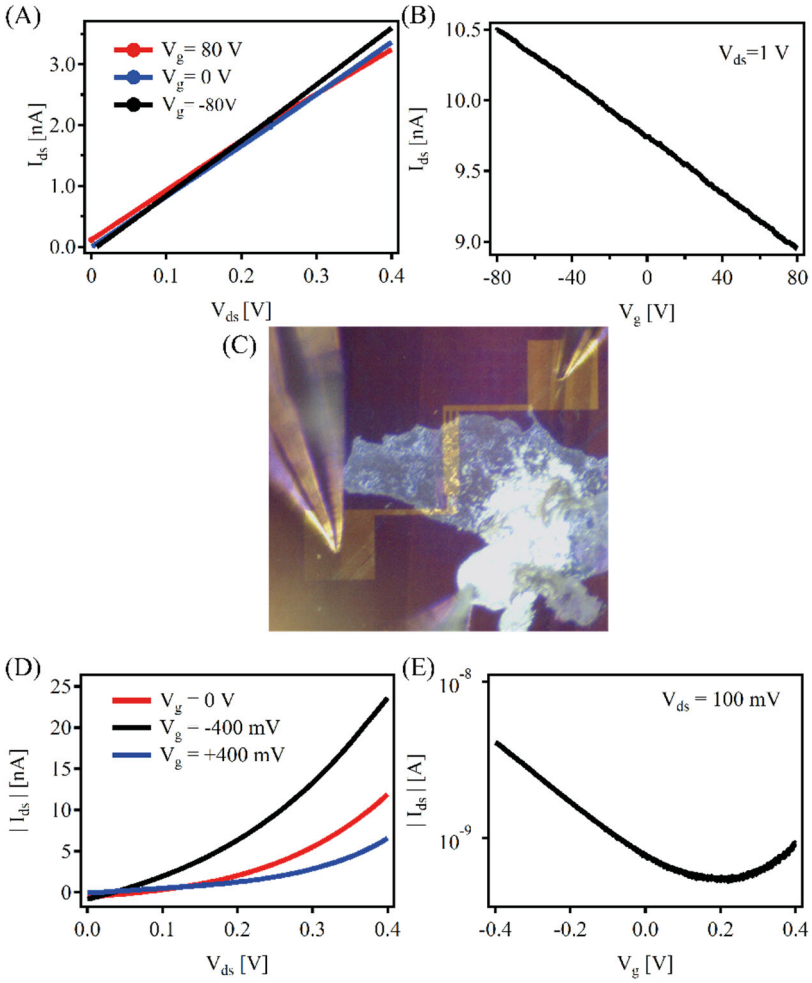

Figure 2-12 Electrical response of a device as a function of the applied top gate or bottom gate voltage (V_g). Measurements were performed in air atmosphere on a device fabricated via the LB technique with a Cu-CAT-1 film thickness of 10 nm and a channel length of 5 µm. (A) Drain-source current (I_{ds}-V_{ds}) curves for three different top gate voltages of 400 mV, 0 V and -400 mV. (B) I_{ds} modulation with top V_g. (C) Picture of top gate (D) I_{ds}-V_{ds} curves for three different bottom gate voltages of 80 V, 0 V and -80 V. (E) I_{ds} modulation with bottom V_g.

using an ion gel based on a copolymer [poly (vinylidene fluoride-co-hexafluoropropylene), P(VDFHFP)] and an ionic liquid (1-ethyl-3-methylimidazolium bis(trifluoromethylsulfonyl)amide, [EMI] [TFSA]).[22] The observed better modulation, as shown in Figure 2-12D and E opens the door to integration and optimization of our films into FET-type devices.

4. Measuring electrical conductivity in different environments

As indicated above, Cu-CAT-1 films change their conductivity according to the environment conditions to which they are exposed. As a result, Cu-CAT-1 films had been used before as chemosensors. However, the mechanism controlling these changes remained unknown. We saw here, the opportunity to use our films to study the response of Cu-CAT-1 under different environments and to understand mechanism controlling that response. For this propose, we developed a original set-up to enable direct control of the environment inside the chamber for running dynamic measurements of electrical conductivity under variable atmospheres (Figure 2-13).

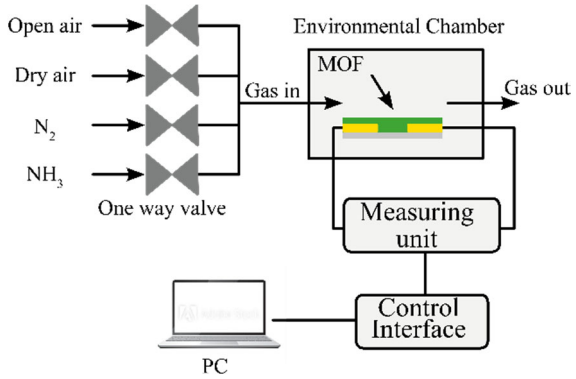

Figure 2-13 Diagram of the set-up for electrical measurements under different environments used in this thesis.

According to the sketch presented in Figure 2-13, we employed a prefabricated sealed chamber of 160x50x130 mm^3 (Figure 2-14A and B) drilled on three of the faces and included fast junctions for the wires used to connect the sample to the measurement instruments and the gas input and output (Figure 2-14A and C). Additionally, we developed a

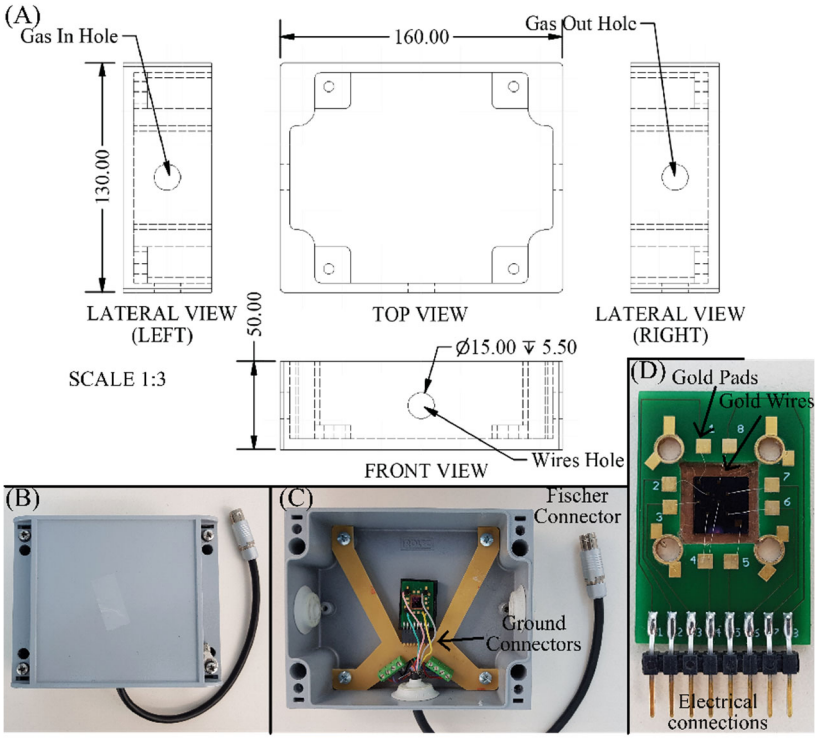

Figure 2-14 Sketch and pictures of the chamber and its components. (A) Sketch of the chamber with its different view pointed of the holes for the gas input/output and the electrical connections. (B) Prefabricated sealed chamber where we can observe the Fischer connector, (C) inside of the chamber showing the gas input/output and the electrical connections, (D) Zoom of the PCB holder we used to connect the samples.

holder and a bed to connect the sample to the chamber (Figure 2-14D). The box was connected to the exterior using a Fischer connector. The sample was mounted on a PCB holder patterned with gold pads. These

pads were connected to the interdigitated contacts using gold wire. The PCB was connected to the box by means of an 8-pin connector. As gas inlet, I used a pneumatic pipe of 6 mm of diameter with a one-way pneumatic valve of the same diameter to open and close the input/output of gas. A bubbler was connected to the gas outlet to observe the gas flow and prevent the contamination of the experiment.

To deposit the films we followed the same deposition protocol described in the previous section. Next, the electrode pads were wedge bonded to the PCB support and inserted into the chamber. Then it was closed and flushed with the test gas (200-1000 sccm) while recording the electrical response as a function of time ($\sigma\ vs\ t$). During the first minutes the output remained open to displace the previous gas, then the output was closed. Once a stable current signal was obtained, I-V curves were measured to confirm that ohmic contacts were formed under all conditions before the environment was changed (Figure 2-15A). Later, this process was repeated to obtain the electrical response under different atmospheres. Using this procedure curves like the one displayed in Figure 2-15B could be obtained. Individual electrical conductivity values (solid dots on Figure 2-15B and Figure 2-16) correspond to the plateau mean value of the σ in this conditions. The average (standard deviation) conductivity for each atmospheric condition (right part of Figure 2-16) was computed as the average (standard deviation) of all values. During the experiments we measured the environmental changes upon exposure to nitrogen (Carburos Metálicos, X50S), synthetic air (Praxair 3X), ammonia (Praxair, nitrogen mixture, 500 ppm vol.) and ambient conditions (atmospheric air, room temperature, approximately 65% relative humidity) on at least 4 devices on 2 different samples. A Yokogawa GS200 was used

to apply 0.1 V bias voltage and a Keithley 6517B electrometer to measure the current. Both instruments were controlled using custom LabVIEW programs. Sample temperature was between 23ºC to 27ºC thorough all experiments.

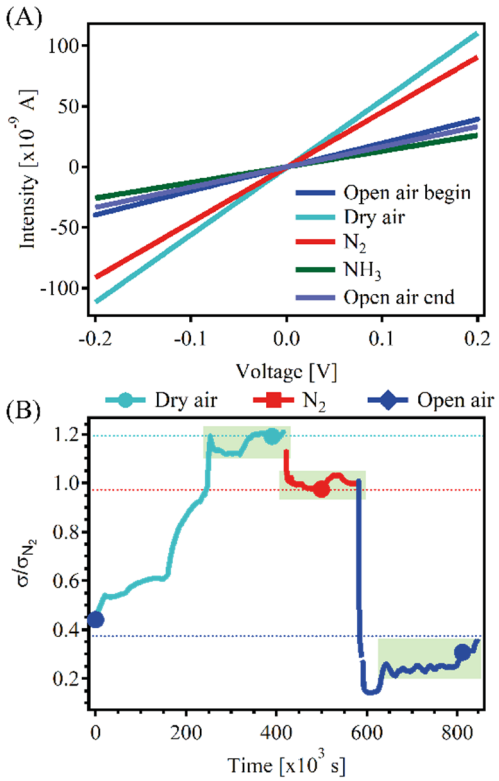

Figure 2-15 (A) I-V curves measured under different atmospheres inside the chamber. (B) Electrical Conductivity (σ) vs time corresponding to different atmosphres for the same sample with a ~30 nm Cu-CAT-1 films device. Green area corresponds to the plateau. Solid dots correspond to the plateau mean values of the σ vs t curves. Grey lines are a guide for the eye. Results have been normalized as σ/σ_{N_2} using the nitrogen average conductivity.

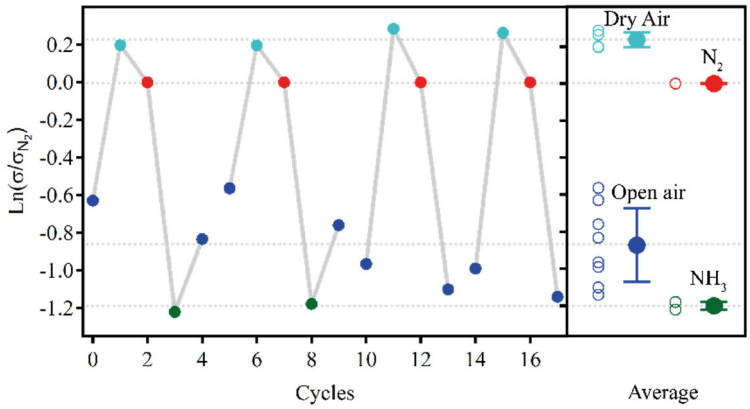

Figure 2-16 Left: Summary of the results on 4 different ~30 nm Cu-CAT-1 film devices subject to different gas test. Dots on the left panel correspond to the plateau mean values obtained from the σ vs t curves. Result have been normalized as $Ln(\sigma/\sigma_{N_2})$ using the average conductivity under nitrogen. Right: normalized average conductivities represented as $Ln(\sigma/\sigma_{N_2})$ measured under different ambient conditions. Grey lines are a guide for the eye.

Our results confirm clear changes on the electrical conductivity under different environments. It is worth mentioning that the response of the system was very slow (i.e. $154 \cdot 10^3$ s is equivalent to day and a half) compared to the results reported by Campbell et. al.[11] where a quite stable signal was obtained after 100 seconds. This could be the result of the very large ($1.2 \cdot 10^{-3} m^3$) volume of gas that has to be displaced by the input gas. Additionally, we observed a marked temperature dependence on the results (Figure 2-17). Nevertheless, in spite of these shortcomings, we observed two clear groups of points data. One that correspond to the conditions generating an inert atmosphere like dry air and N_2, and another set corresponding to guess molecules more prove to chemical interaction with the MOF like open air and NH_3. We believe that the difference between dry and open air are motivated by the presence water in the latter.

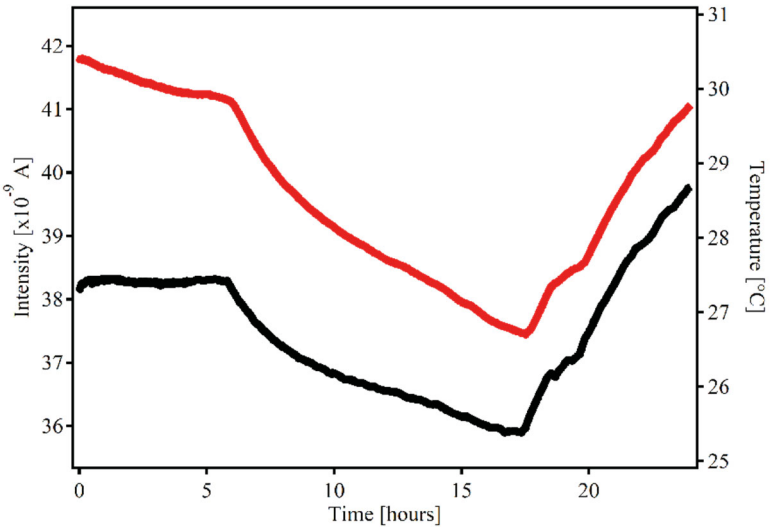

Figure 2-17 Electrical conductivity (σ) vs time vs temperature curve on ~30 nm Cu-CAT-1 films device. Red line corresponds to a measurement of σ vs time and Black line corresponds to a measurement of temperature vs time.

In order to reduce the time response, to make the process faster, to be able to measure in the absence of gas and to control the temperature, it was necessary to develop a new chamber with improved specifications. Following this premise, we updated the set-up replacing the box chamber (Figure 2-18A) by an ISO-KF Reducer Cross KF50 to KF40 (Figure 2-18B) in order to reduce the volume from $1.2 \cdot 10^{-3}$ m^3 to $3.8 \cdot 10^{-4}$ m^3. To pass the electrical connections into the chamber, we employed a 15-pin D-sub feedthrough mounted on a KF50 Flange (Figure 2-18C) and for gas inlet/outlet connections, a custom made KF50 Flange with two Swagelok line valves was employed as it is shown on Figure 2-18D. The remaining KF40 connections are for future upgrades and were blanked in this experiment. To interface our sample while keeping compatibility with our previous design, we designed and printed a board including D-sub female and PCB

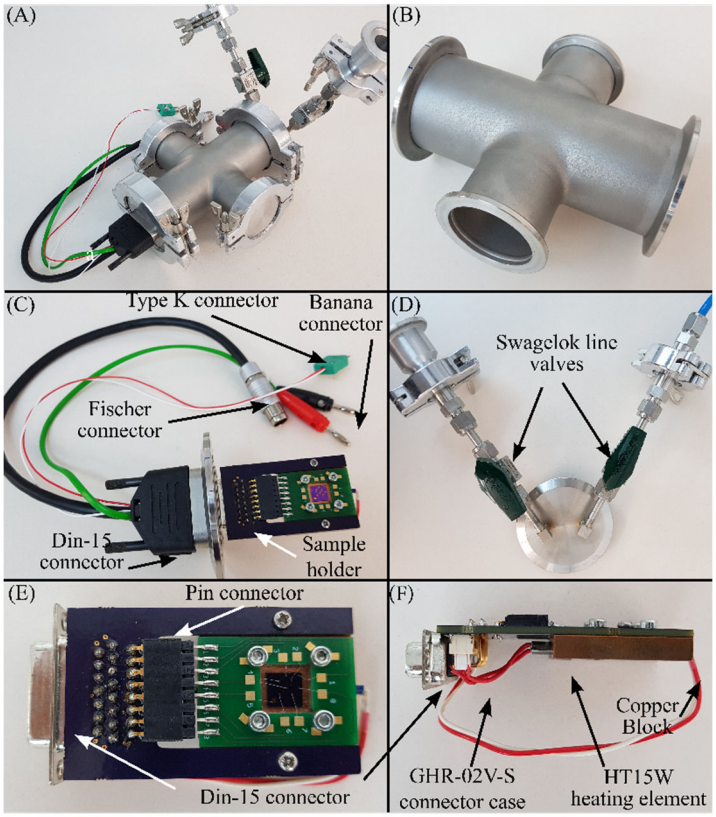

Figure 2-18 Picture of the Real set-up; (A) general view of the set-up; (B) general view of ISO-KF Reducer Cross KF50 to KF40; (C) view of D-sub feedthrough of 15 pins on KF50 Flange with a D-sub female connector of 15 pins and fisher connector of 11 pins together to type K connector to the temperature sensor and two banana plug for HT15W heating element; (D) custom made KF50 Flange with two Swagelok line valves; (E) top view of sample holder with electrical connections; (F) lateral view of sample holder where it can be observed the Cu block, the HT15W heating element rod, and its GHR-02-S connector case.

connectors (Figure 2-18E, F and Figure 2-19). Below it, a copper block was fixed. An a Thorlabs HT15W heating element and a Pt1000 temperature sensor were connected to control the temperature (Figure 2-20).

The sample holder was connected to the KF50 Din connector from the inside and to the electrometer and the temperature controller from the outside using the Din-15, Fischer, male type K and banana connectors.

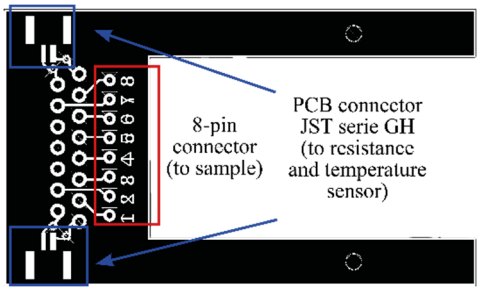

Figure 2-19 PCB sketch for Sample Holder

The Homemade temperature controller (Figure 2-20A) is composed by a ± 24 V_{DC} source, a voltage divider to divide $\pm 24 V_{DC}$ to obtain ± 12 V_{DC} for the supply of the heat sink fan, and a commercially TEC-1123 main board, that has two channels to apply up to ±16 A and ±30 V_{DC} per channel. With this controller, it is possible to control the temperature slope and the time required to stabilize for each channel independently. Each channel can be connected to a resistance, a heating element or a Peltier to control of temperature (Figure 2-20B). For this experiment, I have employed a heating rod that can heat up the sample up to 450℃.

Previous experiments have shown that σ was dependent on the temperature changes in the lab. For that reason, since this point on I carried out all the measurements setting the temperature to 30℃ with an error of ± 0.5℃ using the temperature controller.

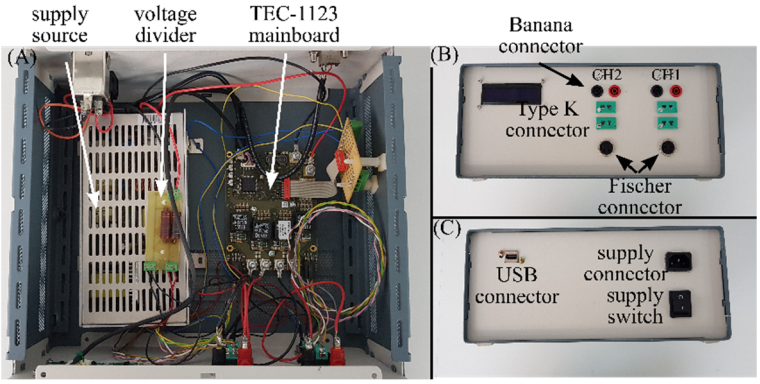

Figure 2-20 (A) internal view of the temperature controller with its internal components: ± 24 V_{DC} source, voltage divider, and temperature controller TEC1123 Mainboard; (B) front view with a LCD and connections for two channels, banana connectors to control the resistance or Peltier, Type K connections to monitor temperature using a PT1000 or NTC sensors, and Fischer connection to control the fans (not shown). (C) back view with (i) a supply connection, a supply switch and USB connection to communicate with the PC and LabVIEW.

Following the same procedure used before, we inserted the sample into the chamber. It was then sealed and flushed with the test gas (200-1000 sccm) or dynamically pumped to $1 \cdot 10^{-6}$ mbar while recording the electrical response as a function of time (σ vs t). Once a stable current signal was obtained (Figure 2-21A), I-V curves were measured to confirm that ohmic contacts were formed under all conditions before the environment was changed (Figure 2-21B). The new gas was injected into the chamber until the working pressure was reached (1 bar). I waited until the measured current was stable and repeated the same process again. Using this procedure curves like the one displayed in Figure 2-22 could be obtained. Individual conductivity values (solid dots on Figure 2-22 and Figure 2-23) correspond to the plateau mean value of the σ vs t curves. The average (standard deviation) conductivity for each atmospheric condition (right

part of Figure 2-23) was computed as the average (standard deviation) of all the plateau mean values. During the experiments, we measured

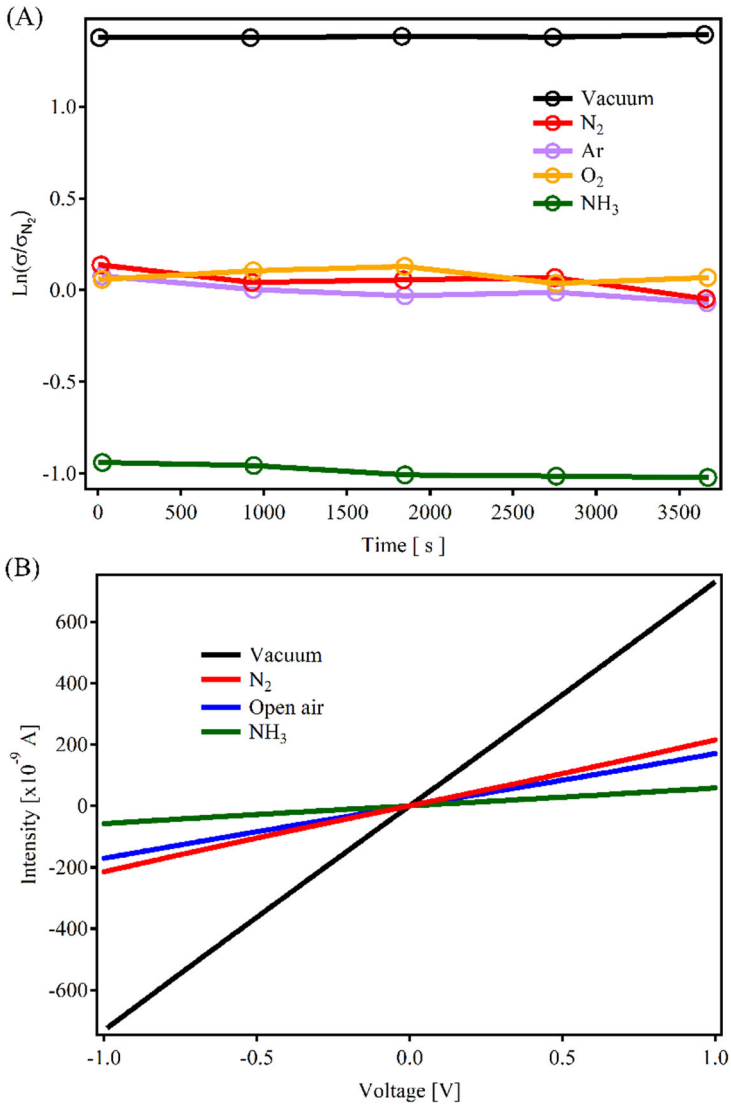

Figure 2-21 (A) Electrical response as a function of time measurements on a ~30 nm Cu-CAT-1 film device exposed to different atmospheres. (B) I-V curves measured under different atmospheres for a ~30 nm Cu-CAT-1 film device. Extracted from ref. 23.

the environmental changes upon exposure to oxygen (Praxair, 4X), argon (Praxair, 3X) and the same gases used on the previous experiment on at least 12 devices on 3 different samples. A Yokogawa GS200 was used to apply 0.1 V bias voltage and a Keithley 6517B electrometer to measure the current. Both instruments were controlled using custom LabVIEW programs.

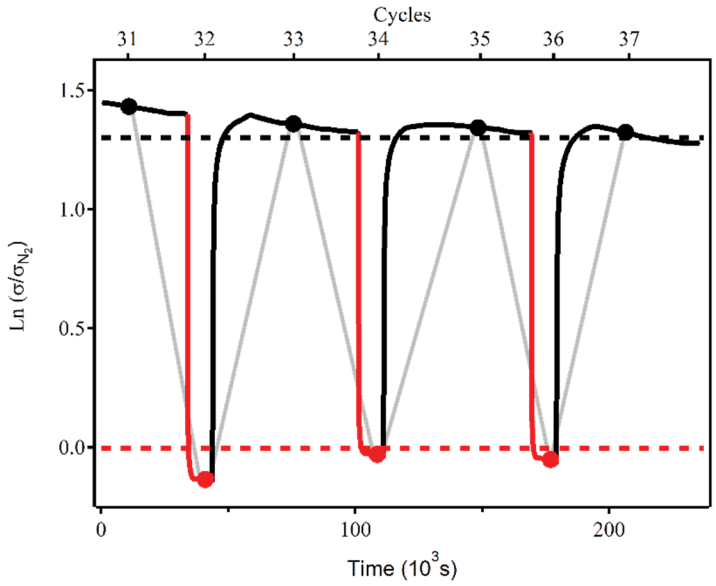

Figure 2-22 Conductivity (σ) vs time curve corresponding to three consecutive vacuum-nitrogen cycles measurements on a ~30 nm Cu-CAT-1 film device. Solid dots correspond to the plateau mean values of the σ vs t curves. Grey lines are a guide for the eye. Results have been normalized as $ln(\sigma/\sigma_{N_2})$ using the nitrogen average conductivity. Extracted from ref. 23.

In Figure 2-23, we have seen that inert gases with poor coordination ability share similar conductivity values, whereas exposure to room conditions results in a broader electrical response. The variation observed when the sample is exposed to vacuum conditions may indicate that adsorbates from the previous cycle have not been fully

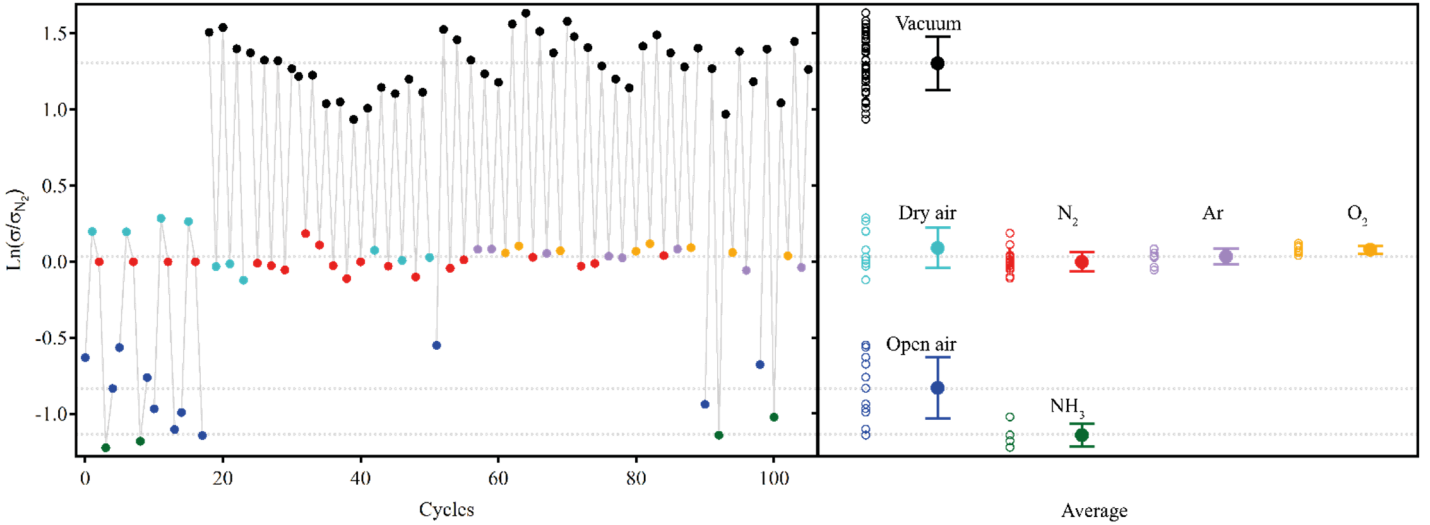

Figure 2-23 Left: Summary of the results obtained on 12 different ~30 nm Cu-CAT-1 film devices subject to different gas test cycles. Dots on the left panel correspond to the plateau mean values obtained from the σ vs t curves. Results have been normalized as Ln (σ/σ_{N_2}) using the average conductivity under nitrogen. Right: normalized average conductivities represented as Ln (σ/σ_{N_2}) measured under different ambient conditions. Grey lines are a guide for the eye. Extracted from ref. 23.

removed. However, after additional non–interacting gas/vacuum cycles, the sample recovers its initial conductivity, confirming that the film is not degraded during the process.

Our experimental data suggest a strong influence of the environment over the film resistance. Variation is quite homogeneous for gases without donor atoms, whereas exposure to room conditions results in very unstable electrical response. This highlights the necessity of controlling the atmosphere in which the electrical conductivity of MOFs is measured to ensure a meaningful comparison between different materials.

As a first step to rationalize to rationalize the experimental data, we used the Co-CAT structure reported by Dincă et al.[7] together with powder diffraction of Cu-CAT-1 to obtain its estimated structure (Figure 2-24), as it had not been reported before. The cell parameters

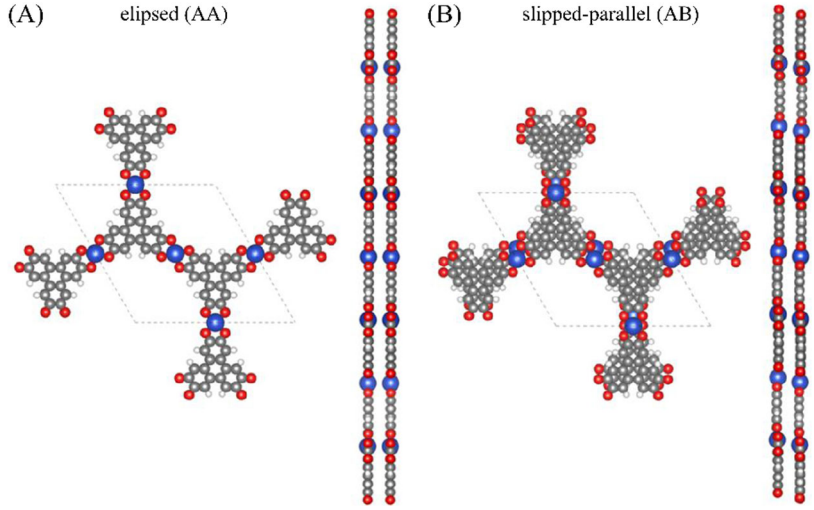

Figure 2-24 Top and side view of crystal structure of Cu-CAT-1 showing two possible packing modes: (A) eclipsed (AA) and (B) slipped-parallel (AB) orientations. Modified from ref. 4.

for this model were a = b = 21.3544 Å, and c = 6.7248 Å. However, the crystal structures resulting from the refinement are impossible to differentiate between two possible stacking arrangements: eclipsed (AA), and slipped-parallel (AB) orientations (Figure 2-24). Our DFT calculations indicate that the energy of the slipped-parallel arrangement is 0.19 eV lower than that of the eclipsed structure, which is agreement with previous theoretical calculations.[9, 17]

Using the Cu-CAT-1 structure, we related the experimental conductivity values with the calculated electronic structure of Cu-CAT-1 under vacuum and in presence of different guest by using dispersion-corrected density functional theory (DFT-D3) and the above Cu-CAT-1 structural model.[4] In the absence of guest interactions (vacuum), Cu-CAT-1 is a semiconductor with a band gap of 0.33 eV (Figure 2-25A). Then, to investigate the effect of host–guest interactions, the structure of Cu-CAT-1 was optimized in presence of N_2, H_2O, and NH_3. The relative humidity at room conditions in our laboratory is 65%, so we assumed that modeling environmental conditions as H_2O was a fair assumption to simplify calculations. As shown in Figure 2-25B, the interaction of N_2 molecules with Cu^{II} centers is extremely weak with Cu-N distances close to 4.3 Å contrary to H_2O and NH_3 molecules, that suggest a stronger interaction with open metal sites (Figure 2-25C and D). The changes to the internal structure of the layer caused by direct interaction of the guest with the open metal sites might have a stronger impact over the electronic structure, for band gaps of 0.40 eV and 0.42 eV after H_2O and NH_3 infiltration due to these two are coordinated in the axial position of the metal.

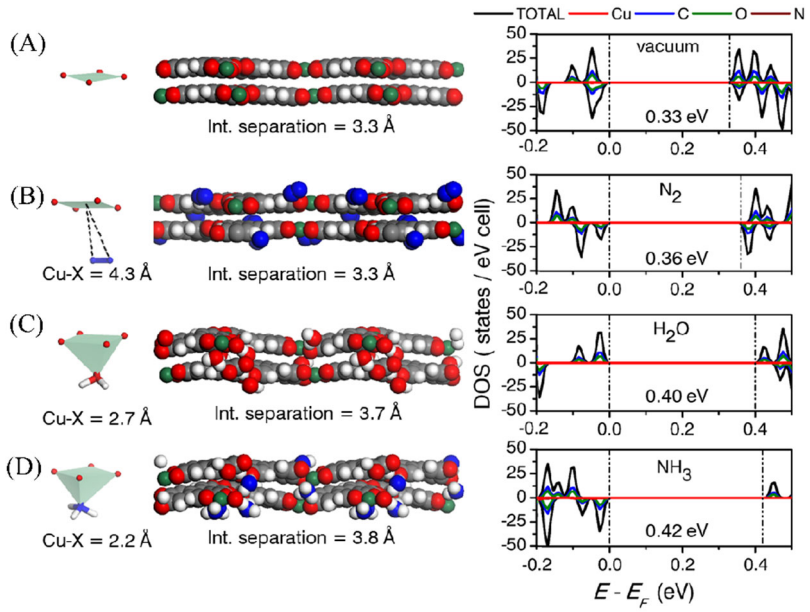

Figure 2-25 Left: Representation of the coordination sphere of CuII centers and DFT-calculated structure. Right: Electronic density of states (DOS) of Cu-CAT-1 in (A) vacuum and in presence of (B) N_2, (C) H_2O, and (D) NH_3. DOS were calculated by using the screened hybrid potential HSE06. Extraced from ref. 23.

Previously, we confirmed that the experimental conductivity of Cu-CAT-1 films with variable thickness (10–50 nm) displays a linear dependence at the high-temperature regime, consistent with a thermally activated mechanism for charge transport.[4] Provided this mechanism is respected, this shall enable a direct comparison of conductivity values with the changes on the electronic structure of the solid upon guest loading ($\ln \sigma \propto E_g$).[1] Figure 2-26 shows that the experimental variations in the conductivity of Cu-CAT-1 under the different atmosphere environments studied follow a linear correlation with the calculated band gap values. This validates our experimental model.

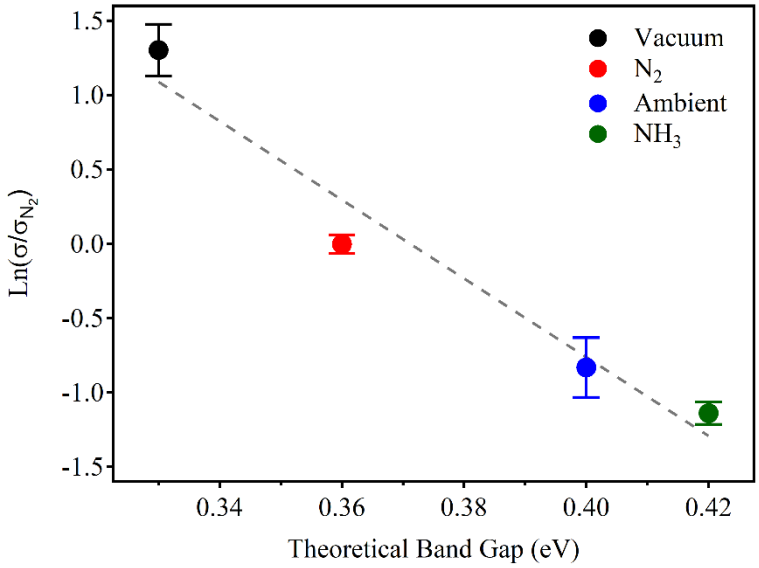

Figure 2-26 Average and standard deviations of Ln (σ/σ_{N_2}) values measured in circa 30 nm Cu-CAT-1 films compared with the theoretical band gap calculated for each gas environment. The gray dotted line is a linear fit of the data. Extracted from ref. 23.

Nevertheles, to get additional evaluations, we made Kelvin probe measurements (Figure 2-27A) where it was observed a large decrease of the contact potential difference (CPD) from 312±4 mV for the pristine Cu-CAT-1 film to 158±12 mV upon exposure to NH_3 vapors for 5 min. This translates in a work function difference of 0.15 eV (Δ_{CPD}=154 mV), same order of magnitude than the electronic changes predicted by DFT-calculations. As a reference, we performed the same experiment on a Glass/Au/C_{12}S substrate. In this case, we observed an initial CPD of -440±2 mV, which is essentially unvaried when exposed to NH_3 (Δ_{CPD}=25 mV). Moreover, we performed infrared reflection absorption spectroscopy (IRRAS) of the above Glass/Au/C_{12}S/Cu-CAT-1 films.

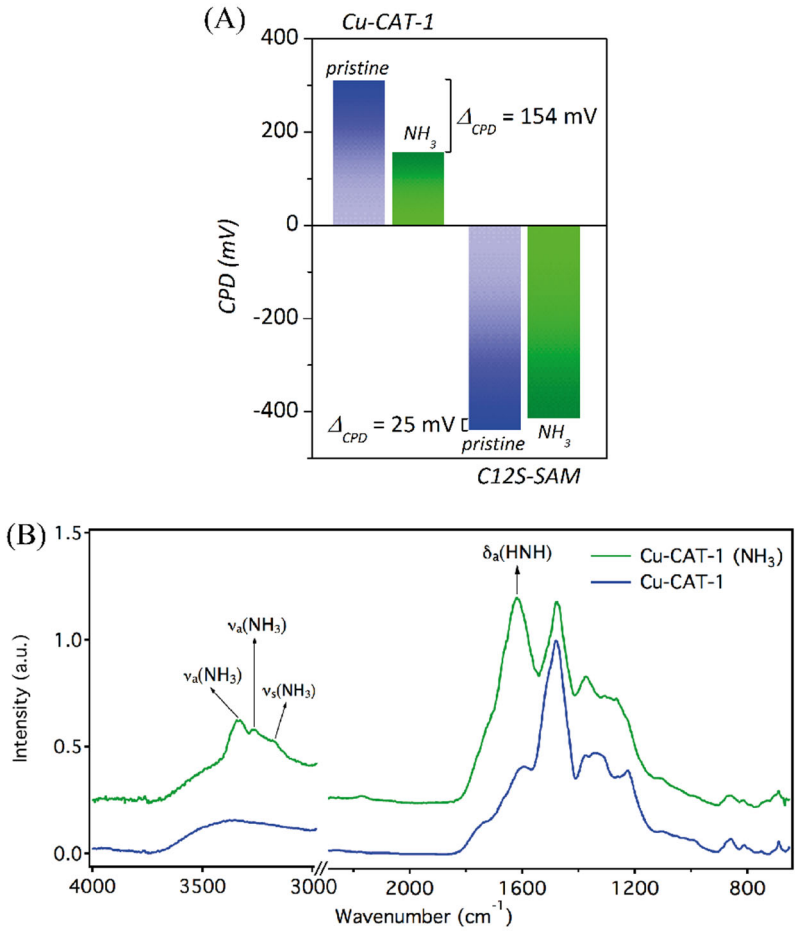

Figure 2-27 (A) Kelvin probe measurements of a Glass/Au/C_{12}S/Cu-CAT-1 film (top) and a reference Glass/Au/C_{12}S substrate (bottom), before and after exposure to NH_3 vapors. (B) IRRAS spectra of Cu-CAT-1 film before and after exposure to NH_3 vapors. Abbreviations: na asymmetric stretching, ns symmetric stretching, da asymmetric bending. Extracted from ref. 23.

Figure 2-27B shows the IRRAS spectra show after exposure to NH_3 the appearance of NH_3 stretching bands at 3336, 3265, and 3170 cm^{-1} and a strong bending peak at 1620 cm^{-1} result of the coordination of NH_3 to Cu^{II}[25]. Moreover, powder X-ray diffraction of the bulk microcrystalline solid also confirms reversible changes in the interlayer

separation of Cu-CAT-1 after exposure to NH_3 vapors, consistent with the DFT model. This data further demonstrates the strong interaction of NH_3 with Cu-CAT-1 thin films and points to guest-MOF interaction as the main responsible for chemoresistive response.

5. Conclusions

To study the electrical conduvity of the M-CAT family on pellets, we designed a four-point probe tool to carried out this task, and we confirm that Cu-CAT-1 displays the highest conductivity among the M-CAT family. After, we integrated Cu-CAT-1 in a FET device as ultrathin films which we observed an atmosphere dependence of σ vs t. Next, we developed a tool capable of doing measurements under different atmosphere included vacuum and controlling the temperature meanwhile the electrical response was monitored. With this set-up was possible to manage better gas consumption, time, temperature and also apply vacuum on the system to obtain more stable measures and faster gas exchange rates usefull to stuty the origin of the chemoresistive phenomenom.

In consideration of the study as such, our results indicate that the origin of the chemiresistive response of Cu-CAT-1 could be linked to the direct interaction of gas molecules with the Cu^{II} sites. This results in slight distortions of the internal structure of the layer or more acute changes in the coordination geometry of the metal node for concomitant modifications of the band gap of the solid. Our findings are also consistent with previous reports[11–13] that suggest a possible relationship between the nature of the metal nodes and the coordination ability of the analytes with the intensity and selectivity of the turn-on response. We are confident this information will be of use to help to

guide the design of advanced sensory platforms based on the rational optimization of the chemical functionality and electronic structure of MOFs.

6. Future work

Regarding the four-point probe, it could be adapted to perform spin-crossover conductivity measurements by implementing a temperature controller to the chamber. It also is possible to transport it into a glovebox to perform this measuring under inert atmosphere better fitted to study reactive films or substrates. Additionally, it could be also used to study the mechanical resistance of flexible MOFs by using the dynamometer to measure the pressure applied.

As regards to the controlled atmosphere chamber, it allows for direct electrical conductivity measurements with simultaneous control of guest injection and temperature. Accordingly, we can change the sample holder and adapt it to another type of applications like thermoelectrics measurements (measurement of Seebeck effect). Additionally, by replacing the blank KF40 Flanges with windows, it should be possible to combine electrical measurements with spectroscopy studies under different atmospheres or to study the modulation of electrical response with light. A possibility that I find particularly appealing.

7. Bibliography

1. Sun, L., Campbell, M. G. & Dincă, M. Electrically Conductive Porous Metal-Organic Frameworks. *Angew. Chemie Int. Ed.* **55**, 3566–3579 (2016).

2. Ko, M., Mendecki, L. & Mirica, K. A. Conductive two-dimensional metal-organic frameworks as multifunctional materials. *Chem. Commun.* **54**, 7873–7891 (2018).

3. Wu, G., Huang, J., Zang, Y., He, J. & Xu, G. Porous Field-Effect Transistors Based on a Semiconductive Metal-Organic Framework. *J. Am. Chem. Soc.* **139**, 1360-1363 (2017).

4. Rubio-Giménez, V. *et al.* Bottom-Up Fabrication of Semiconductive Metal-Organic Framework Ultrathin Films. *Adv. Mater.* **30**, 1704291 (2018).

5. Lahiri, N., Lotfizadeh, N., Tsuchikawa, R., Deshpande, V. V. & Louie, J. Hexaaminobenzene as a building block for a Family of 2D Coordination Polymers. *J. Am. Chem. Soc.* **139**, 19-22 (2017).

6. Huang, X. *et al.* A two-dimensional π–d conjugated coordination polymer with extremely high electrical conductivity and ambipolar transport behaviour. *Nat. Commun.* **6**, 7408 (2015).

7. Hmadeh, M. *et al.* New Porous Crystals of Extended Metal-Catecholates. *Chem. Mater.* **24**, 3511–3513 (2012).

8. Kambe, T. *et al.* π-Conjugated Nickel Bis(dithiolene) Complex Nanosheet. *J. Am. Chem. Soc.* **135**, 2462–2465 (2013).

9. Sheberla, D. *et al.* High Electrical Conductivity in Ni_3(2,3,6,7,10,11-hexaiminotriphenylene)$_2$, a Semiconducting Metal–Organic Graphene Analogue. *J. Am. Chem. Soc.* **136**, 8859–8862 (2014).

10. Cui, J. & Xu, Z. An electroactive porous network from covalent metal–dithiolene links. *Chem. Commun.* **50**, 3986–3988 (2014).

11. Campbell, M. G., Liu, S. F., Swager, T. M. & Dincă, M. Chemiresistive Sensor Arrays from Conductive 2D Metal-Organic Frameworks. *J. Am. Chem. Soc.* **137**, 13780-13783 (2015).

12. Campbell, M. G., Sheberla, D., Liu, S. F., Swager, T. M. & Dincă, M. Cu_3(hexaiminotriphenylene)$_2$: An Electrically Conductive 2D Metal-Organic Framework for Chemiresistive Sensing. *Angew. Chemie Int. Ed.* **54**, 4349–4352 (2015).

13. Yao, M.-S. *et al.* Layer-by-Layer Assembled Conductive Metal-Organic Framework Nanofilms for Room-Temperature Chemiresistive Sensing. *Angew. Chemie Int. Ed.* **56**, 16510-16514 (2017).

14. Smith, M. K., Jensen, K. E., Pivak, P. A. & Mirica, K. A. Direct Self-Assembly of Conductive Nanorods of Metal–Organic Frameworks into Chemiresistive Devices on Shrinkable Polymer Films. *Chem. Mater.* **28**, 5264–5268 (2016).

15. Smith, M. K. & Mirica, K. A. Self-Organized Frameworks on Textiles (SOFT): Conductive Fabrics for Simultaneous Sensing, Capture, and Filtration of Gases. *J. Am. Chem. Soc.* **139**, 16759–16767 (2017).

16. Miner, E. M., Wang, L. & Dincă, M. Modular O_2 electroreduction activity in triphenylene-based metal-organic frameworks. *Chem. Sci.* **9**, 6286–6291 (2018).

17. Melot, B. C. *et al.* Metallic Conductivity in a Two-Dimensional Cobalt Dithiolene Metal–Organic Framework. *J. Am. Chem. Soc.* **139**, 10863–10867 (2017).

18. Dong, R. *et al.* Large-Area, Free-Standing, Two-Dimensional Supramolecular Polymer Single-Layer Sheets for Highly Efficient Electrocatalytic Hydrogen Evolution. *Angew. Chemie Int. Ed.* **54**, 12058–12063 (2015).

19. Jia, H. *et al.* A novel two-dimensional nickel phthalocyanine-based metal-organic framework for highly efficient water oxidation catalysis. *J. Mater. Chem. A* **6**, 1188–1195 (2018).

20. Mendecki, L., Ko, M., Zhang, X., Meng, Z. & Mirica, K. A. Porous Scaffolds for Electrochemically Controlled Reversible Capture and Release of Ethylene. *J. Am. Chem. Soc.* **139**, 17229–17232 (2017).

21. Rubio-Giménez, V. Ultrathin films of layered coordination polymers: charge transport and spin crossover at the nanoscale. (University of Valencia, 2018).

22. Lee, K. H. *et al.* “Cut and Stick” Rubbery Ion Gels as High Capacitance Gate Dielectrics. *Adv. Mater.* **24**, 4457-4462 (2012).

23. Rubio-Giménez, V. *et al.* Origin of the Chemiresistive Response of Ultrathin Films of Conductive Metal-Organic Frameworks. *Angew. Chemie Int. Ed.* **57**, 15086–15090 (2018).

24. Foster, M. E., Sohlberg, K., Spataru, C. D. & Allendorf, M. D. Proposed Modification of the Graphene Analogue $Ni_3(HITP)_2$ To Yield a Semiconducting Material. *J. Phys. Chem. C* **120**, 15001–15008 (2016).

25. Nakamoto, K. *Infrared and Raman Spectra of Inorganic and Coordination Compounds Applications in Coordination, Organometallic, and Bioinorganic Chemistry*. (Wiley, 2009).

Chapter Three – Fabrication of molecular thin films for vertical charge transport: 2D Hoffman Clathrates thin films and Lanthanide–peptide SAMs

1. Introduction

The past three decades have witnessed a spectacular development of organic-based electronic and spintronic (spin–electronic) devices. Between them, digital displays based on organic light-emitting diodes (OLEDs) are already commercially available[1] and molecular photovoltaic devices have recently emerged as feasible competitors of silicon, with efficiencies reported of up to 20%, a fivefold increase in the last years.[2] This has demonstrated the great potential of new materials to impact on the development of new technologies. On the other hand, the hard disk storage capacity has been also influenced by spintronics, where spin-valves are used as a read head.

In this scenario, the properties related to the spin of the electron will help to develop new technologies in the close future.[3–9] Between them, we will focus on two of these effects.

Spin cross-over (SCO) phenomenon represents the paradigm of bistability at the molecular level.[10,11] In the particular case of Fe^{II} compounds, the low-spin (LS) to high-spin (HS) transition is associated with diamagnetic to paramagnetic switching as well as with profound optical changes.[12] This phenomenon was discovered by Cambi et al. as part of the study of iron (II) dithiocarbonate compounds in the early 1930s.[13] This effect has shown a potential application in nanotechnological devices such as memory storage units, sensors actuators and displays.[14–22]

Chirality-induced spin selectivity (CISS) is an effect displayed by helical molecules like DNA bound to a surface. Naaman and others[23-26] showed that the electronic transport along chiral diamagnetic

molecules produces a net spin polarization of the current, so called CISS effect, with potential application in memristor devices.[27]

In this chapter, we will study the deposition on a high conductive substrates and subsequent electronic transport of helical polypeptide Lanthanide Binding Tag (LBT) SAMs, with potential to present CISS effect, and a series of SCO Fe^{II} Hoffman Clathrate (HC) Coordination Polymers (CP) thin films.[28]

1.1. Lanthanide Binding Tags (LBT)

Polypeptides are derived from the combination of two or more amino carboxylic acid molecules (the same or different) linked together through the formation of a covalent bond from the carbonyl carbon of one to the nitrogen atom of the other with formal loss of water (Figure 3-1). The term is usually applied to structures formed from α-amino acids, but it includes those derived from any amino carboxylic acid.[29]

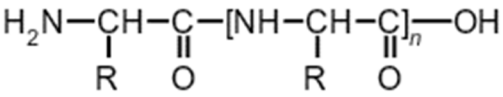

Figure 3-1 Scheme of polypeptide. R may be any organic group, commonly but not necessarily one found in natural amino acids. Extracted from ref. 29.

Herein, we will study the transport properties of a Lanthanide Binding Tag (LBT) polypeptide chain coordinated to Terbium (Tb) ions and deposited as one molecule thick films on gold surfaces to form Tb-LBT SAMs. LBT presents a unique ability to selectively coordinate a single lanthanoid ion. As a result, when it is inserted in other protein chains, it is used as a powerful mean of protein visualization and quantification techniques. Herein, we will focus on a LBT, very close to that first

described by Imperiali et al. (Figure 3-2A).[30–34] When LBTC is coordinated by a lanthanide, it acquires a right-hand helical structure

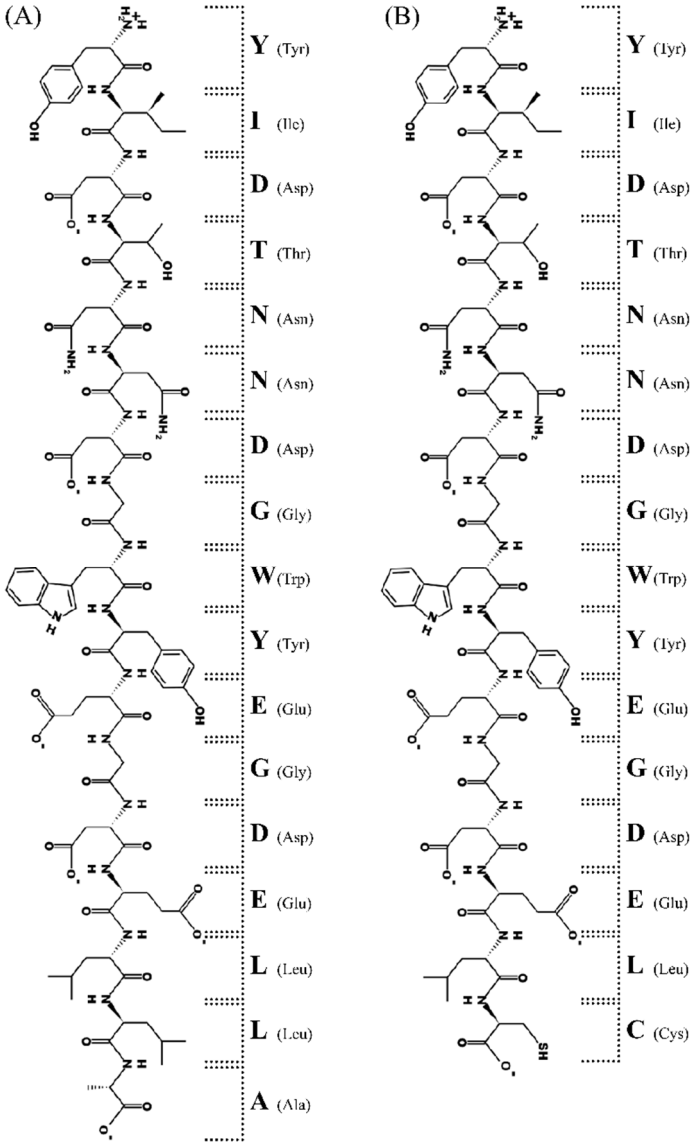

Figure 3-2 Protein chain scheme of (A) LBT (Protein Data Bank (PDB) id: 1TJB) and (B) LBT modified with a cysteine amino-acid to obtain LBTC.

with potential for CISS and coordinated to paramagnetic Terbium (III) lanthanide ion. Moreover, to link it to the gold surface, final amino-acids (LA) has been replaced by a thiol-containing amino-acid (C)[35] to render a new peptide with formula YIDTNNDGWYEGDELC (Figure 3-2B and Figure 3-3) so called LBTC.

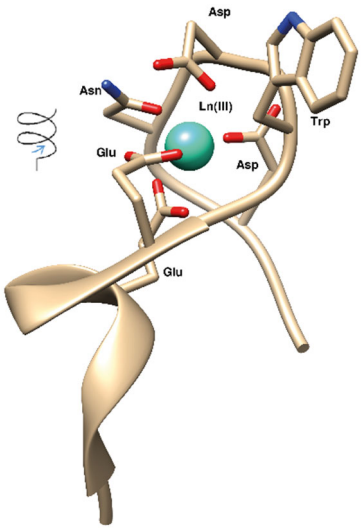

Figure 3-3 Three-dimensional (3D) structure of the LBTC on the right-hand helical of the global structure of the polypeptide.

1.2. Spin-Crossover Hoffman Clathrates (SCO-HC)

Fe^{II} Hoffman Clathrates are a class of CPs composed by metal-cyanide-metal layers with formula $[Fe(L)_2\{Pt(CN)_4\}]$, vertically joined together by aromatic nitrogen-based pillaring ligands (L) coordinated to octahedral Fe^{II} metal ions. Depending on the connectivity of these linkers, they can form either 2D or 3D structures. The latter display intrinsic porosity due to the 1D channels that run parallel to the metal-cyanide planes, while the formers are not intrinsically porous in the bulk form as their monodentate pillaring ligands yield interdigitated structures due to π–π interactions. As we

have recently demonstrated, in the case of 2D HC $[Fe(py)_2\{Pt(CN)_4\}]$ (py = pyridine), this spin-crossover ability is retained when Fe^{II}-HCs are processed into nanometric thick films.[36] Moreover, in a previous report, Kitagawa and collaborators showed the appearance of an unprecedented gate-opening response to guests in ultrathin

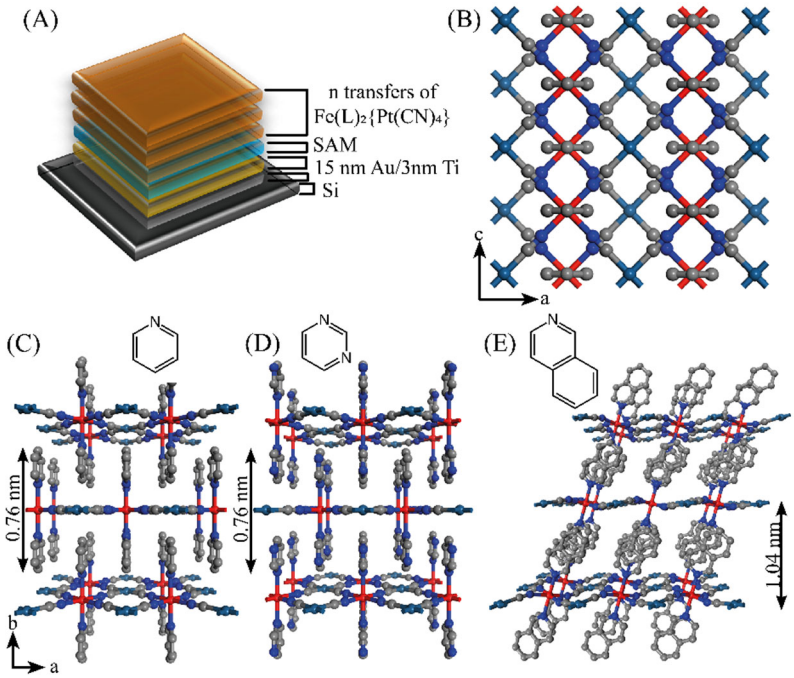

Figure 3-4 (A) Device architecture composed by a SiO_2 substrate, 3nm of Titanium adhesion layer, 15 nm of Gold, a 4-mercaptopyridine SAM and n layers of $[Fe(L)_2\{Pt(CN)_4\}]$. (B) Perspective of the metal-cyanide layer along the b axis in $[Fe(py)_2\{Pt(CN)_4\}]$. (C) Side views of $[Fe(py)_2\{Pt(CN)_4\}]$, (D) $[Fe(pym)_2\{Pt(CN)_4\}]$ and (E) $[Fe(isoq)_2\{Pt(CN)_4\}]$ showing the planar (C and D) and corrugated (E) layers vertically stacked together thanks to π-π interactions between the axial ligands. The thickness of a single increases from 0.76 nm (C and D) to 1.04 nm (E). Color code: Fe, red; Pt, turquoise; N, blue; C, grey.

$[Fe(py)_2\{Pt(CN)_4\}]$ films.[37] Curious about this phenomenon and the possibility to integrate these materials into responsive electronic

devices, we decided to prepare a series of 2D HCs (A) with py and two additional py derivatives as axial ligands (Figure 3-4B and C), pyrimidine (pym) with an extra N donor atom (Figure 3-4D) and isoquinoline (isoq) with an additional aromatic ring (Figure 3-4E).

2. Fabrication of LBTC and HC thin films over conductive substrates using QCM set-up

As a previous step for its integration into devices and for study their electrical properties once grafted on a conductive surface. Recently, my colleagues from RTMM and FUNIMAT have successfully deposited (Tb)-LBTC and HC thin films using dip-coating and LbL, respectively. Nevertheless, this process could not be monitored in-situ. We will study the deposition of LBTC, Tb-LBTC and $[Fe(L)_2\{Pt(CN)_4\}]$ HCs on surfaces using an automatized Quartz Crystal Microbalance (QCM) set-up that has been developed specifically for this purpose. QCM has been used before to monitor the deposition of SAMs,[38] CP[39] and MOFs.[40] However, it has not been applied to HC.

To be able to grow of molecular structures in an automatic way meanwhile monitoring the deposition process, we developed an automatized set-up (Figure 3-5A). For this aim, we refurbished an old Quartz Crystal Microbalance (QCM) with a continuous flow chamber with a peristaltic pump and a 6-way Multiposition Valve Actuator (Figure 3-5B).

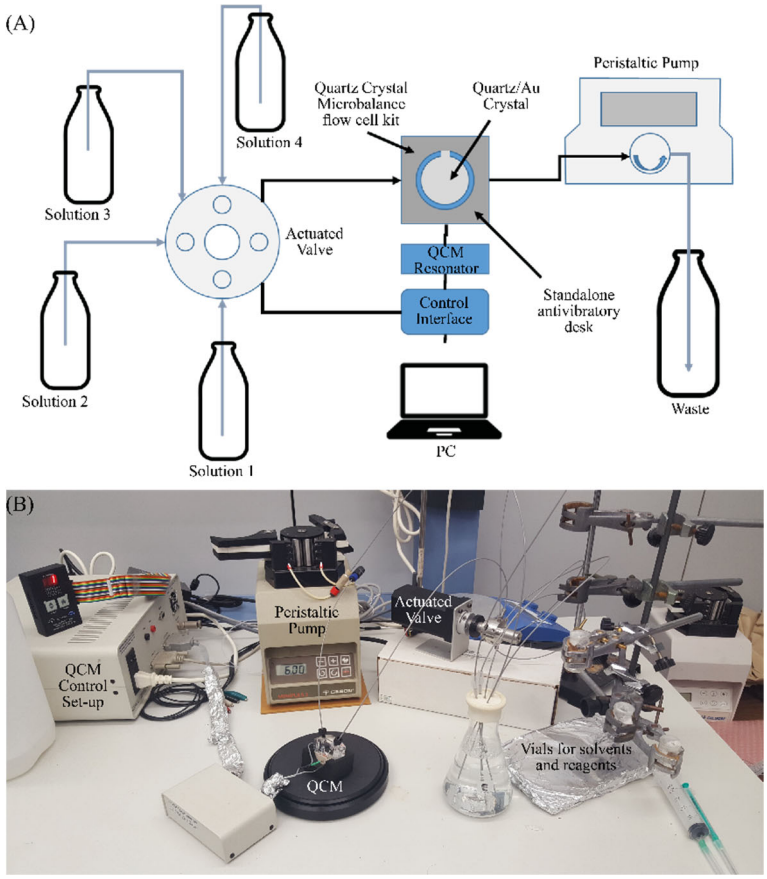

Figure 3-5 (A) Sketch of the QCM set-up used in this study, and (B) The actual automated QCM set-up where the QCM, peristaltic pump, actuated valve and vials for the solvents and reagents can be observed.

We used a Model 400 Electrochemical Quartz Crystal Microbalance (CHI Instruments) consisting of a potensiostat/galvanostat (CHI440), an external box with oscillator circuitry and EQCM cell. The EQCM cell consists of two Teflon pieces, two screws to keep both pieces together and between them, the Quartz Crystal. The Quartz crystal microbalance works measuring the working frequency with respect to the reference frequency difference thorough the experiment. The reference crystal has an oscillation frequency of ~8 MHz, the working

crystal oscillation frequency can be in the range 7.995 MHz and -7.950 MHz.

The Multiposition Valve Actuator (Microelectric EMTMA-CE) consists of a stepper-motor/gearbox assembly a manual controller, a universal AC input (100-240 V_{AC}, 50-60 Hz) to 24 V_{DC} power supply, and the interconnecting cables. The valve has six different inputs and one output. Thanks to this, it can deliver six different reagents. It uses pipes of 0.381 mm inner diameter and an external diameter of 1.5875 mm.

The flow during the experiment is adjusted using a peristaltic pump. Peristaltic pumps are the best options when it is necessary to move a fluid without turbulence, thanks to the fact that it displaces the fluid through the pipe without creating abrupt movements and producing bubbles on it. We used a Gilson MINIPULS 3 pump operating at 220 V. This pump has up to four channels and accept tubing size from 0.2 mm to 4 mm (internal diameter). The peristaltic pump is controlled using a home-made TTL connector and controller. The maximum back pressure is 500 kPa with a flow of up to 45 mL/min. In our specific case, I have employed a tubing size of 1.14 mm and a wall of 0.91 mm on full power the flow was around 600 µL/min.

The QCM acquisition data is controlled by its own software, while the valve position and pump speed and direction using a homemade piece of LabVIEW software.

To estimate the relation between QCM working frequency changes and mass loading we can use the Sauerbrey's equation.[41]

$$\Delta f = \left(- {}^{2f_0^2}\Big/ {}_{A\sqrt{\mu\rho}} \right) \Delta m = f_{working} - f_{reference}$$

where f_0 is the reference frequency of Quartz Crystal, Δf is the change in the frequency of quartz microbalance due to the mass change (Δm) of electrodes. A is the active area (0.205 cm^2), ρ is the density ($2.648\ g/cm^3$), and μ is the shear modulus of the quartz crystal ($2.947 * 10^{11}\ g/cm * s^2$) according to the manufacture's specifications for 8 MHz crystal. In our system the mass change of 0.14 ng corresponds to 0.1 Hz frequency change.

2.1. Fabrication of 2D Hoffman-type CP $[Fe(py)_2\{Pt(CN)_4\}]$ films

We studied the sequential deposition of HC $[Fe(py)_2\{Pt(CN)_4\}]$ using QCM and compared with the results obtained using the LbL assisted approach.[37] As in the previous case, the electrode was cleaned with piranha and rinsed with distilled water. Then it was functionalized with 4-mercaptopyridine 1mM incubated for 24 hours to allow for the first metal layer to anchor on the surface, as my coworkers have reported previously.[42] Finally, it was inserted into the microbalance, then sealed, and ethanol injected into the chamber until a stable reference frequency was obtained. Next, $[Fe(py)_2]^{2-}$ and $[Pt(CN)_4]^{2+}$ ethanol solutions were alternatively injected, absolute ethanol was used to clean the chamber of the previous solution. These three cycles constitute one transfer (Figure 3-6). This sequence was repeated up to twenty transfers. We tested several flows (e.g. 100 to 600 µL/min) and injection step times (e.g. 1000 s to 180s). Figure 4-8 shows optical microscope images of

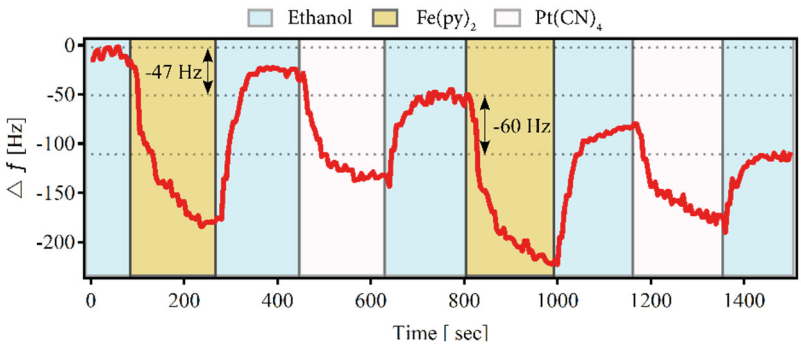

Figure 3-6 Sequential deposition of $Fe(py)_2$ and $Pt(CN)_4$ solution with a rinsed cycle of absolute ethanol. Graph displays two HC transfers cycles. The flow employed was 600 µL/min per step and 180s injection. Δf per transfer in average was -53 Hz.

the comparing deposition of a twenty transfers films obtained by LbL (Figure 3-7A) with the worst (Figure 3-7B) and the best QCM films (Figure 3-7C). The worst results were obtained using a flow rate of 100µL/min with 1000s injection steps of $Fe(py)_2$ and $Pt(CN)_4$, and 400s of absolute ethanol rising, while the best results were obtained increasing the flow up to the max delivered by the pump, 600 µL/min with 180s per step. The results have shown that the flow is more important than the deposition time. Better quality films were obtained when the flow was increased.

We noticed that the cleaning step between metal and ligand injection was especially important. In general we also noticed that the mixing of metal and ligand produced the precipitation and formation of uncontrolled crystallites of $[Fe(py)_2\{Pt(CN)_4\}]$ onto the electrode as it is observed in Figure 3-7B. Despite increasing the flow, the maximum pump flow was not enough to release completely the previous reagent pump flow was not enough to release completely the previous reagent allowing the crystallization inside the crystal chamber. According to these observations and taking account that the effective area is

0.204 mm^2 and the unit cell for $Fe(py)_2\{Pt(CN)_4\}$ is 7.3·7.4 $Å^2$, the expected change for 100% coverage would be ~230.316 Hz or 322.44 ng. In turn, the experimented change was 53±5 Hz equivalent to 74.2±7 ng. This corresponds to a coverage of only ~23.33% per transfer cycle. This is likely responsible for the high density of imperfections displayed by the films that generally displayed poorer qualities (red square in Figure 3-7C) than those obtained using the LbL assisted method (Figure 3-7A).

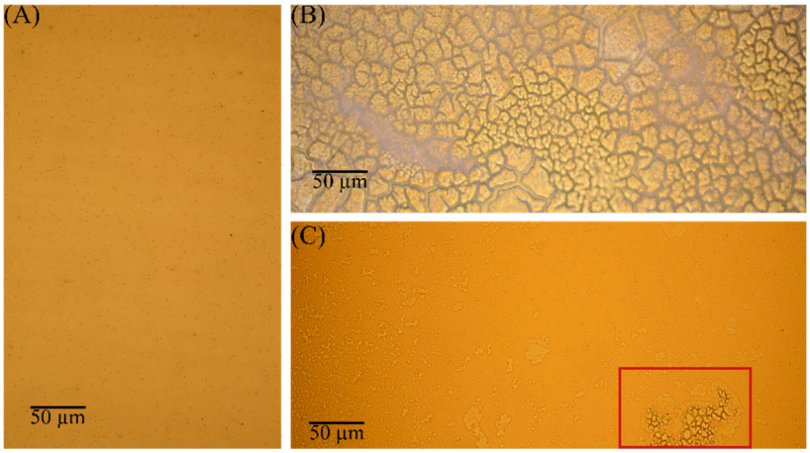

Figure 3-7 Optical characterization (50x) of film produced by means of (A) automated LbL set-up, (B) QCM method 1000s per Fe and Pt solution and 400s per Ethanol with a flow of 100 µl/min, (C) QCM method 180s per each step, Fe, Pt solution and Ethanol Absolute with a flow of 600 µl/min.

Up to this point, we have studied the deposition of Tb-LBT and HC $[Fe(py)_2\{Pt(CN)_4\}]$ using QCM, confirming the self-organization of the Tb-LBT on an Au surface and ruling out the possibility of using the continuous flow as a method to create HC $[Fe(py)_2\{Pt(CN)_4\}]$ thin films with the high quality required to study the electrical transport properties.

2.2. Fabrication of LBTC and Tb-LBTC thin films

To prepare LBT SAMs the QCM crystal was cleaned with a fresh piranha solution (H_2SO_4:H_2O_2) and then rinsed with distilled water. Next, the Crystal was inserted on the Microbalance Chamber, it was then sealed and a test solution injected with the aid of the valve and the peristaltic pump with a constant flow of 100 µL/min while recording

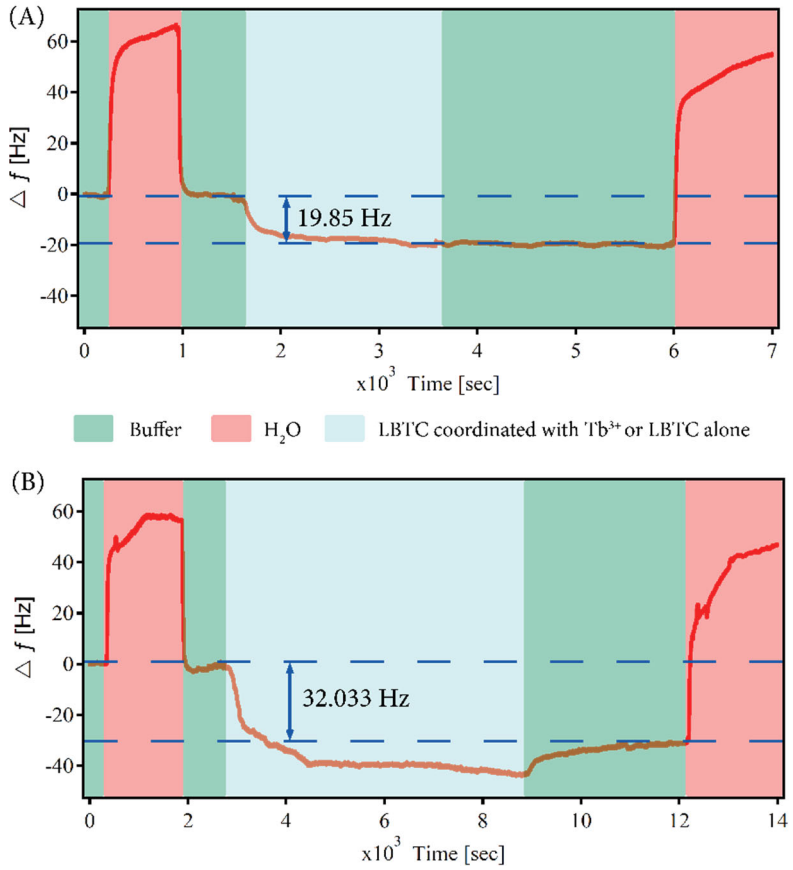

Figure 3-8 QCM measures. frequency shift (Δf) recorded while the crystal was sequentially exposed to distilled water, buffer (HEPES), and (A) LBTC coordinated with Tb^{3+} or (B) uncoordinated LBTC. Then exposed to buffer to clean and distilled water to finish the experiment.

the frequency shift response as a function of time ($\Delta f \ vs \ t$). Reference frequency was adjusted using pH = 7 HEPES buffer [HEPES, (4-(2-hydroxyethyl)-1-piperazineethanesulfonic acid)]. Once a stable frequency signal was obtained, the next solution was injected. This process was repeated following the other shown in Figure 3-8. The test solutions injected were distilled water, and depending of the case, LBTC coordinated with Terbium (Figure 3-8A) or uncoordinated LBTC (Figure 3-8B). Water injection results in a rise of frequency as a result of the removal of the HEPES ions physisorbed over the surface and the addition of the Tb-LBTC leads to a negative shift of frequency, characteristic of mass absorption over the QCM gold crystal.

To calculate LBTC coverage from the observed frequency shifts, we used two different theoretical models (Figure 3-9). Considering that in the absence of the lanthanide, LBTC keeps its tertiary structure based on LBTC crystal structure, simplified area per molecule and packing models can be estimated:

- Model A: the molecule is considered as a cube of 1.7 nm side.
- Model B: the molecule is considered a sphere whose projection on the surface is a circle of 1.6nm diameter

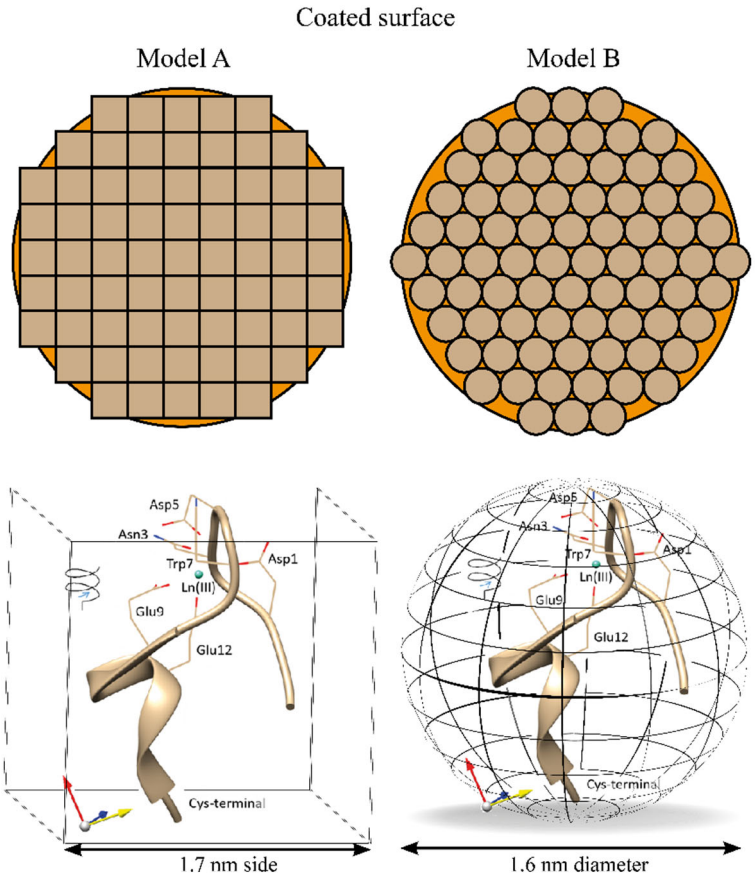

Figure 3-9 Area of the base considered to calculate theoretical coverage of the polypeptide according to the two models proposed, Model A on the right and Model B on the left.

Following these models, the theoretical coverage was calculated obtaining the values collected in Table 3-1.

Table 3-1 Theoretical Δf obtained from the Model A and B compared to the Experimental Δf to obtain an estimated coverage.

Molecule	Model	Theoretical Δf [Hz]	Experimental Δf [Hz]	Coverage
LBTC	A	15.85	30	189%
	B	20.64		145%
Tb-LBTC	A	17.22	20	116%
	B	25.00		80%

As observed in Figure 3-8A changes are 20 Hz for Tb-LBTC, giving rise to a range of coverage between 80 and 116% considering model B and the model A respectively, for LBTC the frequency shift measured is one third higher than for Tb-LBTC (ca. 30Hz vs 20Hz). This indicates a coverage of 145 and 189%. The weight of a single molecule of LBTC uncoordinated and coordinated with Tb^{3+} were $2.2 \cdot 10^{-8}$ and $2.4 \cdot 10^{-8}$ g respectively.

From the analysis of these results, we believe that when Tb^{3+} complex is used the thiol groups are attached to the gold and almost all the surface is covered. However, the large amount of material estimated when the Tb^{3+} is not present in the solution, can be only justified by two different explanations: (i) intermolecular polypeptide-polypeptide interactions are stronger than intramolecular interactions forcing a less globular shape and permitting a higher coverage of the surface, especially in the absence of the metal ion (Figure 3-10A) or (ii) a second layer is formed on top of the first layer (Figure 3-10B). From our point of view, the second option is less probable due to rising with buffer produce a Δf change from releasing a possible second layer and in presence of Tb^{3+} ion it does not happen.

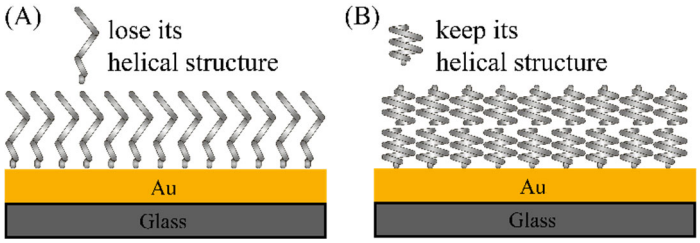

Figure 3-10 Scheme of the two different explanations: (A) intermolecular polypeptide- polypeptide interactions are stronger than intramolecular interactions forcing a less globular shape and permitting a higher coverage of the surface, or (B) a second layer is formed on top of the first layer.

In addition, it is important to clarify that the molecular weights of LBTC and Tb-LBTC are not precise, as the number and kind of counter ions and amount of hydration molecules linked to LBTC and Tb-LBTC on the surface are unknown. We have considered the simplest situation where protons compensate negative charges of the polypeptide, this means that the final coverages estimated are upper limits.

On the next section, we will focus our attention to probe the molecular transport properties of $Fe(L)_2\{Pt(CN)_4\}$ films and TbLBTC SAMS by using Ga_2O_3/EGaIn liquid contact junctions. For simplicity both films were grown on Si/Au substrates using either incubation or LbL techniques, respectively.

3. Designing a vertical set up to study electrical transport on low conductive films

The biggest problem to study the electrical transport properties on low conductive films is that the contacts should be very close. Resistance increases with contact distance. Moreover, to produce lateral contacts with gaps of less than few micrometers is a challenging task. To puzzle out this problem the contacts can be fixed vertically, in this case contact

distance is imposed by the film thickness, but this configuration brings a new disadvantage, how do we avoid short-circuits in very thin films during contacting?

This disadvantage can be released using liquid metals as the top electrode. The most common choice as liquid metals are Hg or Eutectic Gallium-Indium (EGaIn). EGaIn presents a Ga_2O_3 thin layer that avoids its diffusion through the molecular layer. This technique has been widely used to measure self-assembly monolayers (SAMs),[43] and in some cases to measure metal-organic frameworks (MOFs)[44,45] and coordinated polymers (CP).[42] In the case of MOFs, we have observed that we obtain more working junctions, that is, junctions that do not present short-circuits, when we use EGaIn, probably as a result of its different viscosity (Figure 3-11A and B) compared to Hg.

To produce liquid contacts, we used a set-up (Figure 3-11C) composed by a test stand (Mecmesin), a hanging mercury drop electrode (ICnf) or a syringe (Hamilton) filled with EGaIn, a microscope objective (Nikkon, 5x), a CCD Camera (Thorlabs) and a micrometric 3-axis roller block (Thornlabs) to position the sample. Everything was mounted on an optical bread board (Thorlabs). Contact area was determined from the radius of the liquid metal/substrate junction with the aid of the CCD camera and the microscope objective.

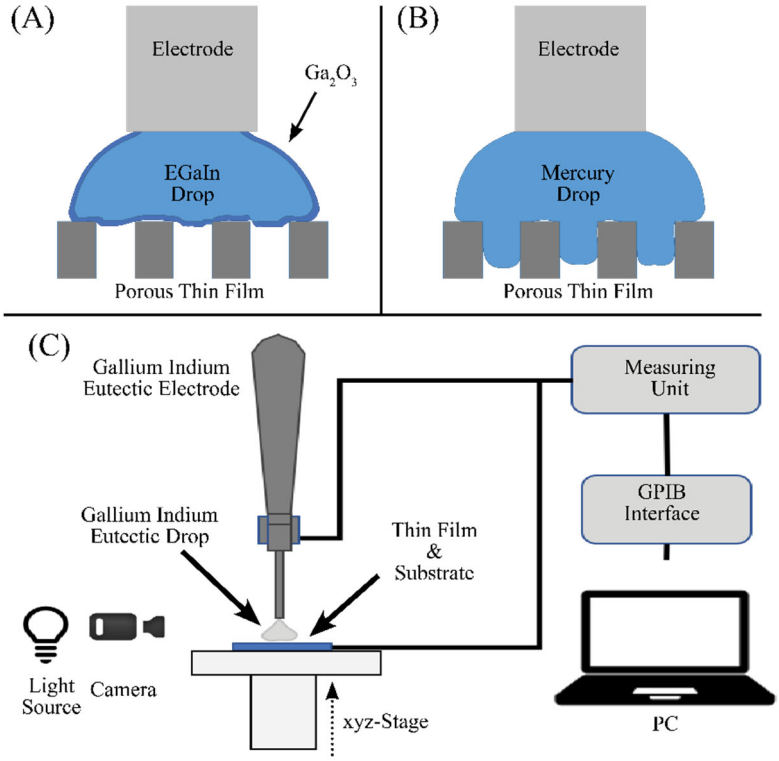

Figure 3-11 (A) Behavior of a Gallium Indium Eutectic drops and (B) a Mercury Drop on a porous film. (C) Scheme of the Hanging Drop Electrometer used in this thesis.

3.1. Vertical transport on $Fe(L)_2\,Pt(CN)_4$ HC films

We measured electronic transport through $Fe(L)_2Pt(CN)_4$ films were the pillaring ligand (L) was pyridine (py), pyrimidine (pym) or isoquinoline (isoq). Due to the fact that the films produced with continuous flow method were of poor quality, we prepared the films using the LbL assisted method, which consists in the sequential immersion of the mercaptopyridine SAM functionalized Au substrates in ethanol solutions of $Fe(BF_4)_2$ and $(TBA)_2Pt(CN)_4$ (TBA = thiobarbituric acid) with an excess of the respective axial ligand (Figure 3-12).[37]

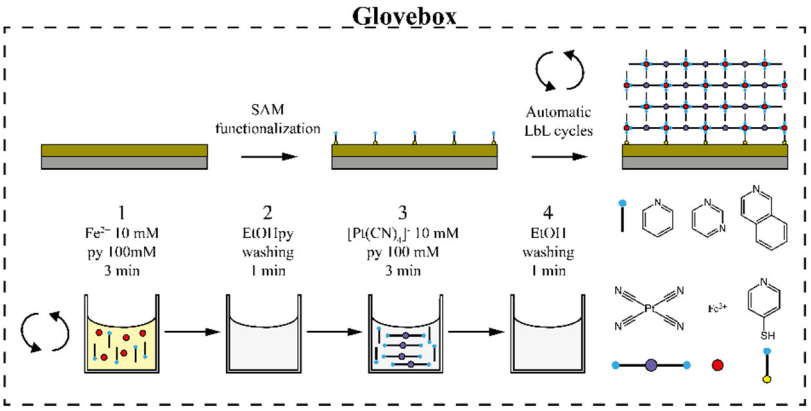

Figure 3-12 Automated LbL ultrathin film fabrication process of $[Fe(L)_2\{Pt(CN)_4\}]$. Scheme detailing the structure of the films and the LbL process with the four different molecular components of $[Fe(L)_2\{Pt(CN)_4\}]$: the axial ligands, the $[Pt(CN)_4]^{2-}$ complex, the Fe^{2+} ions and the mercaptopyridine SAM. A SAM-functionalized Si/Ti/Au substrate is sequentially immersed in ethanol solutions of the molecular components, (1) first Fe^{2+}/L and then (3) $[Pt(CN)_4]^{2-}$/L with intermediate (2 and 4) washing steps of pure ethanol. Sequential cycling for controllable film thickness is done with an automatic dipping system to ensure reproducibility. The whole process is carried out inside the glovebox to avoid Fe^{II} oxidation.

To study the electrical transport properties of HC $[Fe(L)_2\{Pt(CN)_4\}]$ films we used $Au/Fe(L)_2\{Pt(CN)_4\}//Ga_2O_3/EGaIn$ liquid contact junctions (Figure 3-13) with areas ranging from ~ 3200 to ~ 12000 μm^2. The contact to the bottom gold substrate was accomplished using gold wire and silver paste. The area of the contact was determined with the aid of a CCD camera and the current densities (J) of the molecular junctions measured as a function of the voltage. Data was recorded using a Keithley 6517B electrometer controlled with LabVIEW (National Instruments).

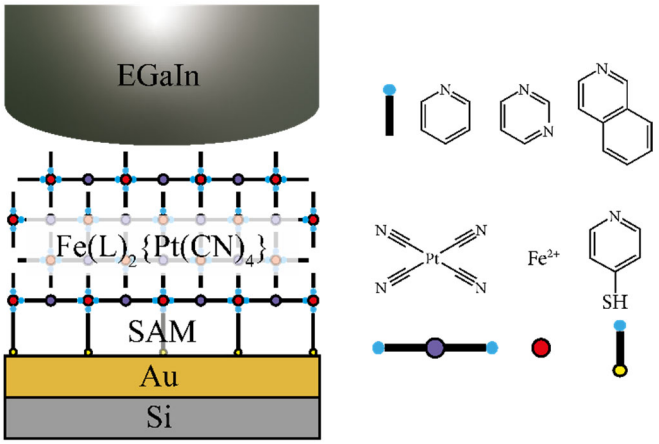

Figure 3-13 Scheme of the junction used to measure [Fe(L)$_2${Pt(CN)$_4$}] series. Left: Au/Fe(L)$_2${Pt(CN)$_4$}//Ga$_2$O$_3$/EGaIn liquid contact junctions. Right: different parts that conform the HC.

First, we studied a 10 transfer films. We formed different junctions and collected ten consecutive I-V scans for each junction between -0.2 and 0.2 V for a given drop size increasing the voltage above ±0.2 V generally lead to the breaking of the junction. From these data, we calculate the current density (J=*I*/A) vs voltage applied at 0.1 V.

Once ten I-V scans were recollected, we displaced the sample laterally with the XYZ-stage, produced a new Eutectic Gallium-Indium drop and repeated the process all over again. To improve statistics, we repeated this process at least 10 times on various parts of the film surface and collected at least 90 curves I-V for each sample (Figure 3-14A). As displayed in Figure 3-14B we observed a wide distribution of J values for each sample. The center of this distribution corresponds to the average Log J of the sample.

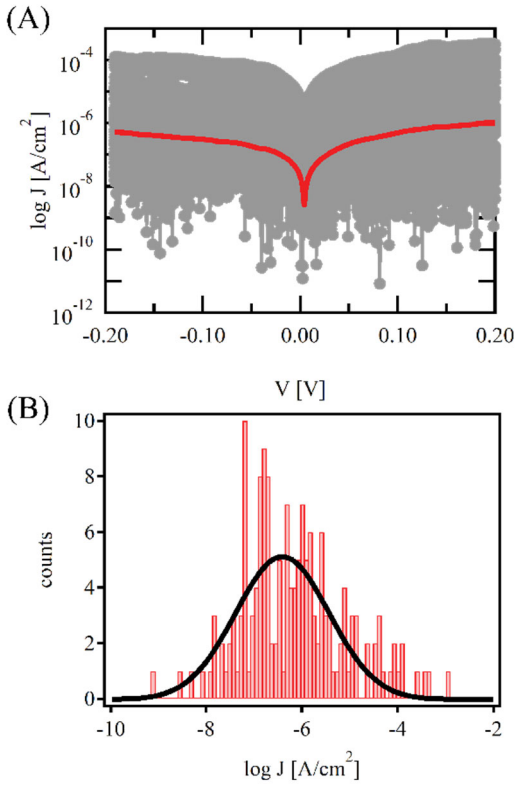

Figure 3-14 (A) All 100 log J curves measured in different points along the substrate and their average highlight on red. (B) Log J histogram at ± 0.12 V measured for a 4-transfers $Fe(py)_2\{Pt(CN)_4\}$ film thickness and gaussian fit to the data. Average value from the fit Log J.

To test if the great dispersion on the sample was linked to the deposition technique used, we separated the experimental data in three different groups depending on the distance to silver paste contact used as bottom electrode were the I-V curves were collected. The three distances were $\sim 9mm$, $\sim 6mm$ and $\sim 3mm$ (Figure 3-15A and Figure 3-16). Substrate size was 10 mm per 30 mm.

As we can observe I-V curves taken on the central part show a narrower dispersion, this reflects the way in which the samples of the substrate

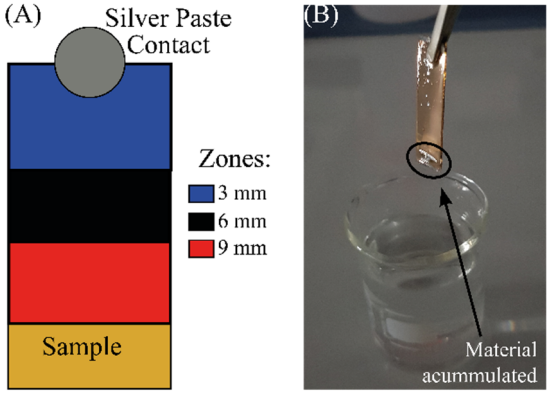

Figure 3-15 (A)Diagram of the different areas measured on the sample. (B) Sample after being submerged vertically on a solution.

are prepared. On the deposition process, the sample is submerged vertically (Figure 3-15B) on the different solutions, owing to that the farthest part of the sample gets more amount of material than the nearest part to the clamp used to hold the sample. The nearest part to the contact corresponds to the zone of the sample that left the solution in the first place. As a result, I-V were measured in the middle of the sample were the thickness expected to be more homogeneous. Although in that case, the width of the distribution is smaller compared to the other two zones (Figure 3-16), there is still some experimental variation in the J-V curves collected for a given sample that can be attributed to the presence of small local variation of thickness, roughness or structure and/or to errors on the estimation of the drop diameter.

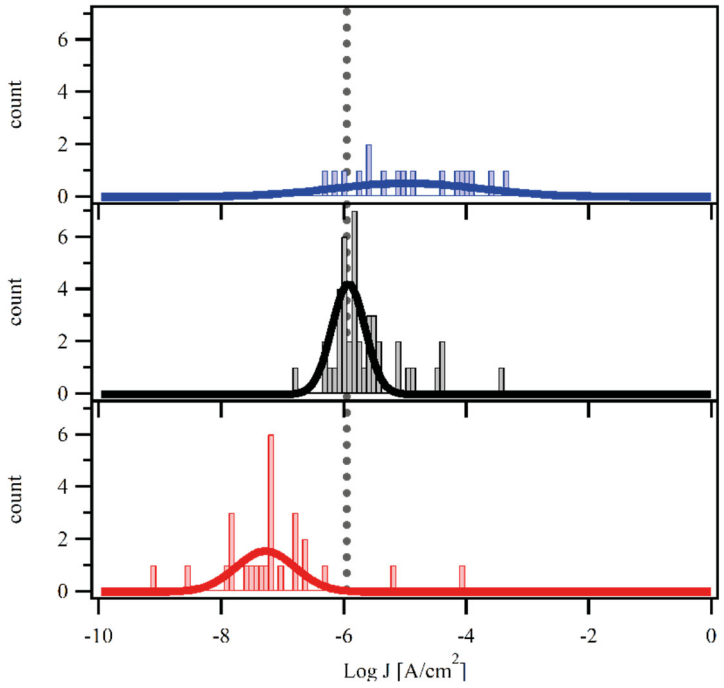

Figure 3-16 Log J Histograms measured on different areas on a ten transfer [Fe(isoq)$_2${Pt (CN)$_4$}] films. Blue up to 3mm, Black up to 6mm and Red up to 9 mm. Grey line is a guide for the eye.

Depending on the thickness/number of transfers, we obtain different dispersion widths as we can observe in Figure 3-18. On samples with few numbers of transfers (i.e. 3 transfers with a thickness of 3nm), width of the distribution was smaller (Figure 3-18 isoq, $Log\ |J| \approx\ -\ 0.5\ A/\ cm^2$). However, on samples with several number of transfers (e.g. 10 transfers with a thickness of 10 nm), we observed histograms with wider log J dispersion values (Figure 3-18 isoq, $Log|J| \approx -5.8\ A/cm^2$). This can be results of the increased roughness of RMS 3.2±0.8 nm and RMS 5.6±1.1 nm respectively, as confirmed by AFM.

Next, and using the same procedure as described before we collected I-V data on the central part of the substrate for each HC film after 1-15 transfers. Log J-V are symmetric within the testing window, scale down for increasing film thickness and display the expected V-shape for a nonmetallic contact (Figure 3-17). Again current density

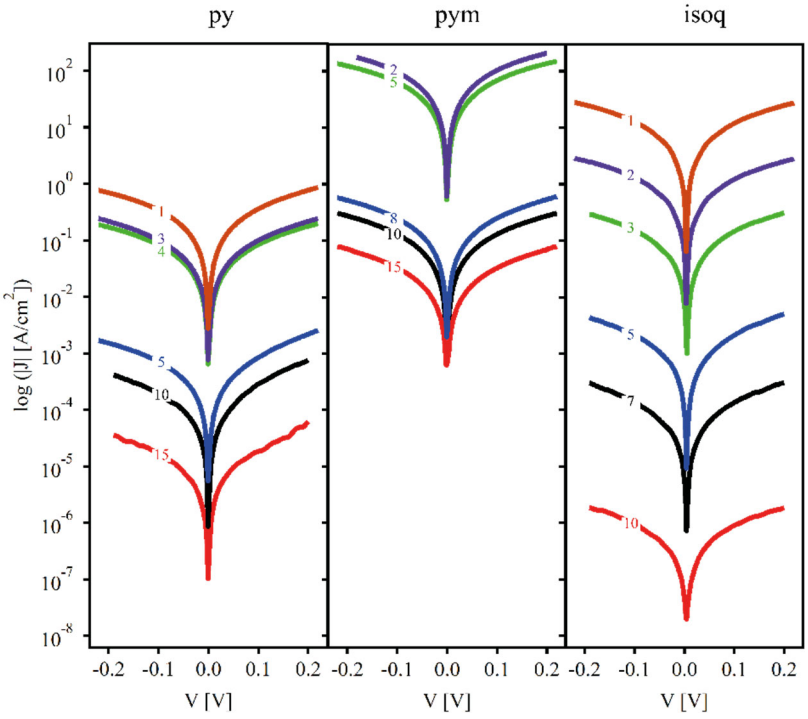

Figure 3-17 [Fe(L)$_2${Pt(CN)$_4$}] average current density (log J=I/A) curves as a function of the applied voltage and the number of transfers. Curves are the average of at least 90 traces measured at various positions over the surface of each film. L means py, pym or isoq.

histograms at a given voltage were calculated from the measured |J(±V)| values calculated at ±0.1V. Figure 3-18 shows Log |J| histograms, gaussian fit to the data and average log |J| values. Table 3-2 shows the average log |J_0| and β values as a function of the thickness for [Fe(L)$_2${Pt(CN)$_4$}] with L as py, pym, and isoq.

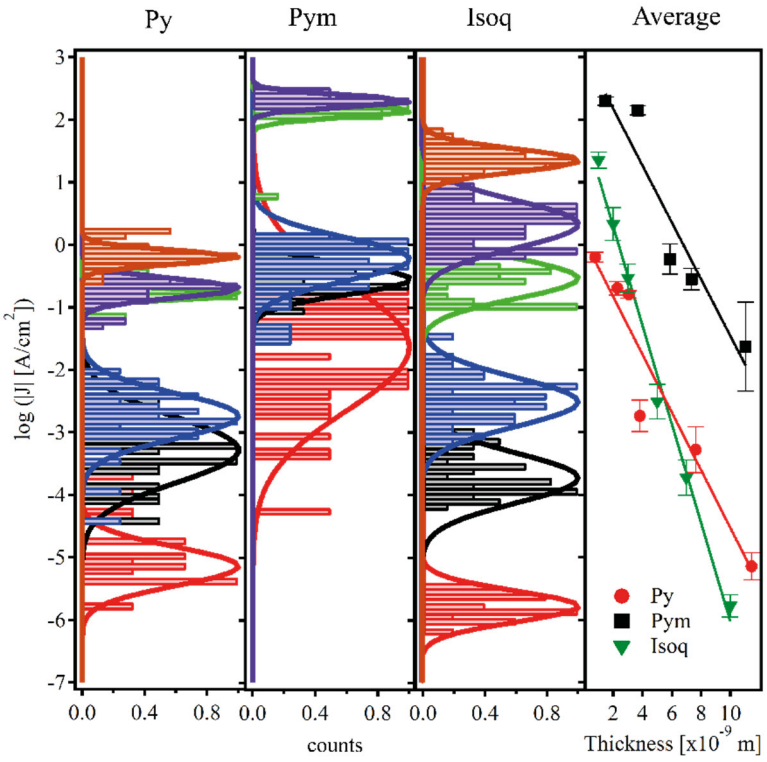

Figure 3-18 Electrical characterization of 2D Fe^{II}-HC ultrathin films. From left to right: Dependence of the logarithm of the absolute value of the current density (log | J |) measured at 0.1 V as a function of film thickness for $[Fe(L)_2\{Pt(CN)_4\}]$ films. L = py, pym, and isoq. Solid lines are gaussian fits to the data. Average log | J | values as a function of film thickness. Error bars correspond to the Gaussian width. Straight solid lines are a linear fit to the data according to log [$J= J_0+\beta$(thickness)/2.303]. β values are reported on Table 3-2.

Table 3-2 Attenuation factor (β), J_0 and interlayer distances for $[Fe(L)_2\{Pt(CN)_4\}]$ ultrathin films.

Ligand	$\beta[Å^{-1}]$	$\lvert J_0 \rvert [A/cm^2]$	d[Å]
py	0.035	0.09	7.63
pym	0.033	3.08	7.56
isoq	0.079	1.87	10.4

In order to extract information about the transport mechanism, these values were fitted our data to the Eq.3-1:

$$J = J_0 e^{(-\beta T)} \qquad \textbf{3-1}$$

where β is the attenuation factor intrinsic to the electronic properties of the film, d stands for its thickness, and J_0 is a factor that accounts for interfaces between film and electrodes.

According to the literature, the tunnelling mechanism is probably inadequate to describe charge transport across 2D Fe^{II}-HCPs and a multistep electron/hole hopping mechanism between redox sites is likely to be operative instead.[46] Analogously to what is customary for metal-molecule-metal junctions,[47] we used a linear fit of log J vs film thickness (T = d number of cycles) at a specific voltage (0.1 V) to extract the attenuation length (β); intrinsic to the electronic properties of the film and the contact current density J_0; a factor that accounts for the interfaces between the film ($[Fe(L)_2\{Pt(CN)_4\}]$) and the electrodes (py-S-functionalized Au and Ga_2O_3/EGaIn). β values in the >0.1-1 $Å^{-1}$ range account for a strong dependence of resistance with film thickness, which is indicative of a tunnelling regime. If there is a weaker dependence, the β value is lower than 0.1 $Å^{-1}$ which is usually attributed to a hopping regime. A transition between both regimes has been observed around this β value when varying the length of conjugated molecular wires[48–50] as well as in molecular wires of coordination complexes.[51] However, no shift in transport regimes has ever been observed in MOF thin films.[42,44,52] For our $[Fe(L)_2\{Pt(CN)_4\}]$ ultrathin films, the data can be fitted to a single straight line indicating a unique transport mechanism without any regime transition. As shown in Table 3-2, the obtained attenuation factors β correspond to

ca. 0.03-0.08 $Å^{-1}$. Those values are close to those reported for other conjugated organic molecular wires[50,53] but are well above those observed in some metal−organic molecular wires[51,54–57] and 3D CPs.[52] This is probably the result of the absence of covalent bonding between adjacent metal-cyanide layers. π-π interactions feebly contribute to electron delocalization and thus difficult electron hopping between metal centers. Similar β values (0.12 $Å^{-1}$) were reported for NASF-1, a 2D CP formed by planar layers (d = 9.3 Å) of Cu^{II} pairs and Co^{II}-tetracarboxylate porphyrins vertically stacked thanks to the π-π interactions between axial py ligands.[42,58] As previously, differences in the pillaring ligand are reflected in the electronic transport. Along the $[Fe(L)_2\{Pt(CN)_4\}]$ 2D Fe^{II}-HC series, the larger interlayer distance (d) of L = isoq further complicates interlayer electron transport and results in a higher β value for $[Fe(isoq)_2\{Pt(CN)_4\}]$ in spite of the stronger π-π interactions between the layers. Whilst the other two 2D Fe^{II}-HCs share similar interlayer distances and feature similar β values. It is worth noting that, despite all 2D Fe^{II}-HCPs being bond to the Au surface in an equivalent way through the py-SH SAM, at the time of junction formation they expose different interfacing groups toward the Ga_2O_3/EGaIn droplet that contribute differently to J_0. Within the series, L = pym with a donor heteroatom, displays the stronger interaction with the metallic top contact and thus yields a higher J_0 value.[59–61] This further highlights the importance of the of the axial ligand in out-of-plane charge transport processes involving 2D CPs.

3.2. Vertical transport on Tb-LBTC SAMs

Next, we measured electronic transport through Tb-LBTC SAM by following the same procedure described before. We collected I-V scans for a total of at least 30 different junctions and ~16 I−V scans for each

junction between −0.5 and 0.5 V. Unlike in the case of HC films LBTC junctions resulted stable up to ±0.5 V. As can be seen in Figure 3-19, in the vast majority of the junctions (>90%) the transport occurs through the SAM, with only a minority of short-circuits. This is supported by a decrease in the log of the absolute current density (log|J=I/A| in A·cm^{-2}) of roughly two orders of magnitude as compared to the reference sample without Tb-LBTC (top Figure 3-19A). At the working voltage of 0.15 V the logarithm of the current density log (|J|(A·cm^{-2})) = -1.18 ± 0.07 is close to that of Au substrates functionalized with 1 mM octadecanethiol ethanolic solutions, which in the same conditions was log(|J|(A·cm^{-2}) = -0.802 ± 0.005). Thus,

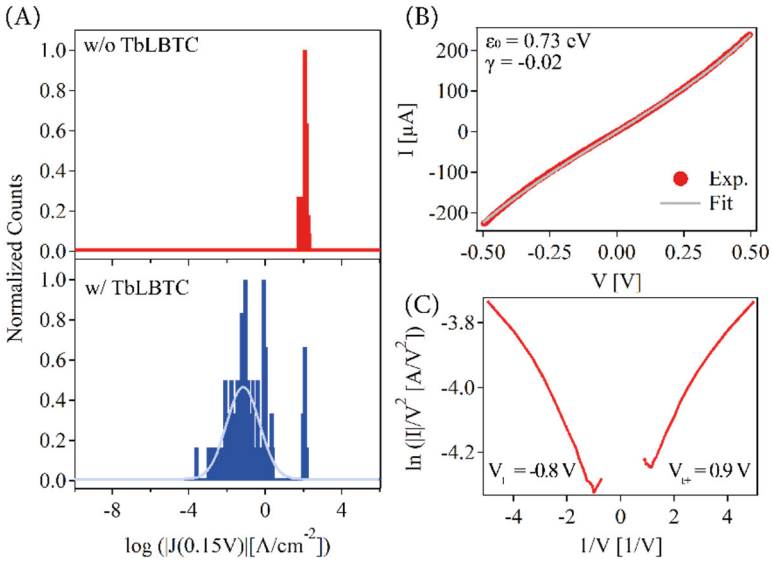

Figure 3-19 (A) log J histograms measured at V = 0.15 V on a reference sample without TbLBTC (top) and on a TbLBTC SAM (bottom). From the TbLBTC SAM measurements: (B) Representative I–V curve fitted using the single-level model with Lorentzian trans-mission and (C) Fowler−Northeim plot obtained from an I−V curve measured up to 1 V.

log J values are consistent with conduction in the tunneling regime.

Next, we employed the single-level model with Lorentzian transmission (sometimes referred to as the Newns–Anderson model) to analyze the experimental I–V curves and to estimate the Fermi energy (E_F)-molecular orbital energy offset ($\epsilon_o = E - E_F$) and the asymmetry of the potential profile (γ) along the junction.[62–64] These two values can be described as Eq. 3-2 and Eq. 3-3 respectively:

$$|\varepsilon_0| = 2 * \frac{e|V_{t+} * V_{t-}|}{\sqrt{V_{t+}^2 + \frac{10 * |V_{t+} * V_{t-}|}{3} + V_{t-}^2}} \qquad 3\text{-}2$$

$$\gamma = \frac{sign\ \varepsilon_0}{2} * \frac{V_{t+} * V_{t-}}{\sqrt{V_{t+}^2 + \frac{10 * |V_{t+} * V_{t-}|}{3} + V_{t-}^2}} \qquad 3\text{-}3$$

Transition voltage ($V_{t\pm}$) correspond to the change between tunneling and emission field conduction regimes. It can be obtained from a fitting of I-V curves or from experimental data using a Fowler-Nordheim (FN) plot (I/V^2 as function of $1/V$) which is known as transition voltage spectroscopy (TVS).[63]

I-V traces are nearly symmetric with respect to the origin and exhibit a nonlinearity that becomes more pronounced at higher bias. Fitting of the I–V curves up to ±0.5 V yielded ϵ_o = 0.68 ± 0.18 eV and γ= - 0.03±0.03 average values, a representative I–V curve and its fitting is shown in Figure 3-19B. In order to reveal the transition voltage (V_t), we collected additional I-V scans up to ±1 V. However, a bias voltage above ±0.5 V resulted in the breakdown of 100% of the junctions after only a few scans. From the data before junction breakdown, it was possible to estimate average V_{t+} and V_{t-} values of 0.85 ± 0.11 and 0.80 ± 0.08 V (ϵ_o = 0.710 eV, γ = 0.010 consistent with the previously

fitted parameters. The FN plot obtained from an I−V curve measured up to 1 V is displayed in Figure 3-19C.

This information combined with the change in the absolute value of the electrode work function (Φ) due to the adsorbed TbLBTC SAM, Φ_{SAM}= 4.62 eV (measured through a combination of Kelvin probe and ambient photoemission spectroscopy), led to the level alignment scheme of Au/TbLBTC//Ga_2O_3/EGaIn junction proposed in Figure 3-20.

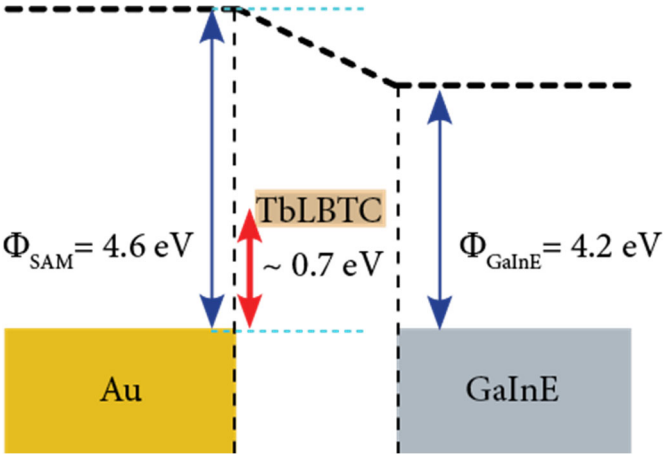

Figure 3-20 Schematic level alignment diagram of Au/Tb-LBTC//Ga_2O_3/EGaIn liquid junction.

Looking if Tb-LBTC present CISS effect, we upgraded EGaIn set-up to apply magnetic fields while I-V scans are collected (Figure 3-21). For doing that we inserted a permanent NdFeB magnet below the sample. The magnetic field applied was 350 mT and its direction could be inverted by turning the magnet before each new measurement. As a reference sample, we measured the spin polarization (SP) of ALA8 that is a right hand helical polypeptide chain with general formula (Boc)-Cys-(S-Acm)-(Ala-Leu)$_8$-NH-$(CH_2)_2$-SH.[65] ALA8 shows the same right-hand helicity than Tb-LBTC and show CISS effect as

reported by Naaman et al. using cyclovoltammetry measurements and photo emission in the presence of magnetic.[65] To measure this sample, we followed the same protocol previously described, we collected I-V scans in a total of at least 4 different junctions and ~16 I−V scans for each junction between −0.2 and 0.2 V. This time the procedure was done on the presence of a magnetic field positive (spin up), negative (spin down), and in the absence of magnetic field for a total of 12 junctions.

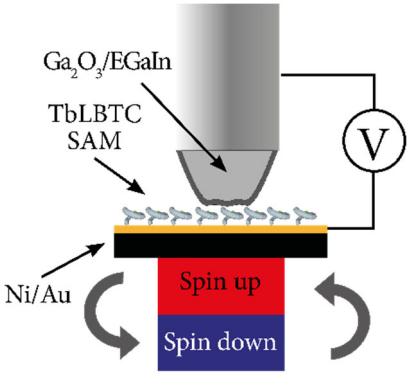

Figure 3-21 Set-up scheme employed to measure CISS effect

As show in Figure 3-22, ALA8 was more conductive on the presence of negative magnetic field than positive magnetic field in good agreement with the results obtained for this family of polypeptides previously reported by Naaman et al.[65]

The SP is defined by Eq. 3-4:

$$SP\% = \frac{I_+ + I_-}{I_+ - I_-} \qquad 3\text{-}4$$

where I_+ and I_- are the intensity with positive and negative magnetic field respectively. The SP obtained from our techniques was -39%.

This SP differ from the values reported previously reported (one order of magnitude more than CV measurements, -12%).[65] The high selectivity measured here as compared to that found in the photoemission and cyclovoltammetry analysis, that use bigger working areas (5 to 8 mm^2), may indicate that methods electrons coming from defective areas of the surface reduce the measured overall spin polarization measured.[65]

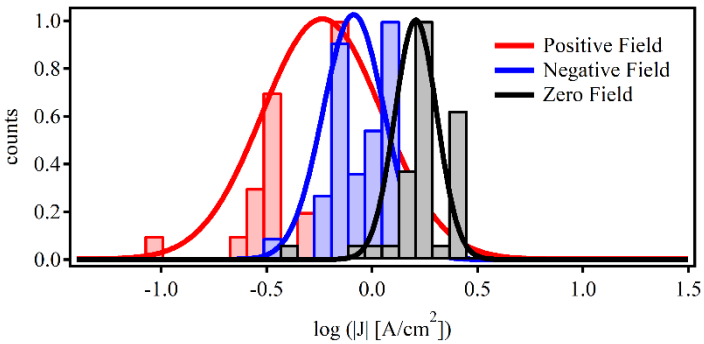

Figure 3-22 log |J| histograms measured at V = 0.15 V on a reference ALA8 SAM with the different magnetic field, the positive field is considered as 350 mT and negative field as -350 mT. Solid lines are gaussian fit from the data.

Once we have confirmed that CISS effect could be measured in our set-up. Next, we moved to Tb-LBTC (Figure 3-23) and as was expected from the right-hand helicity, Tb-LBTC can filter spin up electrons and therefore presents CISS effect. The spin polarization was up to -51% depending of the measured sample. These results were compared with CV measurements where the SP was -6%. As in the case of ALA8,[65,66] these CV values are one order of magnitude lower than those measured in the solid state using micrometric liquid contacts.

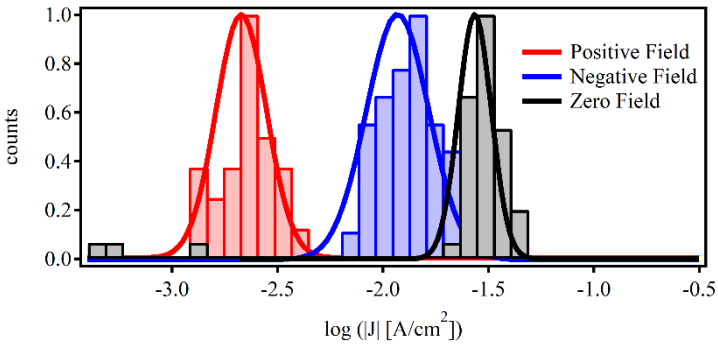

Figure 3-23 log |J| histograms measured at V = 0.15 V on a Tb-LBTC SAM with a different magnetic field, the positive field is considered as 350 mT and negative field as -350 mT. Solid lines are gaussian fit from the data.

4. Conclusions

With regards to equipment, I have optimized an old QCM to perform deposition experiment involving repeated cycling of different reagents and cleaning solutions. I have used this set-up to measure the progressive formation of LBTC and Tb-LBTC onto an Au surface and to estimate its coverage. Also, I have applied the method to grow HC. However, after having compared the results obtained with those of the LbL method we have come to the conclusion that LbL method is more convenient for HC due to QCM method presenting imperfections in the films produced.

Later, I have studied the electrical transport using EGaIn liquid contacts to avoid damage to the films. In the case of HC, we have shown that structure (pillaring ligand pyridine (py), pyrimidine (pym) or isoquinoline (isoq)) has a marked effect on transport properties. In the case of LBTC, I have shown for the first time that when these measurements are performed in the presence of a magnetic field CISS effect can be studied. I have thus, shown that LBTC as other helical

oligopeptides can act as spin-filter.[23,24,65–68] Moreover, the SP values measured are one order of magnitude above thus reported using other techniques. We attribute this, to the more local nature of this technique compared to electrochemical or photoemission experiments, for example.

5. Future Work

With respect to QCM, we are evaluating the possibility to change its way of operation from a continuous flow operation mode, to a step like operation, closer to that used in the LbL method. We will control pump direction and use a single pipe and to successively fill and empty the reaction vessel with the reagent and cleaning solution, to ensure a homogeneous distribution of reagents over all the surface area. We will also add a sonicator like Wöll et al[69] to further assure that the previous reagent has been removed from the vessel and will also change the tubing diameter to allow greater flows. This should result in the obtaining of better-quality films like the films obtained from LbL method.

6. Bibliography

1. Han, C.-W. *et al.* Advanced technologies for UHD curved OLED TV. *J. Soc. Inf. Disp.* **22**, 552–563 (2014).

2. Grätzel, M. The light and shade of perovskite solar cells. *Nat. Mater.* **13**, 838–842 (2014).

3. Prinz, G. A. Magnetoelectronics. *Science* **282**, 1660-1663 (1998).

4. Freeman, M. R. Advances in Magnetic Microscopy. *Science* **294**, 1484–1488 (2001).

5. Wolf, S. A. Spintronics: A Spin-Based Electronics Vision for the Future. *Science* **294**, 1488–1495 (2001).

6. Žutić, I., Fabian, J. & Das Sarma, S. Spintronics: Fundamentals and applications. *Rev. Mod. Phys.* **76**, 323–410 (2004).

7. Sanvito, S. The rise of spinterface science. *Nat. Phys.* **6**, 562-564 (2010).

8. Sun, D., Ehrenfreund, E. & Valy Vardeny, Z. The first decade of organic spintronics research. *Chem. Commun.* **50**, 1781-1793 (2014).

9. Forment-Aliaga, A. & Coronado, E. Hybrid Interfaces in Molecular Spintronics. *Chem. Rec.* **18**, 737–748 (2018).

10. Real, J. A., Gaspar, A. B. & Muñoz, M. C. Thermal, pressure and light switchable spin-crossover materials. *Dalt. Trans.* **0**, 2062–2079 (2005).

11. Gamez, P., Costa, J. S., Quesada, M. & Aromí, G. Iron Spin-Crossover compounds: from fundamental studies to practical applications. *Dalt. Trans.* **0**, 7845–7853 (2009).

12. Gütlich, P., Hauser, A. & Spiering, H. Thermal and Optical Switching of Iron(II) Complexes. *Angew. Chemie Int. Ed. English* **33**, 2024–2054 (1994).

13. Cambi, L. & Szegö, L. Über die magnetische Susceptibilität der komplexen Verbindungen. *Berichte der Dtsch. Chem. Gesellschaft (A B Ser).* **64**, 2591–2598 (1931).

14. Hogue, R. W., Singh, S. & Brooker, S. Spin crossover in discrete polynuclear iron(II) complexes. *Chem. Soc. Rev.* **47**, 7303–7338 (2018).

15. Gütlich, P. & Goodwin, H. A. Spin Crossover—An Overall Perspective. in *Spin Crossover in Transition Metal Compounds I* **1**, 1–47 (2004).

16. Bousseksou, A., Molnár, G., Salmon, L. & Nicolazzi, W. Molecular spin crossover phenomenon: recent achievements and prospects. *Chem. Soc. Rev.* **40**, 3313-3335 (2011).

17. Halcrow, M. A. *Spin-Crossover Materials*. *Spin-Crossover Materials: Properties and Applications* (John Wiley & Sons Ltd, 2013).

18. Gütlich, P., Gaspar, A. B. & Garcia, Y. Spin state switching in iron coordination compounds. *Beilstein J. Org. Chem.* **9**, 342-391 (2013).

19. Shepherd, H. J. *et al.* Molecular actuators driven by cooperative spin-state switching. *Nat. Commun.* **4**, 2607 (2013).

20. Brooker, S. Spin crossover with thermal hysteresis: practicalities and lessons learnt. *Chem. Soc. Rev.* **44**, 2880-2892 (2015).

21. Senthil Kumar, K. & Ruben, M. Emerging trends in spin crossover (SCO) based functional materials and devices. *Coord. Chem. Rev.* **346**, 176–205 (2017).

22. Kahn, O. *Molecular Magnetism*. *VCH Publishers,Inc.* (John Wiley & Sons, Ltd, 1994).

23. Naaman, R. & Waldeck, D. H. Chiral-induced spin selectivity effect. *J. Phys. Chem. Lett.* **3**, 2178–2187 (2012).

24. Gutierrez, R., Díaz, E., Naaman, R. & Cuniberti, G. Spin-selective transport through helical molecular systems. *Phys. Rev. B* **85**, 081404 (2012).

25. Guo, A.-M. & Sun, Q. Spin-Selective Transport of Electrons in DNA Double Helix. *Phys. Rev. Lett.* **108**, 218102 (2012).

26. Medina, E., López, F., Ratner, M. A. & Mujica, V. Chiral molecular films as electron polarizers and polarization modulators. *EPL (Europhysics Lett).* **99**, 17006 (2012).

27. Al-Bustami, H. *et al.* Single Nanoparticle Magnetic Spin Memristor. *Small* **14**, 1801249 (2018).

28. Otsubo, K., Haraguchi, T. & Kitagawa, H. Nanoscale crystalline architectures of Hofmann-type metal–organic frameworks. *Coord. Chem. Rev.* **346**, 123–138 (2017).

29. Peptides. *IUPAC Compend. Chem. Terminol.* **1307**, 4479 (2014).

30. Franz, K. J., Nitz, M. & Imperiali, B. Lanthanide-binding tags as versatile protein coexpression probes. *ChemBioChem* **4**, 265–271 (2003).

31. Silvaggi, N. R., Martin, L. J., Schwalbe, H., Imperiali, B. & Allen, K. N. Double-lanthanide-binding tags for macromolecular crystallographic structure determination. *J. Am. Chem. Soc.* **129**, 7114–7120 (2007).

32. Daughtry, K. D., Martin, L. J., Sarraju, A., Imperiali, B. & Allen, K. N. Tailoring Encodable Lanthanide-Binding Tags as MRI Contrast Agents. *ChemBioChem* **13**, 2567–2574 (2012).

33. Nitz, M., Franz, K. J., Maglathlin, R. L. & Imperiali, B. A powerful combinatorial screen to identify high-affinity terbium(III)-binding peptides. *ChemBioChem* **4**, 272-276 (2003).

34. Nitz, M. *et al.* Structural origin of the high affinity of a chemically evolved lanthanide-binding peptide. *Angew. Chemie - Int. Ed.* **43**, 3682–3685 (2004).

35. Nowinski, A. K., Sun, F., White, A. D., Keefe, A. J. & Jiang, S. Sequence, structure, and function of peptide self-assembled monolayers. *J. Am. Chem. Soc.* **134**, 6000–6005 (2012).

36. Rubio-Giménez, V. *et al.* Effect of nanostructuration on the spin crossover transition in crystalline ultrathin films. *Chem. Sci.* **10**, 4038–4047 (2019).

37. Sakaida, S. *et al.* Crystalline coordination framework endowed with dynamic gate-opening behaviour by being downsized to a thin film. *Nat. Chem.* **8**, 377–383 (2016).

38. Tang, Z., Liu, S., Wang, E. & Dong, S. Self-assembled monolayer of polyoxometalate on gold surfaces: quartz crystal microbalance, electrochemistry, and in-situ scanning tunneling microscopy study. *Langmuir* **16**, 4946–4952 (2000).

39. Zacher, D. *et al.* Liquid-Phase Epitaxy of Multicomponent Layer-Based Porous Coordination Polymer Thin Films of [M(L)(P)0.5] Type: Importance of Deposition Sequence on the Oriented Growth. *Chem. - A Eur. J.* **17**, 1448–1455 (2011).

40. Liu, B. *et al.* Enantiopure metal-organic framework thin films: Oriented SURMOF growth and enantioselective adsorption. *Angew. Chemie - Int. Ed.* **51**, 807–810 (2012).

41. Sauerbrey, G. Verwendung von Schwingquarzen zur Wägung dünner Schichten und zur Mikrowägung. *Zeitschrift für Phys.* **155**, 206–222 (1959).

42. Rubio-Giménez, V. *et al.* High-Quality Metal-Organic Framework Ultrathin Films for Electronically Active Interfaces. *J. Am. Chem. Soc.* **138**, 2576–2584 (2016).

43. Simeone, F. C. *et al.* Defining the value of injection current and effective electrical contact area for egain-based molecular tunneling junctions. *J. Am. Chem. Soc.* **135**, 18131-18144 (2013).

44. Neumann, T. *et al.* Superexchange Charge Transport in Loaded Metal Organic Frameworks. *ACS Nano* **10**, 7085–7093 (2016).

45. Goswami, S. *et al.* A porous, electrically conductive hexa-zirconium(iv) metal-organic framework. *Chem. Sci.* **9**, 4477-4482 (2018).

46. D'Alessandro, D. M. Exploiting redox activity in metal-organic frameworks: Concepts, trends and perspectives. *Chem. Commun.* **52**, 8957–8971 (2016).

47. Liu, H. *et al.* Length-Dependent Conductance of Molecular Wires and Contact Resistance in Metal–Molecule–Metal Junctions. *ChemPhysChem* **9**, 1416–1424 (2008).

48. Ho Choi, S., Kim, B. & Frisbie, C. D. Electrical Resistance of Long Conjugated Molecular Wires. *Science* **320**, 1482-1486 (2008).

49. Lu, Q. *et al.* From Tunneling to Hopping: A Comprehensive Investigation of Charge Transport Mechanism in Molecular Junctions Based on Oligo(p -phenylene ethynylene)s. *ACS Nano* **3**, 3861–3868 (2009).

50. Luo, L., Choi, S. H. & Frisbie, C. D. Probing Hopping Conduction in Conjugated Molecular Wires Connected to Metal Electrodes. *Chem. Mater.* **23**, 631–645 (2011).

51. Bu, D. *et al.* Understanding the charge transport properties of redox active metal–organic conjugated wires. *Chem. Sci.* **9**, 3438–3450 (2018).

52. Liu, J. *et al.* Electric transport properties of surface-anchored metal-organic frameworks and the effect of ferrocene loading. *ACS Appl. Mater. Interfaces* **7**, 9824–9830 (2015).

53. Kaliginedi, V. *et al.* Promising anchoring groups for single-molecule conductance measurements. *Phys. Chem. Chem. Phys.* **16**, 23529–23539 (2014).

54. Tuccitto, N. *et al.* Highly conductive ~40-nm-long molecular wires assembled by stepwise incorporation of metal centres. *Nat. Mater.* **8**, 41–46 (2009).

55. Luo, L. *et al.* Length and Temperature Dependent Conduction of Ruthenium-Containing Redox-Active Molecular Wires. *J. Phys. Chem. C* **115**, 19955–19961 (2011).

56. Sedghi, G. *et al.* Long-range electron tunnelling in oligo-porphyrin molecular wires. *Nat. Nanotechnol.* **6**, 517-523 (2011).

57. Sakamoto, R., Wu, K.-H., Matsuoka, R., Maeda, H. & Nishihara, H. π-Conjugated bis(terpyridine)metal complex molecular wires. *Chem. Soc. Rev.* **44**, 7698–7714 (2015).

58. Chiechi, R. C., Weiss, E. A., Dickey, M. D. & Whitesides, G. M. Eutectic gallium-indium (EGaIn): A moldable liquid metal for electrical characterization of self-assembled monolayers. *Angew. Chemie - Int. Ed.* **47**, 142–144 (2008).

59. Yoon, H. J. *et al.* The Rate of Charge Tunneling through Self-Assembled Monolayers Is Insensitive to Many Functional Group Substitutions. *Angew. Chemie Int. Ed.* **51**, 4658-4661 (2012).

60. Bernasek, S. L. Can We Understand the Molecule in Molecular Electronics? *Angew. Chemie Int. Ed.* **51**, 9737–9738 (2012).

61. Leary, E. *et al.* Incorporating single molecules into electrical circuits. the role of the chemical anchoring group. *Chem. Soc. Rev.* **44**, 920–942 (2015).

62. Bâldea, I. Transition Voltage Spectroscopy: An Appealing Tool of Investigation in Molecular Electronics. in *Molecular Electronics* (ed. Bâldea, I.) **6**, 397–437 (Pan Stanford, 2015).

63. Yi, X. *et al.* Probing Frontier Orbital Energies of {Co 9 (P 2 W 15) 3 } Polyoxometalate Clusters at Molecule–Metal and Molecule–Water Interfaces. *J. Am. Chem. Soc.* **139**, 14501-14510 (2017).

64. Smith, C. E., Xie, Z., Bâldea, I. & Frisbie, C. D. Work function and temperature dependence of electron tunneling through an N-type perylene diimide molecular junction with isocyanide surface linkers. *Nanoscale* **10**, 964–975 (2018).

65. Kettner, M. *et al.* Spin Filtering in Electron Transport Through Chiral Oligopeptides. *J. Phys. Chem. C* **119**, 14542-14547 (2015).

66. Kiran, V. *et al.* Helicenes - A New Class of Organic Spin Filter. *Adv. Mater.* **28**, 1957–1962 (2016).

67. Mondal, P. C. *et al.* Chiral Conductive Polymers as Spin Filters. *Adv. Mater.* **27**, 1924–1927 (2015).

68. Kiran, V., Cohen, S. R. & Naaman, R. Structure dependent spin selectivity in electron transport through oligopeptides. *J. Chem. Phys.* **146**, 092302 (2017).

69. Gu, Z.-G. *et al.* Transparent films of metal-organic frameworks for optical applications. *Microporous Mesoporous Mater.* **211**, 82–87 (2015).

Resumen en castellano

El propósito de esta tesis, titulada **"Ingeniería de nuevas herramientas para la automatización. Fabricación de películas delgadas moleculares y Estudio de sus propiedades eléctricas",** es el desarrollo de algunas plataformas faltantes en el Instituto de Ciencia Molecular (ICMol) para llevar acabo el estudio de propiedades eléctricas de materiales moleculares e integrarlos en dispositivos electrónicos. Los objetivos específicos son: i) la nanoestructuración de materiales moleculares novedosos como los polipéptidos, las redes metal orgánicas bidimensionales (2D MOFs, two dimentional metal-organic frameworks), polímeros de coordinación que presenten bi-estabilidad de espín en capas finas y ii) medir de manera fiable sus propiedades eléctricas e integrarlos en dispositivos funcionales (por ejemplo, sensores de gas o transistores de efecto de campo) compatibles con tecnologías actuales.

La tesis se centró específicamente en la descripción de las herramientas que se diseñaron y construyeron, y cómo se usaron. Adicionalmente, se prestó especial atención en mostrar sus limitaciones y cómo se pueden mejorar a corto plazo.

Este documento está dividido en tres capítulos: uno de introducción, sobre principios generales de propiedades electrónicas y técnicas de medición de conductividad, y los otros, de trabajo experimental, donde se detalla del desarrollo de las herramientas usadas para medir las propiedades eléctricas de los materiales.

El primer capítulo empieza introduciendo en las redes metal-orgánicas y porqué son candidatos prometedores para integrarlas

en dispositivos electrónicos. Después, presenta los principios generales para entender las propiedades eléctricas usadas en las técnicas para medir las propiedades eléctricas en muestras en polvo y en capas finas. Finalmente, un resumen general de las técnicas usadas para depositar redes metal-orgánicas (MOFs)[1] en capas finas.

Los MOFs son sólidos cristalinos construidos a partir de ligandos orgánicos y componentes inorgánicos unidos con enlaces de coordinación. Gracias al posicionamiento organizado de los grupos inorgánicos o uniones metálicas y los ligandos orgánicos en espacios tridimensionales se forman estructuras regulares con superficies muy altas de hasta 8000 m^2g^{-1} por el momento. Además, mediante ingeniería molecular se puede modificar el tamaño, la forma y la función química de sus cavidades, dando lugar a una extensa familia de sólidos cristalinos con diferentes estructuras y grupos funcionales.

MOFs ya son usados en aplicaciones como el almacenamiento y separación de gases como también para catálisis heterogénea. Además, han ganado importancia en aplicaciones como censado de gases, magnetismo, ferro-electricidad, óptica no lineal y entrega de medicamentos localmente. Tradicionalmente los MOFs exhiben una muy baja conductividad a consecuencia de la forma en que están construidos, donde los iones metálicos están contados por ligandos inactivos redox que se unen a través de átomos de oxígeno. Por lo tanto, la mayoría de los MOFs no tienen transportadores de carga de baja energía ni transportadores de carga libres y por eso tienen un comportamiento aislante con una conductividad de 10^{-10} Scm^{-1}. Sin embargo, en la última década han sido reportados significativos

[1] por sus siglas en inglés: metal-organic frameworks

ejemplos de MOFs conductores. Con la conductividad eléctrica agregando una nueva dimensión a su naturaleza, los MOFs han encontrado recientemente nuevas aplicaciones en dispositivos eléctricos. Por ejemplo, en sensores quimioresistivos, supercondensadores, componentes para baterías, celdas solares, termoeléctricos y hasta en FETs[2].

En gran medida las nuevas áreas dependen fundamentalmente de la evaluación comparativa de las propiedades eléctricas de los MOFs incluyendo la conductividad eléctrica, la movilidad, la densidad de carga, la separación de la banda electrónica y la energía de activación.

La conductividad eléctrica es el factor clave por el cual el transporte en MOFs es juzgado, y es definida por la densidad de carga y la movilidad de los electrones y huecos. Para alcanzar una alta conductividad es necesario tener una gran densidad y movilidad de carga.

De acuerdo con la teoría de bandas, los materiales están clasificados en aislantes, semiconductores o metálicos basados en la brecha de energía entre la banda de conducción y la banda de valencia. Las bandas por debajo del nivel de Fermi son llamadas bandas de valencia y las que se encuentran encima bandas de conducción. Los materiales con una brecha de energía superior a 4eV son considerados aislantes, mientras que con una brecha de entre 0 y 3eV son semiconductores y aquellos con una brecha igual a 0 son considerados metales. En los conductores metálicos, la banda de conducción y de valencia se solapan y sus transportadores de carga están libres dando así una alta conductividad eléctrica (>100 Scm^{-1}).

[2] (Field-Effect Transistor, en inglés)

En semiconductores y aislantes, el nivel de Fermi se encuentra en medio de la banda de conducción y la de valencia. La distancia entre el punto de menor energía en la banda de conducción o el punto mayor energía en la banda de valencia al nivel de Fermi es llamado energía de activación. A determinada temperatura los electrones son promovidos a la banda de conducción. Entonces la densidad de carga es dependiente de la temperatura y de la energía de activación.

Para los MOFs hay dos tipos de transporte, transporte por bandas o por salto. En el transporte por bandas, las moléculas tienen que estar muy bien organizadas para que todos sus niveles de energía se solapen formando las bandas de conducción y de valencia, en tal caso los electrones se podrán mover a través de ellas, de lo contrario los electrones saltan de las diferentes bandas de los átomos de una molécula que es lo que se llama transporte por salto. El transporte de bandas puede presentarse a través del espacio, la molécula huésped o el enlace con los ligandos.

Hasta ahora hemos visto los conceptos básicos de la conductividad eléctrica en MOFs. Ahora veremos, las técnicas usadas para medir muestras en polvo, o en películas finas.

La conductividad eléctrica depende principalmente de la corriente y el voltaje de circuito además del área de los contactos y de la distancia entre los mismos. Todas las muestras pueden ser medidas a 2 o 4 puntas. Por lo general para muestras con una resistencia menor a 1 Kilo ohm se usa medición a 4 puntas para eliminar la resistencia de los contactos, ya que esta puede alcanzar unas cuantas centenas de ohm lo cual causaría un error del 10% o más. Para muestras con una resistencia superior se usará una medición a 2 puntas.

Para medir muestras en polvo prensado es necesario tener algunos factores de corrección como el espesor de la muestra y la distancia entre los contactos, sin estos factores los valores de conductividad pueden cambiar hasta un orden de magnitud.

Para muestras en capas finas por lo general se usan dos configuraciones: horizontal y vertical. La aproximación más sencilla para medir capas finas es la horizontal ya que se pueden usar además de los contactos necesario para medir la muestra, contactos adicionales para medir la modulación del material con un voltaje de puerta como se hace en los FETs. Esta configuración solo es útil cuando las muestras tienen una resistencia menor a 1 giga ohm con una distancia entre contactos de 2.5μm. Para esta configuración son necesarios el área de los contactos y la distancia entre ellos. Para el caso de muestras con resistencia superiores o que presentan multicapas es necesario medirlas en disposición vertical. En este tipo de arreglo la distancia entre los contactos es reducida al espesor del material y para nuestro caso, como contacto superior, usamos metales líquidos. Dado que en esta técnica no es posible conocer el área del contacto inferior, se compara la densidad de corriente de diferentes materiales. La densidad de corriente se calcula dividiendo la corriente eléctrica en el área del contacto de metal líquido.

Para poder realizar medidas en películas finas es necesario la deposición de estos materiales en superficies planas. Estas técnicas están divididas en tres tipos: deposición de coloides/dispersión coloidal, síntesis directa o capa a capa.

La fabricación de capas finas a través de la deposición de coloides/dispersión coloidal consta de dos pasos. El primero es

preparar nanopartículas coloidales en disolución y después depositarlas en superficie. Para realizar esta tarea se usan las técnicas tradicionales de deposición como dip-coating, drop-casting o spin-coating. Estos métodos permiten capas de un espesor de unos 500 nm.

En el caso de la fabricación de capas finas a través de síntesis directa, el solvente, los reactivos y el sustrato permanecen juntos durante la reacción. Una vez termina la reacción se obtiene un polvo depositado en el sustrato. Estas técnicas permiten reducir el espesor de las muestras hasta unos 40 nm dependiendo de la reacción.

Por último, tenemos la fabricación capa a capa, dividida en dos: fabricación capa a capa asistida y Langmuir Blodgett, como método de fabricación capa a capa. La fabricación capa a capa consiste en la deposición secuencial de los reactivos con una limpieza con el solvente común entre ambos para evitar la competencia entre la nucleación de los componentes cercanos y la deposición de las capas. Basándose en este método, han surgido varias alternativas. Por ejemplo, el método de inmersión que consiste en sumergir el sustrato en cada uno de los componentes, ya sea de forma manual o de forma automática usando un robot; el método de flujo continuo que consiste en sellar el sustrato en una cámara en la cual se inyectan de forma secuencial los reactivos que también permite usar microbalanza de cuarzo o resonancia de plasmones superficiales; el método de spray el cual sigue la misma idea de los dos anteriores con la diferencia que esta vez los reactivos son depositados a través de un spray y por último, el método de spin-coating es básicamente la deposición de los diferentes reactivos mientras el sustrato va girando sobre su mismo eje a una velocidad determinada. Por otro lado, está el método de Langmuir Blodgett como

método de deposición capa a capa que consiste en la formación de las capas en una solución acuosa para después transferir la capa al sustrato, este método es repetido las veces necesarias para obtener el espesor de la película deseada. Las técnicas basadas en la deposición capa a capa son las que ofrecen mayor control en la deposición, además de poder depositar capas de entre 1 a 10 nm. Por esta razón durante los próximos capítulos se usarán Langmuir Blodgett para depositar Cu-CAT-1 y el método de inmersión para depositar los clatratos de Hoffman.

El segundo capítulo, se enfocó en el estudio de MOFs bidimensionales que han ganado gran interés por su gran variedad de propiedades, entre ella las respuestas quimioresistivas que presentan, especialmente el caso de las familias $M_2(HITP)_2$, $M_3(HTTP)_2$, $M_3(HHTP)_2$, entre ellos la única diferencia que tienen es el átomo que se conecta al metal, N, S y O respectivamente. Esto le confiere a cada uno y de acuerdo con el metal M que se le coordine, dándole diferentes habilidades de detección de gases. Para nuestro caso, nos hemos enfocado en la familia $M_3(HHTP)_2$ con los metales como Co, Ni, Cu, Zn y Cd. La síntesis de estos compuestos se llevó a cabo mediante una reacción solvotermal, calentando hasta una temperatura y tiempo determinados. Una vez obtenido el polvo de cada uno de los miembros de la familia se procedió a medir la conductividad de cada uno de los materiales. Para realizar esta tarea, se prensó el polvo obtenido para formar tabletas y se diseñó un equipo capaz de medir la conductividad eléctrica de las mismas. Este equipo esta basado en el sistema tradicional de 4 puntas alineadas con la diferencia que las puntas son retráctiles para adaptarse a la superficie y tener un dinamómetro para medir la presión ejercida sobre la muestra, además se compone de un soporte para sostener el dinamómetro, una cámara para medir la distancia entre puntas y el

espesor de la muestra, y un soporte para la muestra con desplazamiento micrométrico en los tres ejes de coordenadas. Las puntas van conectadas a los equipos para aplicar voltaje y medir corriente; estos equipos y la cámara están conectadas a un ordenador para registrar toda la información y tratar posteriormente los datos.

Tras realizar las medidas en cada una de las muestras se observó que la muestra más conductora de la familia fue aquella que se encontraba coordinada con Cu.

Para comprobar que los datos observados no fueron un resultado de un error del equipo se realizaron dos tipos de pruebas al equipo: Medir una muestra en dos posiciones diferentes, y medir la muestra, triturarla, hacer de nuevo la tableta y medirla de nuevo.

El resultado obtenido en estos experimentos ha mostrado que se pueden registrar cambios de hasta un 50% en la corriente al medir la muestra en dos posiciones diferentes y, en cuanto a medir la muestra antes y después de haberla triturado, los resultados arrojaron que se puede registrar un cambio de hasta un 80%. Sin embargo, los cambios registrados entre los diferentes miembros de la familia fueron mayores al 100% en cada uno de los casos denotando que entre el Cu y el Co hay un cambio del 500% siendo el Cu el mas conductor. Esto puede ser explicado por la diferencia estructural en cada uno de los compuestos además de la liberación del agua a la hora de triturar la muestra.

Una vez confirmado que el $Cu_3(HHTP)_2$, a partir de ahora renombrado como Cu-CAT-1, y con el objetivo de hacer un dispositivo, se decidió depositar este material en películas finas y medir sus propiedades eléctricas. La deposición se llevó a cabo mediante el método Langmuir

Blodgett como método de capa a capa sobre un sustrato previamente funcionalizado con una SAM[3] adecuada para la molécula que se quiso depositar.

Una vez perfeccionado el método de fabricación se decidió a depositar el Cu-CAT-1 en interdigitados de oro previamente depositados en una capa de óxido de silicio sobre un sustrato de silicio altamente dopado tipo n.

Lo primero que se hizo luego de depositar el Cu-CAT-1 fue medir la resistencia en función del número de transferencias realizadas, comparando el método capa a capa y el Langmuir Blodgett como método capa a capa. Los resultados arrojaron que el método Langmuir Blodgett presenta menos dispersión en los datos y por lo tanto mas fiable para realizar estudios de transporte en las mismas.

Después se realizó un estudio de la conductividad eléctrica frente a la temperatura en un dispositivo de 10 transferencias. Como resultado se observaron dos tipos de transporte, uno dominado por activación térmica, es decir un incremento en la conductividad eléctrica cuando la temperatura es incrementada y el otro, dominado por el mecanismo de salto.

Como complemento de este trabajo se realizó una comparación de la modulación del material al ser expuesto a un voltaje de puerta. Se empezó aplicando un voltaje de puerta ejercido a través del sustrato usando la capa de óxido de silicio en el sustrato como dieléctrico. Como resultado, se obtuvo una modulación ínfimamente baja, por lo tanto, se decidió probar usando un voltaje de puerta desde arriba, en el

[3] Self-assembled monolayer por sus siglas SAM en inglés

cual se usó como dieléctrico un polímero aislante. Usando este método los resultados cambiaron drásticamente observando un cambio de un orden de magnitud con respecto a la intensidad obtenida sin aplicar un voltaje de puerta. Este cambio se atribuye a un mal contacto entre el sustrato y el MOF.

Una vez caracterizadas eléctricamente las películas finas de Cu-CAT-1 se decidió estudiar el mecanismo que el comportamiento quimioresistivo de este tipo de sistemas para lo cual es necesario aplicar un voltaje, medir una corriente eléctrica y además exponerlas a diferentes atmosferas. Para este propósito fue necesario diseñar una cámara, que fuera capaz de realizar esta labor. Al principio se empleó una caja estanca y se le abrieron tres agujeros: uno para las conexiones eléctricas y los otros dos para la entrada y salida de los gases. Para alojar la muestra dentro de caja se diseñó un soporte capaz de sujetar y contactarla eléctricamente para poder registrar los cambios eléctricos mientras la muestra es expuesta a las diferentes atmosferas.

Para este primer experimento se inyectó secuencialmente aire, aire seco, nitrógeno, amonio y de nuevo aire. Durante este proceso, la muestra fue monitorizada eléctricamente para estudiar sus cambios eléctricos durante el proceso.

Los resultados mostraron que en comparación a otros artículos publicados del mismo tipo de MOFs, el nuestro tomaba más tiempo del necesario para estabilizarse eléctricamente. Sin embargo, se podían observar claramente dos tipos de grupos: uno con las atmosferas poco reactivas como el aire seco y el nitrógeno, y el otro con las atmosferas reactivas como el amonio y el aire. La diferencia entre el aire y el aire seco se atribuye a que el aire tiene presencia de moléculas de agua la

cual son altamente reactivas como el amonio. Por otro lado, se observó que la muestra tardaba en estabilizarse por la fluctuación de la temperatura y la presencia de fugas lo que también incrementaba el consumo de gases, por esta razón a partir de este momento, para los siguientes experimentos la temperatura se mantuvo estable con un error de ±0.5℃.

Al ver los problemas que se tenían, se decidió diseñar una nueva cámara con un volumen interior, que fuera capaz de alcanzar ultra alto vacío y controlar la temperatura, además de tener las características de la cámara anterior, poder contactar eléctricamente y ser capaz de albergar gases sin tener fugas. Para hacer esto posible, se usó una "T" diseñada específicamente para soportar ultra alto vacío. Para las conexiones eléctricas se empleó una tapa KF50 adaptada para conexiones eléctricas y otra para poder inyectar y extraer gases. Adicionalmente, se diseñó un nuevo soporte para albergar la muestra y poder calentarla, mientras se realizaba la medida. Para poder controlar la temperatura, se ensambló un controlador de temperatura capas de controlar dos temperaturas simultáneamente.

Para este nuevo experimento, se inyectaron diferentes gases intercalados por un ciclo de vacío para acelerar el proceso y asegurar la liberación de todos los gases de la muestra. Por cada nuevo gas al que se expuso la muestra, se midió una curva de la corriente dependiente del voltaje. Para este nuevo experimento se emplearon los gases mencionados en el experimento anterior además de Argón, Oxigeno y ultra alto vacío. En este nuevo experimento se notó una mayor respuesta teniendo en cuenta que antes para obtener una respuesta estable se tardaba 1 día y ahora unas 3 horas.

Comparando los resultados del experimento con los datos teóricos, se concluyó que los gases reactivos interactúan con los centros metálicos de la estructura, que a su vez amplía la distancia entre las diferentes capas estructurales y, como consecuencia, reduce la respuesta eléctrica del material.

El tercer capítulo se enfocó en la fabricación de películas finas moleculares para estudiar su transporte de carga vertical. Para este propósito se centró el estudio en dos familias: los clatratos de Hoffman y los polipéptidos capaces de atrapar lantánidos. Estas familias son interesantes, principalmente, porque tienen características únicas. En el caso de los clatratos de Hoffman, presentan bi-esbilidad de espín en sus centros metálicos. Y en los polipéptidos, gracias a su quiralidad, podrían presentar efecto CISS[4].

Los clatratos de Hoffman son estructuras laminares auto ensambladas tridimensionales, basadas en capas de metal-cianuro-metal unidas verticalmente por pilares de anillos aromáticos con bases nitrogenadas.

Los polipéptidos se derivan de múltiples aminoácidos formando una cadena carbonada.

Previamente ambas moléculas han sido depositadas en superficie, pero este proceso no ha sido posible monitorizarlo. Por esta razón se decidió usar la microbalanza de cuarzo (QCM[5]) como herramienta para estudiar la dinámica de deposición de ambas moléculas. Para este propósito fue necesario combinar la QCM a con una bomba y una válvula de múltiples canales. Con la combinación de estos elementos,

[4] The Chiral Induced Spin Selectivity por sus siglas en inglés (CISS)
[5] Quartz Crystal Microbalance por sus siglas en inglés (QCM)

fue posible inyectar secuencialmente los diferentes reactivos para crear las estructuras deseadas.

Para el caso de la fabricación de películas finas de clatratos de Hoffman con pilares de piridina se empezó inyectando los diferentes reactivos con un flujo de 100µL/min durante 1000 segundos por ciclo hasta terminar con un flujo de 600µL/min durante 180s por ciclo.

Los resultados del experimento mostraron que con flujos lentos no es posible limpiar completamente el reactivo anterior, lo cual creaba competencia entre la nucleación de los compuestos y la formación de la película sobre la superficie obteniendo películas de mala calidad. Al aumentar el flujo la calidad de las películas mejora considerablemente pero lamentablemente no tiene la calidad adecuada para ser comparadas con las producidas por el método de capa a capa asistida por robot, usado anteriormente. Por lo tanto, se decidió continuar usando el método automatizado de capa a capa, en lugar de usar el que emplea la QCM.

En el caso de la fabricación de SAMs compuestas por polipéptidos, se buscaba estudiar la formación de las monocapas. Para este propósito se realizaron dos estudios: la deposición del péptido y el mismo coordinado a un lantánido. Como resultado se observó una diferencia del 30% entre la deposición del LBTC[6] enlazado al lantánido y del LBTC en ausencia del lantánido. Basado en los cálculos teóricos, se podrían encontrar dos posibles respuestas de porqué se observó este cambio: la primera es que la estructura quiral del LBTC se pierde y como consecuencia se puede compactar mejor la SAM y la segunda, es

[6] Lanthanide Binding Tag with Cisteine por sus siglas en inglés (LBTC)

que la estructura del LBTC se conserva y forma una segunda monocapa apilada sobre la primera, sin embargo, esto no se presenta en el LBTC que tiene coordinado el lantánido, por eso mismo se cree que es la menos probable.

Una vez estudiada la deposición de ambas moléculas se continuó con el estudio de transporte de carga vertical en ambas moléculas.

Para este propósito se adaptó una configuración que ya se tenía montada la cual usaba Hg como metal líquido. El problema de este metal es su viscosidad la cual le permite infiltrarse en las estructuras cuando estas son porosas como es el caso de los clatratos de Hoffman. Por esta razón se decidió cambiar al eutéctico de galio indio (EGaIn), el cual, gracias a su fina capa de óxido de galio, conserva su forma y no se infiltra en las estructuras de los materiales porosos. La configuración que se usó tiene un soporte que mantiene suspendida la aguja la cual sostiene el electrodo de metal líquido, una cámara digital, un objetivo 5x y una base con precisión micrométrica para moverse en las tres dimensiones del especio.

En el caso de los clatratos de Hoffman se estudiaron dos factores: la dependencia de la densidad de corriente frente al espesor de las películas, y el cambio de esta dependencia al cambiar la naturaleza de los pilares que sostienen la estructura. Para este último objetivo se escogieron 3 pilares similares: de piridina, de pirimidina y de isoquinolina.

Al medir las muestras de isoquinlona se observó que los datos estaban dispersos entre 4 ordenes de magnitud, por consiguiente, se realizó un estudio de los resultados obtenidos de densidad de corriente en

diferentes zonas de la muestra. La muestra se separó en 3 zonas diferentes dado a la forma en la que las muestras son fabricadas. Éstas se fabricaron sosteniendo las muestras por un extremo y sumergiéndolas en los diferentes elementos de comprende las moléculas. Como resultado, la parte por la que la muestra es sujetada no se logra depositar casi material y en el extremo opuesto ocurre lo contrario, se acumula todo el material creando espesores no deseados, por lo tanto, se decidió a partir de ese momento, solo tener en cuenta las medidas realizadas en el centro de las muestras que se esperaba fuera más homogénea, la cual fue demostrado en los resultados de densidad de corriente en las tres zonas.

Una vez resuelto este problema, se decidió seguir midiendo las muestras de piridina y pirimidina. Una vez comparados los resultados de todas las familias se observó que a pesar de que todas están ligadas de igual manera a la SAM en el contacto de oro, presentan una clara diferencia a la hora de realizar la interfaz con el EGaIn, en el cual la pirimidina ofrece una interfaz mas fuerte y por consiguiente muestra una densidad de corriente inicial (J_0) más alto, seguido de la familia con pilares de isoquinolina que presentan un valor menor de $J_{0,}$ pero al tener una distancia interplanar más amplia, dificulta el mecanismo de salto entre centros metálicos. Por último, se tiene la familia de piridina la cual tiene una J_0 más baja, pero presenta el mismo comportamiento que la pirimidina, por la ausencia del nitrógeno en su anillo aromático.

En el caso de las Tb-LBTC SAMs se realizaron dos estudios: averiguar la función de trabajo y observar si el sistema posee polarización de espín. Para averiguar la función de trabajo, primero fue necesario estudiarla eléctricamente, midiendo uniones de Au/Tb-LBTC/EGaIn

por toda el área de la muestra. Usando la información obtenida a través del modelo de un solo nivel con transmisión Lorentziana y espectroscopia de voltaje de transición se averiguó que se necesitan 0.7 eV para superar el Tb-LBTC y además una función de trabajo de 4.62 eV para la SAM de Tb-LBTC.

Una vez estudiada eléctricamente la muestra, se decidió averiguar si la SAM de Tb-LBTC podría filtrar espines polarizados. Con este objetivo en mente, se modificó la configuración de transporte eléctrico vertical para que fuera capaz de aplicar un campo magnético fijo, para lograrlo se puso debajo de la muestra un imán de neodimio y así aplicar un campo magnético mientras la muestra era media eléctricamente.

Para comprobar si la nueva configuración funcionaba, se decidió probar la polarización de espín en ALA8, la cual ha sido medida por ciclo-voltametría y espectrometría de fotoemisión, además de haber sido medida por AFM conductor. Teniendo en cuenta ésto, se midió la SAM de ALA8 y se obtuvo una polarización de espín de un orden de magnitud comparado con los obtenidos a través de medidas de ciclo-voltametría tal cual dice la bibliografía. Luego, se comprobó que la nueva configuración propuesta funcionó.

Con este resultado, se pasó a medir la SAM de Tb-LBTC con la nueva configuración propuesta y con ciclo-voltametría. Los resultados mostraron que la polarización de espín de la SAM de Tb-LBTC fue, en promedio, de un -51%, lo cual fue un orden de magnitud mayor al resultado obtenido por ciclo-voltametria, del 6%. Con esto se comprobó que Tb-LBTC es capaz de filtrar espines y que el equipo diseñado es capaz de medir polarización de espín, lo cual fue una nueva

contribución a las técnicas de medición de transporte eléctrico usando contactos líquidos.